Part 2: Descriptions of the proposed Crawford Lake GSSP and supporting SABSs
The Anthropocene Epoch and Crawfordian Age: proposals by the Anthropocene Working Group

Submitted to the **ICS Subcommission on Quaternary Stratigraphy**
On October 31, 2023

Submission prepared by members of the Anthropocene Working Group:
Colin N. Waters (Chair): University of Leicester, UK
Simon Turner (Secretary): University College London, UK
An Zhisheng: Chinese Academy of Sciences, Xi'an, China
Anthony Barnosky: University of California, Berkeley CA, USA
Alejandro Cearreta: Universidad del País Vasco, Spain
Andrew Cundy: University of Southampton, UK
Ian Fairchild: University of Birmingham, UK
Barbara Fiałkiewicz-Kozieł: Mickiewicz University, Poznań, Poland
Agnieszka Gałuszka: Jan Kochanowski University, Kielce, Poland
Jacques Grinevald: IHEID Genève, Switzerland
Irka Hajdas: ETH Zurich, Switzerland
Han Yongming: Chinese Academy of Sciences, Xi'an, China
Peter Haff: Duke University, Durham NC, USA (deceased)
Martin J. Head: Brock University, St. Catharines, Canada
Juliana Assunção Ivar do Sul: Leibniz Institute for Baltic Sea Research, Germany
Catherine Jeandel: LEGOS Université de Toulouse, France
Reinhold Leinfelder: Freie Universität Berlin, Germany
Francine McCarthy: Brock University, St. Catharines, Canada
John McNeill: Georgetown University, Washington DC, USA
Eric Odada: University of Nairobi, Kenya
Naomi Oreskes: Harvard University, Cambridge, USA
Clément Poirier: Normandie Université, Caen, France
Daniel deB. Richter: Duke University, Durham NC, USA
Neil Rose: University College London, UK
Yoshiki Saito: Shimane University, Matsue, Japan
William Shotyk: University of Alberta, Canada
Colin Summerhayes: University of Cambridge, UK
Jaia Syvitski: University of Colorado, Boulder CO, USA
Davor Vidas: The Fridtjof Nansen Institute, Lysaker, Norway
Michael Wagreich: University of Vienna, Austria
Mark Williams: University of Leicester, UK
Scott Wing: Smithsonian Institution, Washington DC, USA
Jan Zalasiewicz: University of Leicester, UK
Jens Zinke: University of Leicester, UK

Corresponding author: Colin Waters cw398@leicester.ac.uk
Updates (11th March 2024) related to revised GSSP candidate core and review by Kim Cohen

Contents

1. ASSESSMENT OF CANDIDATE STRATOTYPES FOR THE ANTHROPOCENE 4

2. THE PROPOSED GLOBAL BOUNDARY STRATOTYPE SECTION AND POINT: CRAWFORD LAKE, CANADA 5

3. THE PROPOSED STANDARD AUXILIARY BOUNDARY STRATOTYPES (SABSs) 20

3.1 Beppu Bay, Japan 21

3.2 Sihailongwan Maar Lake, China 30

3.3 Śnieżka Peatland, Poland 37

4. SUMMARY 44

REFERENCES (*AWG publications written in full, including defining papers for 12 sites and thematic sets) 47

APPENDIX 1: REQUIREMENTS FOR A GSSP/SABS 52

APPENDIX 2 DETAILS OF SELECTED REFERENCE SECTIONS 54

2.1 East Gotland Basin, Baltic Sea 54

2.2 Ernesto Cave, Italy 59

2.3 Karlsplatz, Vienna, Austria 62

2.4 North Flinders Reef, Australia 64

2.5 Palmer ice core, Antarctic Peninsula 67

2.6 San Francisco Estuary, California, USA 69

2.7 Searsville Lake, California, USA 71

2.8 West Flower Garden Bank Reef, Gulf of Mexico, USA 74

REFERENCES USED IN THE APPENDICES (* key references) 77

ABSTRACT

This part of the Anthropocene Working Group (AWG) submission proposes that the base of the Anthropocene should be defined as series/epoch, terminating the Holocene Series/Epoch with a single Crawfordian stage/age using a Global boundary Stratotype Section and Point (GSSP) in an annually varved Crawford Lake core, Ontario, Canada, defined at 17.5 cm in core CRA23-BC-1F-B at the base of the dark lamina in a varve deposited in 1952 CE, at the level where the primary marker shows a rapid increase in $^{239+240}$Pu concentrations (coinciding with a globally recognisable, isochronous signal of the first above-ground thermonuclear tests). Secondary markers, determined in precisely correlated core closely adjacent to the proposed GSSP host, include a marked increase in ^{14}C values and in spheroidal carbonaceous particles (SCPs), increased heavy metal concentrations, a decline in δ^{15}N values, a marked change in phytoplankton assemblages and declines in elm (*Ulmus*) pollen and in non-arboreal pollen.

The submission also provides descriptions of three proposed Standard Auxiliary Boundary Stratotypes (SABSs), in cores extracted from marine anoxic sediments of Beppu Bay (Japan), in Sihailongwan Maar Lake (China) and in the Śnieżka Peatland (Poland) and eight reference sections located in cores extracted from marine anoxic sediments in the Baltic Sea, from coral bioherms off Australia and in the Gulf of Mexico, from an Antarctic ice core, from San Francisco Estuary and nearby lake (USA), in a speleothem from northern Italy and a section in urban anthropogenic deposits in Austria. This ubiquity of signals verifies that the Anthropocene can be widely delineated as a sharply distinctive chronostratigraphic unit in diverse terrestrial and marine depositional environments, and reflects a major Earth System change that will have geologically lasting consequences.

1. ASSESSMENT OF CANDIDATE STRATOTYPES FOR THE ANTHROPOCENE

Given the brief duration of research into the Anthropocene since 2000 and by stratigraphers since the inception of the Anthropocene Working Group (AWG) in 2009, there is no historical stratotype for this unit. Following the conclusion by the AWG that the Anthropocene has stratigraphic reality identifiable in geological successions in diverse environments, with the guiding criterion for the base of the Anthropocene being one of the multiple stratigraphic signals around the mid-20th century (AWG, 2019; see Part 1, Appendix 1), the research required to propose a Global boundary Stratotype Section and Point (GSSP) commenced, and this submission concludes that assessment.

Eight distinct environments (anoxic marine basin, estuary/coastal, coral bioherms, lakes, peatlands, ice sheet, speleothem and urban anthropogenic deposits) in 12 locations across five continents have been assessed since 2019, with multi-proxy appraisals of these as potential GSSP sites and associated reference sections (Figure 1; Table 1). The analytical programme was enabled by Berlin's Haus der Kulturen der Welt (Rosol *et al*., 2023) and the site analyses were guided by, but were independent of, the AWG, though many AWG members were involved in one or more studies (Waters *et al*., 2023).

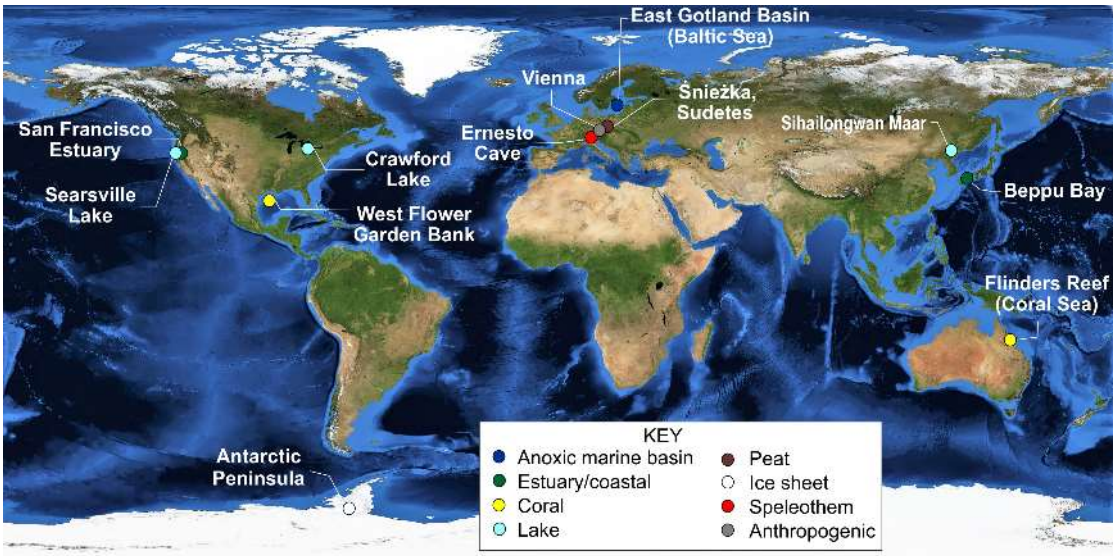

Figure 1. Location of the 12 candidate and other reference localities indicating the depositional environment. Satellite image: NASA Visible Earth. Source: reproduced from Waters et al. (2023).

A full description of the data and assessments for suitability for each site has been published in a thematic volume (vol. 10, part 1) of *The Anthropocene Review*, as referenced in Table 1. The voting procedure and results used to identify the candidate GSSP site, SABSs and reference sections are detailed in Appendix 1 of Part 1. The criteria followed to decide on site suitability are provided by Waters *et al*. (2023) and summarised in Table 1 (Appendix 1 of Part 2).

Table 1. The locality names and environments of the 12 candidate and other reference sites, listing the core/site altitude at time of collection, the full core length and length of that part that is established to be Anthropocene in age, and the relevant reference. Reproduced from Waters et al. (2023).

Location	Coordinate	Depositional environment	Altitude (m asl)	Core length (m)	Age of core top (year CE)	Age of core base (year CE)	Anthropocene thickness (m)	Relevant publication
East Gotland Basin, Baltic Sea	57.2830°N, 020.1204°E	Anoxic marine basin	-241	0.45	2018	~1840	0.278	Kaiser *et al*. (2023)
San Francisco Estuary, USA	37.5495°N, 122.1831°W	Estuary	-10.5	2.3	2019	~1952	~2.3	Himson *et al.* (2023)
Searsville Lake, USA	37.4068°N, 122.2378°W	Lake	104	9.445	2018	1900	3.54	Stegner *et al*. (2023)
Crawford Lake, Canada	43.4686°N, 79.9487°W	Lake	282	0.89	2023	~1000	0.175	McCarthy *et al.* (2024)
Sihailongwan Lake, China	42.2868°N, 126.6012°E	Lake	778	0.53	2021	~1200	0.089	Han *et al*. (2023)
Flinders Reef, Australia	17.7179°S, 148.4510°E	Coral reef	-10	3.33	2017	1708	0.4316	Zinke *et al.* (2023)
West Flower Garden Bank Reef, USA	27.8762°N, 93.8147°W	Coral reef	-21.3	1.74	2005	1755	0.3138	DeLong *et al.* (2023)
Palmer core, Antarctica	73.8521°S, 65.4526°W	Ice sheet	1897	133..45	2012	1621	34.91	Thomas *et al.* (2023)
Ernesto Cave, Italy	1.6575°E, 45.9772°N	Speleothem	1167	0.45	2000	~1 ka – 8.5 ka	0.005	Borsato *et al.* (2023)
Śnieżka peatland, Poland	50.7391°N, 15.7077°E	Peat	1440	0.5	2020	1931	0.395	Fiałkiewicz-Kozieł *et al.* (2023)
Beppu Bay, Japan	33.2778°N, 131.5373°E	Coastal marine basin	-71	0.94	2021	1917	0.648	Kuwae *et al*. (2023)
Karlsplatz, Vienna, Austria	48.1991°N, 16.3726°E	Urban anthropo-genic deposits	170	0.6	2019 – 2021	~1700	~0.3	Wagreich *et al.* (2023)

2. THE PROPOSED GLOBAL BOUNDARY STRATOTYPE SECTION AND POINT: CRAWFORD LAKE, CANADA

Project Leader and submission by Francine M.G. McCarthy. Details updated from McCarthy *et al*. (2023) and incorporated into McCarthy *et al*. (2024).

A distinct change in lithology in the varved succession of Crawford Lake dates to 1951 CE, the base of two centimetre-thick dark bands that are easily correlated between cores across the deep basin of Crawford Lake. The base of this lithological change occurs ~1 mm below the primary chronostratigraphic marker of the onset of the steady rise in $^{239+240}$Pu activities, taken to provide the principal guide for the location of the base of the Anthropocene. The contact between the thin (0.33 mm) pale calcite lamina and

overlying dark organic lamina, both assigned a varve age 1952 CE at 17.5 cm in the 89 cm-long freeze core CRA23-BC-1F-B is proposed as the GSSP for the Anthropocene series/ epoch and Crawfordian age/stage. This lithological boundary approximates (and is taken to represent) the moment when the first thermonuclear weapon (Ivy Mike) was detonated: 7:15 am (local time) on November 1st, 1952 in the Marshall Islands (19:15 on 31st October, GMT and 14:15 on 31st October, EST the local time at Crawford Lake).

Because the cores are archived in Ottawa, miscommunication about the core proposed as GSSP led to identifying core CRA23-BC-1F-A as the preferred choice since it was intact. It was only discovered on 20th October 2023, when the archive section was sought to determine the precise point of the GSSP, that this was the only 2023 freeze core subsampled for analysis for which an intact archive section was not preserved. An archive section was preserved from the nearly identical core CRA23-BC-1F-B, co-sampled with CRA23-BC-1F-A for annual plutonium analysis, so this is the proposed GSSP archive section.

1. Location and geological setting

Core CRA23-BC-1F-B (freeze core) was collected from 18.3 m water depth in the meromictic Crawford Lake together with 7 other freeze cores in April 2023, joining eight cores studied to track geological change in the mid-20th century (McCarthy *et al*., 2023). The lake occupies a deep sinkhole dissolved in dolomitic limestones of the Silurian Lockport Group in a rural ('Greenbelt') portion of the township of Milton, Ontario Canada, at 43.468658°N, 79.948726°W (Figure CL1).

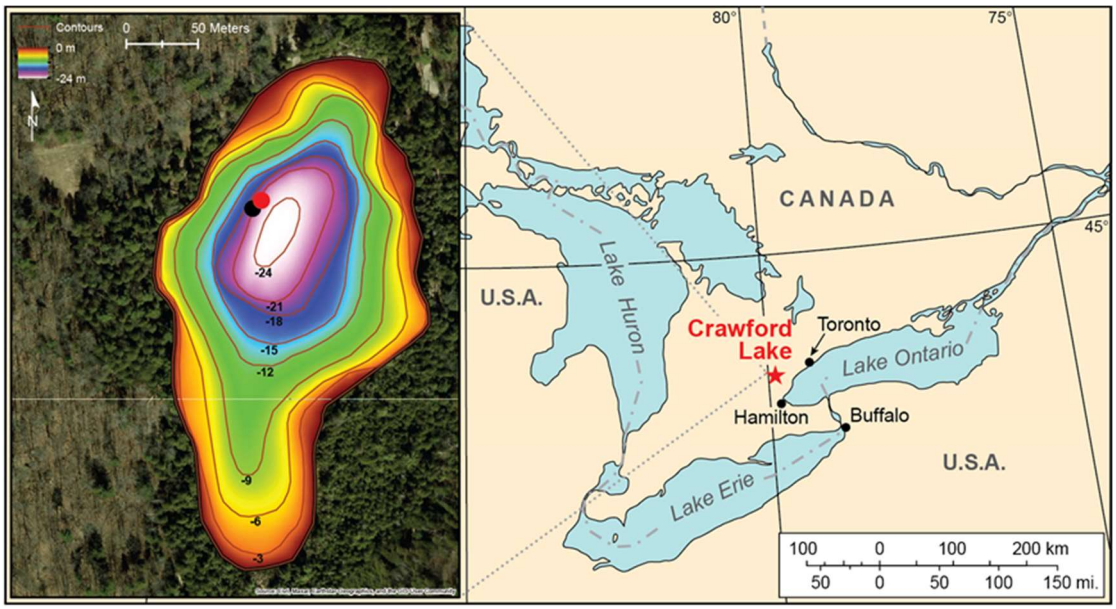

Figure CL1. The meromictic Crawford Lake is in a rural area of Canada in the Lake Ontario catchment, and the proposed GSSP core CRA23-BC-1F-B is from 18.3 m water depth (black dot), as are the other 12 cores analysed to assess the potential of its varved succession to define the proposed Anthropocene series/epoch and three cores that remain untouched. The location of core CRA23-2FT-A1, used to determine the ^{137}Cs chronology, is shown by the red dot. From McCarthy et al. (2024).

Its location high on the Niagara Escarpment (282 m asl) makes this deep basin ideal for preserving atmospheric deposition. Endogenic varves accumulate undisturbed below the chemocline (at 15.5 m water depth), and no benthic macrofauna disturb the lakebed although highly transmissive aquifers transfer highly oxygenated groundwater into the monimolimnion. Fossil pigment data record development of this distinctive depositional environment, in which authigenic calcite crystals started accumulating seasonally in the 13th century, coinciding with Indigenous agricultural settlement on thick, glacially derived soils in the far northwestern part of its catchment.

2. Lithology and indication in the field

Each varve comprises light- and dark-coloured laminae composed almost entirely of endogenic calcite and authigenic organic matter, respectively, with little siliciclastic influx. Varves provide annual precision for sampling, beginning in the early 19th century and spanning a 218-year interval in the middle of the last millennium, when eutrophication attributed to agricultural settlement altered the pH sufficiently each summer to allow abundant calcite to crystallise. Annual precision breaks down in the Little Ice Age interval (early 16th through 18th centuries) when temperature and pH conditions were generally unsuitable for calcite precipitation; Ca^{+2} and CO_3^{-2} dissolved from the Silurian limestones precipitate in the hard waters of the epilimnion when water temperature exceeds ~15°C and primary production/carbon fixation raises pH above 7.76. The bulk of the dark organic matter in the dark-coloured laminae accumulates on the lakebed when surface water temperatures plummet (inducing winter kill) and the mixolimnion becomes isothermal, i.e., between mid-October and early December. Although there is some accumulation during the rest of the calendar year, the bulk of each varve accumulates between June and December. There is very little accumulation in this small, isolated lake between January and June based on sediment trap studies (Llew-Williams *et al*., 2024).

Because water chemistry exerts a strong control on the precipitation of calcite and fixation of organic matter, the lithology reflects documented changes in climate and land use at local to global scales. Acid rain resulting from unchecked industrial emissions from the 1950s to early 1970s reduced the amount of calcite precipitated, producing two, centimetre-thick, dark bands in the varved succession in which there are very thin summer calcite laminae. These two dark bands are separated by a distinct triplet of calcite laminae deposited during the summers of 1957, 1958 and 1959 CE (Figure CL2). Sharp changes in bomb radionuclides and several proxies of the Great Acceleration are measured within the lower of these dark bands, i.e., through the early 1950s (Figures CL3–9). The GSSP for the Anthropocene series/epoch and Crawfordian stage/age is proposed at the contact between the thin (0.33 mm) pale calcite lamina and overlying dark organic lamina, both assigned a varve age 1952 CE at 17.5 cm in the freeze core CRA23-BC-1F-B.

(a)


CRA23-BC-1F-B
Depth (cm)
0
10
20
30
40
50
60
70
80
13
12
11
10
09
08
07
06
05
04
03
02
01
2000
99
98
97
96
95
94
93
92
91
90
89
88
87
86
85
84
83
82
81
80
79
78
77
76
75
74
73
72
71
70
69
68
67
66
65
64
63
62
61
60
59
58
57
56
55
54
53
52
51
1950
49
48
47
46
45
44
43
42
41
40
39
38
37
36

(b)

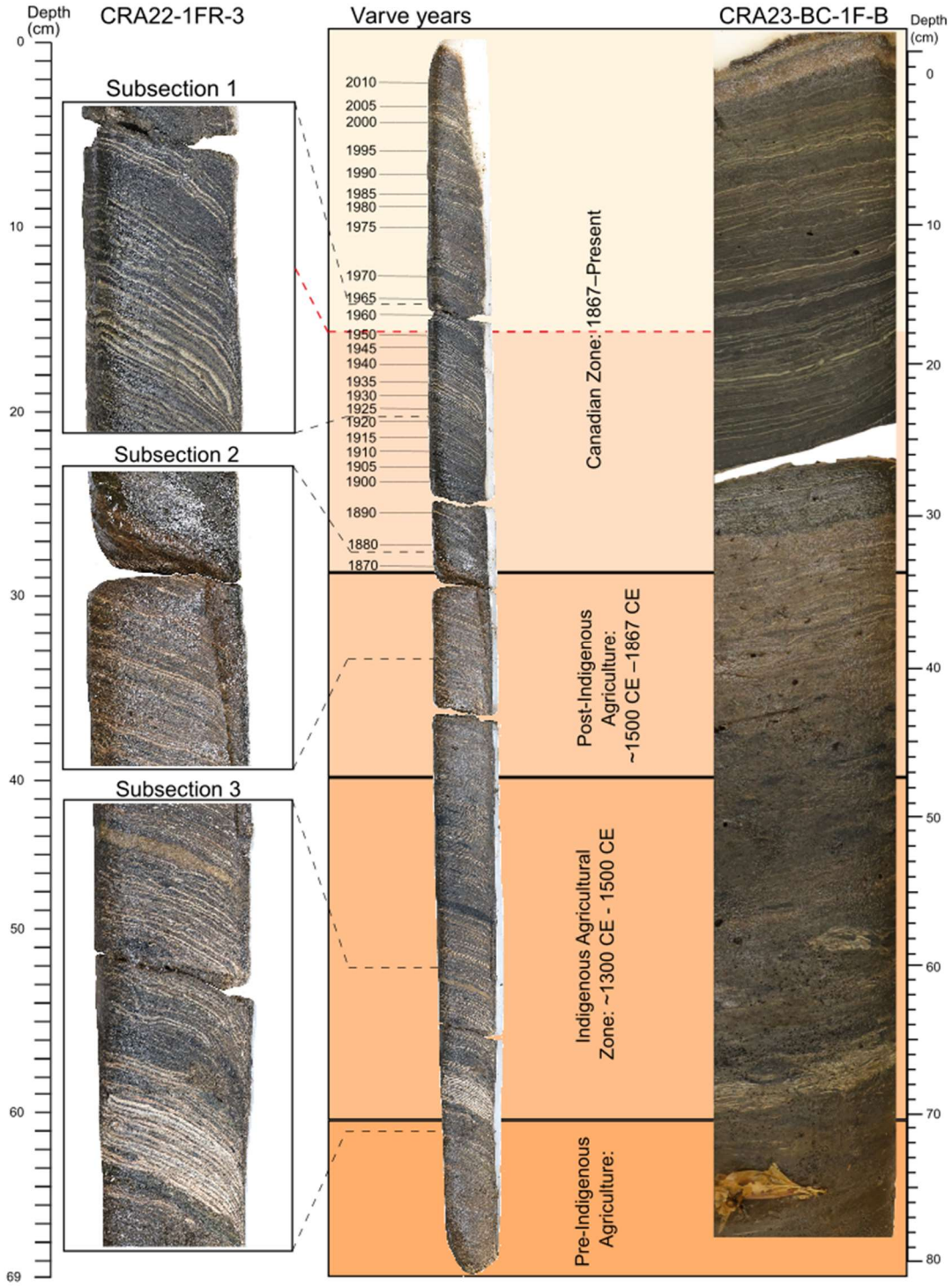
Depth (cm)
CRA22-1FR-3
Varve years
CRA23-BC-1F-B
Depth (cm)
Subsection 1
Subsection 2
Subsection 3
2010
2005
2000
1995
1990
1985
1980
1975
1970
1965
1960
1950
1945
1940
1935
1930
1925
1920
1915
1910
1905
1900
1890
1880
1870
Canadian Zone: 1867–Present
Post-Indigenous Agriculture: ~1500 CE –1867 CE
Indigenous Agricultural Zone: ~1300 CE - 1500 CE
Pre-Indigenous Agriculture:
0
10
20
30
40
50
60
69
70
80

(c)

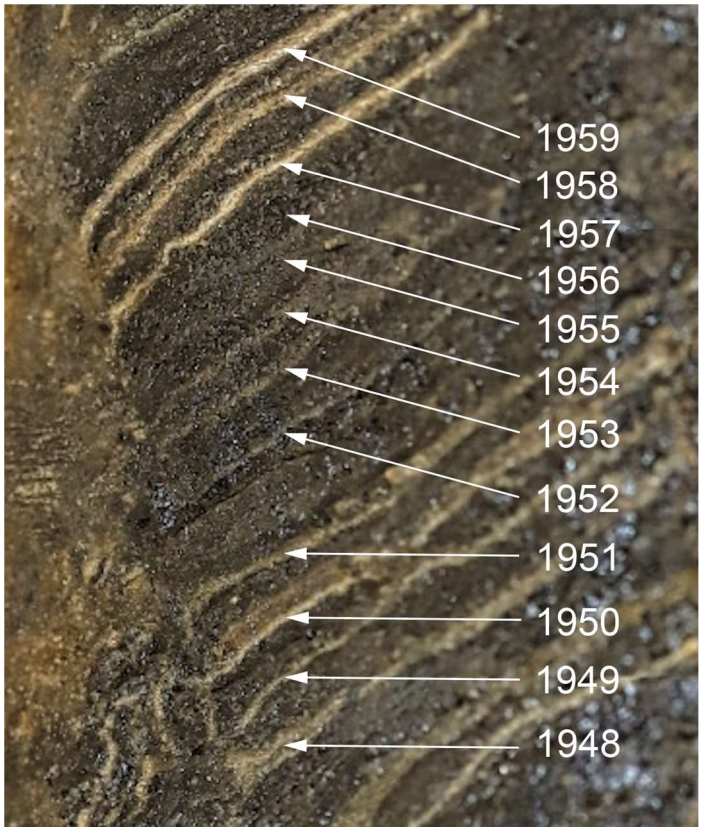

Figure CL2 (a) The proposed GSSP is at 17.5 cm in 89 cm-long freeze core CRA23-BC-1F-B at the contact between the thin (0.33 mm) pale calcite lamina and overlying dark organic lamina, together assigned a varve age 1952 CE, with the contact specifically marking *the Fall of 1952 CE. The thick calcite lamina at 20 cm, that formed the starting point for sampling above and below, was deposited in 1936 CE. N.B. that the depth scale relates to the right side of the core.* From *McCarthy et al. (2024). b) Endogenic varves began accumulating during the warm, arid Medieval Climate Optimum when an agricultural settlement was established in the NW part of the small catchment (69.5 cm in the CRA22-1FR-3 core, late 13th century) and resumed with colonial activity in the 19th century, culminating in intense logging and lumber milling in the catchment until 1900 CE. N.B. The varves are inclined in the wide freeze core, and all depths are given for the left-hand side of the core as viewed in the images. c) High-resolution photographic images of the edge of freeze core CRA23-BC-1F-B that includes the proposed 1952 GSSP horizon at 17.5 cm (1952 CE). The age model assumes that the thickest white calcite lamina formed during the exceptionally warm and dry summer of 1936 CE. Allowing the core surface to slightly dry caused the water-rich dark organic laminations to recede slightly, while the more resilient calcite-rich laminations remained in higher relief, making them easier to distinguish in the face-view image, although it produces a lighter-coloured image.*

3. Accessibility

Vertical sections of three freeze cores collected in 2022 and 2023 (including the core hosting the proposed GSSP) are archived in the National Biodiversity Cryobank of Canada at the Canadian Museum of Nature (CMN), Ottawa; two others are archived in the cold storage facility at the Royal Ontario Museum, Toronto; and the remainder are in the laboratory of R.T. Patterson at Carleton University, Ottawa, Canada. Scientific

collaborations using all these cores are welcome and displays and educational programmes at the museums and the Interpretive Centre at the Crawford Lake Conservation Area will inform the public about the lake and its sediment record. The lake is readily accessible off a major rural road within 50 km of international airports in Toronto and Hamilton, Canada, and just over 100 km from Buffalo, USA. Future cores can be collected with permission from Conservation Halton.

4. Conservation

The cores are conserved as described above, well protected but accessible. Crawford Lake is within a conservation area managed and protected by Conservation Halton since 1969, and since 2019, decisions on scientific access have been made in consultation with the Indigenous council. The Crawford Lake Conservation Area is within a Greenbelt Area of Ontario, Canada, and forms part of the UNESCO Niagara Escarpment Biosphere Reserve.

5. Stratigraphic completeness of the section

The sediments in the central part of the small, deep lake basin are not prone to erosion or disturbance. A single small, slow-flowing, spring-fed stream enters the lake at its north end, and outlet is through a shallow sill separating the lake from a wetland at the south end, eventually flowing into Lake Ontario. There is little terrigenous influx, since soil cover is thin and discontinuous over much of the small (~91 ha) catchment, and the effects of streamflow and overland flow are limited to the mixolimnion (upper 15.5 m) of the water column of this nearly 24 m-deep lake. The thick cedar-dominated forest and low-lying topography limit wind stress, and the very high ratio of depth to surface area inhibits mixing of the water column. Meromixis is re-enforced by a sharp increase in dissolved ion concentration ('salinity') and density around 15.5 m – the chemocline. There is no indication of bioturbation or physical disturbance of sediment in the deep basin, few allochthonous/siliciclastic layers and no indication of missing varves.

6. Age constraints

Ultra-high-resolution imagery was used to document the distinct varve pattern that facilitates precise correlation of individual varves between cores, providing annual resolution without error bars, although most of the sediment accumulates on the lakebed between July and December of any given calendar year. Historic records of climate and land use allow cross-validation of the age model based on varve counts, given the imperfect recovery of unconsolidated lakebed sediment at the top of the cores. Analysis of ^{137}Cs from individual varves carried out in summer 2023 on core CRA23-2FT-A1 (Figure CL3), located near to core CRA23-BC-1F-B. This shows the caesium bomb-spike beginning in 1955 CE, a decline in 1960–1961 CE, consistent with the moratorium in testing from November 1958 to September 1961, followed by a rapid increase. The peak ^{137}Cs in 1963 reveals that the varve age, based on the model of Lafond *et al*. (2023), was too old by 1 year, and subsequent climate modelling and varve counting in core CRA23-BC-1F-B supports readjustment of the age of the marker varve (the thickest light-coloured lamina of the calcite-rich 'Dust Bowl' interval of the 1930s) to 1936 CE from 1935 CE (McCarthy *et al.,* 2024). Because this marker was consistently used to assign ages and subsample up-core and downcore since the fall of 2019, age assignments in McCarthy *et al*. (2023) can confidently be shifted one year later.

7. Proxies for the base of the proposed Crawfordian stage

Primary marker:

The base of the initial rapid rise of plutonium bomb-spike, expressed as rapid increase in $^{239+240}$Pu activities/concentration to 0.0036 Bq/g, was measured in the varve deposited in 1952 CE, with samples collected from the base of each calcite layer to the top of the overlying organic layer, representing the bulk of sediment accumulation from June through fall turnover in November of each calendar year (Llew-Williams *et al*. 2024). This is at 17.5 cm depth in the archived section of the proposed GSSP core, CRA23-BC-1F-B. The increase of 0.0031 Bq/g from 0.0005 Bq/g in 1951 CE represents a 620% increase in one year. A similar increase, of 0.29 Bq/g (all with low errors), was measured between 1953 and 1954 CE. $^{239+240}$Pu activities reach a peak in 1963 CE (0.0299 ± 0.0017 Bq/g at 14.0 cm in core CRA23-BC-1F-B), rising sharply between 1961 (0.0175 ± 0.0008 Bq/g) and 1962 CE (0.0278 ± 0.0013 Bq/g). This is consistent with the rapid increase in global yields following the moratorium that lasted from November 1958 to September 1961 (UNSCEAR, 2000). A steady decline is measured beginning in 1964 CE, following ratification of the Limited Test Ban Treaty (Figure CL4a).

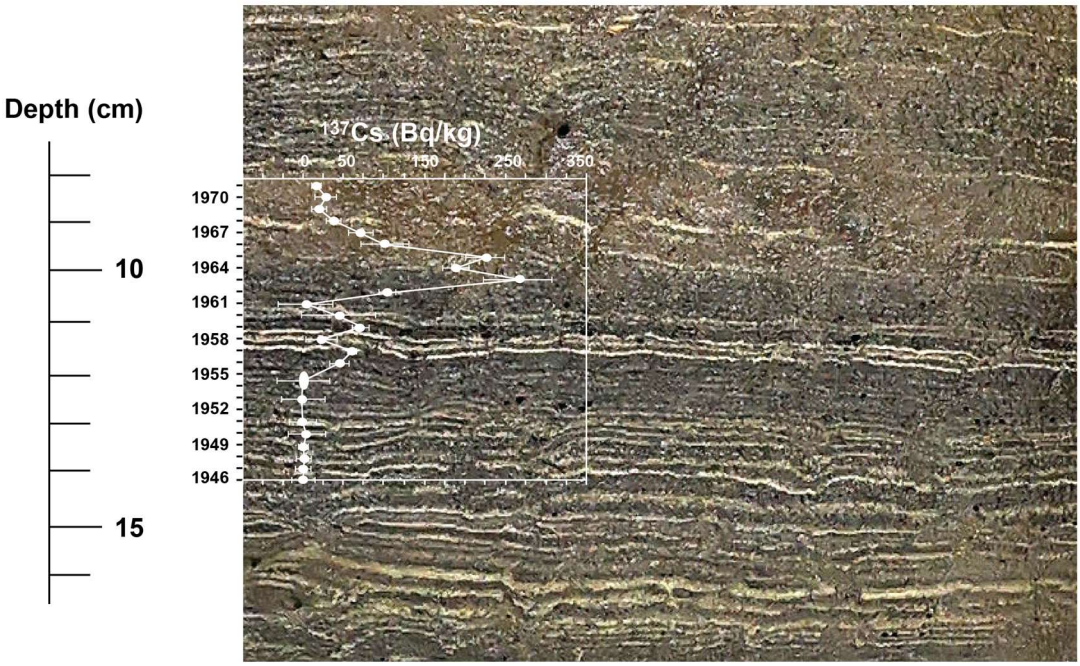

Figure CL3. ^{137}Cs activity measured from individual varves in core CRA23-2FT-A reflects global yields, with an increase beginning in 1955 CE, a decline in 1960–1961 CE (consistent with the moratorium in testing from November 1958 to September 1961) followed by a rapid increase. The higher activity measured in the varve sample '1962' than for '1964' suggests that the peak is in the missing sample, revealing a 1-year offset in the varve age model of Lafond et al. (2023). All analyses (spanning less than 5 cm in the core, illustrated here) are of individual varves except 1953–1954 CE, which were combined for analysis, and thus illustrated by an ellipse rather than a circle. From McCarthy et al. (2024).

This same Pu pattern was seen in other freeze cores from Crawford Lake, albeit at lower resolution, with samples that combined multiple varves (Figure CL4b, c). The longer series identifies the post-Test Ban Treaty decline to Nuclear Age background activities by the early 1980s as well as slightly elevated activity in the sample spanning 1947–1948 CE, comparable to that measured in the 1950 CE varve (0.0012 and 0.0011 Bq/g, respectively). Low activities ranging between 0.0139 and 0.0143 Bq/g in three samples from freeze cores collected in 2019 and 2022 span the late 1958–1961 moratorium and analysis of individual varves from 1955–1959 CE will be completed in January 2024. The remainder of the twelve varve samples being prepared at GAU Laboratories for AMS analysis at VERALabs span the mid–late 1940s, and the decline to background levels through the late 1960s.

The plutonium profiles are thus consistent with annual global detonation yields from above-ground nuclear weapons testing of thermonuclear devices since 1952 CE (UNSCEAR, 2000), and they capture, too, fallout from earlier atomic bombs. $^{240}Pu/^{239}Pu$ atomic ratios measured in most samples were in the range of global fallout (mean 0.180 ± 0.014), although ratios in the early-1950s were lower (Figures CL4a, c). The lowest ratios were measured in the 1952 CE varve and increase gradually beginning in 1953 CE, reaching the global mean by 1963 CE. Very low $^{240}Pu/^{239}Pu$ ratios appear to characterise this interval globally and could act as an additional marker for the GSSP (McCarthy *et al.,* 2024). Additional analysis of plutonium ratios, perhaps including additional isotopes, from individual varves should provide important insights into fingerprinting sources of fallout and quantification of lags between detonations and Pu accumulation.

The onset of the continuous (although not constant) rise in plutonium activity in the varve deposited primarily through the latter half of 1952 CE and also into early 1953, and in which $^{240}Pu/^{239}Pu$ atomic ratios were lowest (i.e., the largest relative increase in ^{239}Pu), is proposed to serve as the primary guide for the location of the GSSP. Beyond Crawford Lake, for practical purposes it is to be taken midpoint between the two adjacent annual samples that show the biggest proportional increase within the run of samples that all have detectable Pu. At Crawford Lake this definition coincides in core CRA23-BC-1F-B with the base of the organic lamina in the varve level equivalent to the Fall (October-December) 1952 CE, closely coincident with the first thermonuclear detonation on 1st November 1952 CE.

Figure CL4 [over page]. Plutonium isotopes across the proposed base of the Anthropocene (green line, base of the calcite laminae in the varve deposited in 1952 CE) in varved sediments from Crawford Lake. (a) Blank-corrected concentrations of atoms of ^{239}Pu per dry weight measured using accelerator mass spectrometry (AMS) in twelve individual varves from freeze cores collected in 2023, activities of ^{239}Pu and ^{240}Pu calculated from the atomic concentrations, and ratios of $^{240}/^{239}Pu$; (b) and (c) plotted with data from freeze cores collected in 2019 and 2022, all subsampled with reference to the same marker varve. Note, the profile image of the archived section of core CRA23-BC-1F-B illustrates the slight warping resulting from sinking slowly into the lake bed over the 30-minute interval that the laminated sediments freeze onto the super-cooled metal face of the sampler. The data at annual resolution are consistent with global yields, increasing steadily to 1954 CE from background values in 1951 CE, and rising quickly from 1961 to the peak in 1963 CE. The low activities measured in 1961 CE confirm the shoulder in the profile that identifies the 1958–1961 moratorium (grey shading). From McCarthy et al. (2024).

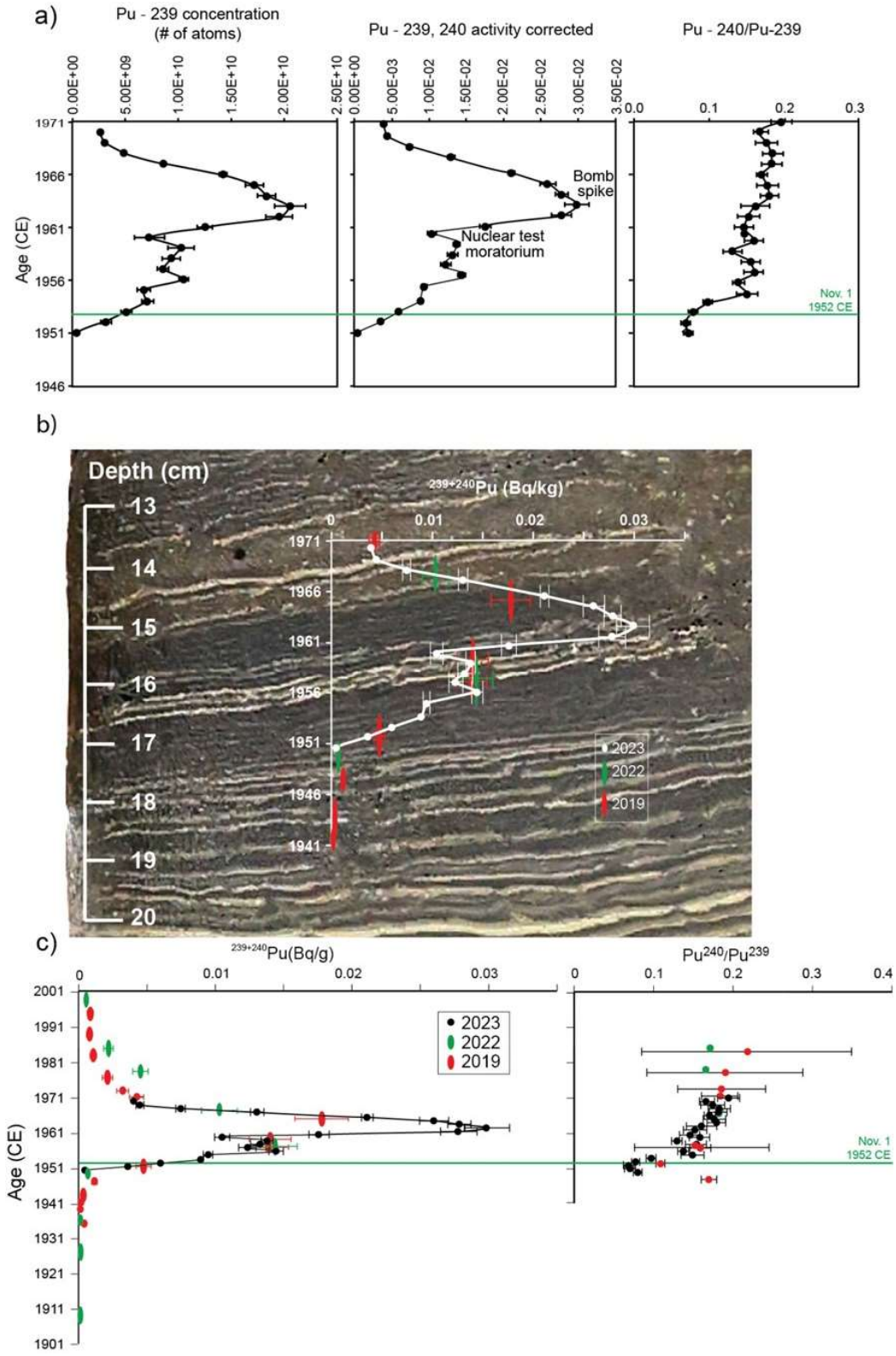

Additional proxies from other cores from the same locality:

a) ^{14}C values (measured as $F^{14}C$ in two cores, Figure CL5): marked increase beginning in the mid-1950s is consistent with the 'bomb pulse', despite the strong old carbon effect in this 430 Ma dolomitic limestone basin.

b) A marked increase in spheroidal carbonaceous particles (SCPs): sharply higher concentrations are recorded in two freeze cores (CRA19-2FT-B2 and CRA22-

1FR-A) from 1953 CE, following a gradual increase through the early 20th century, with the start of the continuous record of SCPs from the mid-1930s (Figure CL6). Smaller particle sizes (<10 µm) become more common from 1949 CE. Analysis of palynological preparations of varved sediments from freeze core CL-2011 confirm the peak in SCP concentration in the mid-1950s–1980s, with the decline attributed to enforced air quality standards in North America beginning in the 1970s. As with the nitrogen isotope and other organic proxy data (see below), there is some correlation with the relative abundance of calcite vs. organic matter in varves, and there is some variability between cores, but the overall pattern of atmospheric deposition of fly ash concentrations reflects the Great Acceleration. This signature is accentuated by the presence of steel mills 35 km SSE of Crawford Lake, which are a regional contributor of these products of high temperature fossil fuel combustion, and where records show steel production increased dramatically from the late 1940s through 1970s.

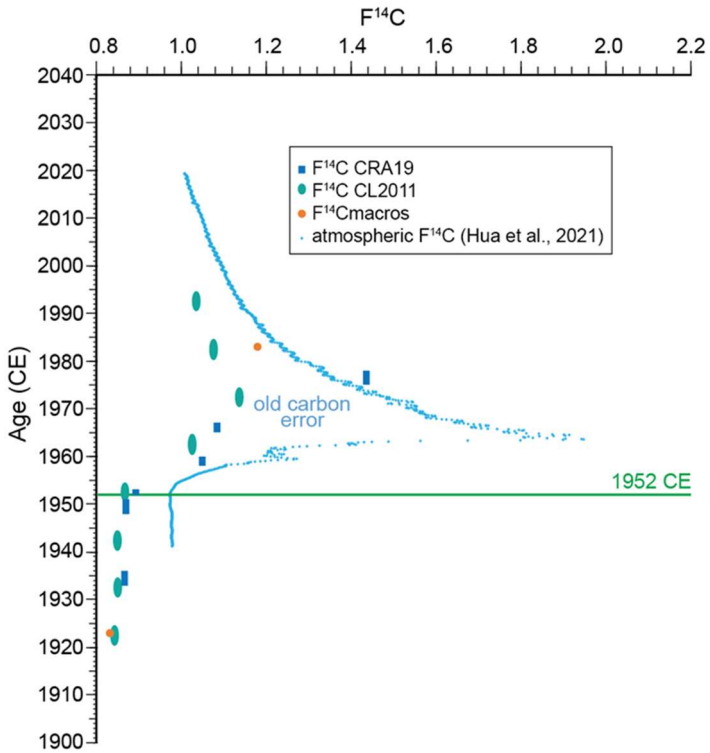

Figure CL5. Measurements of $F^{14}C$ increase after 1955 CE in varved sediments from Crawford Lake, mirroring the global atmospheric pattern (blue curve from Hua et al., 2021), although a strong old carbon effect was present in most samples, even in macrofossils. From McCarthy et al. (2023).

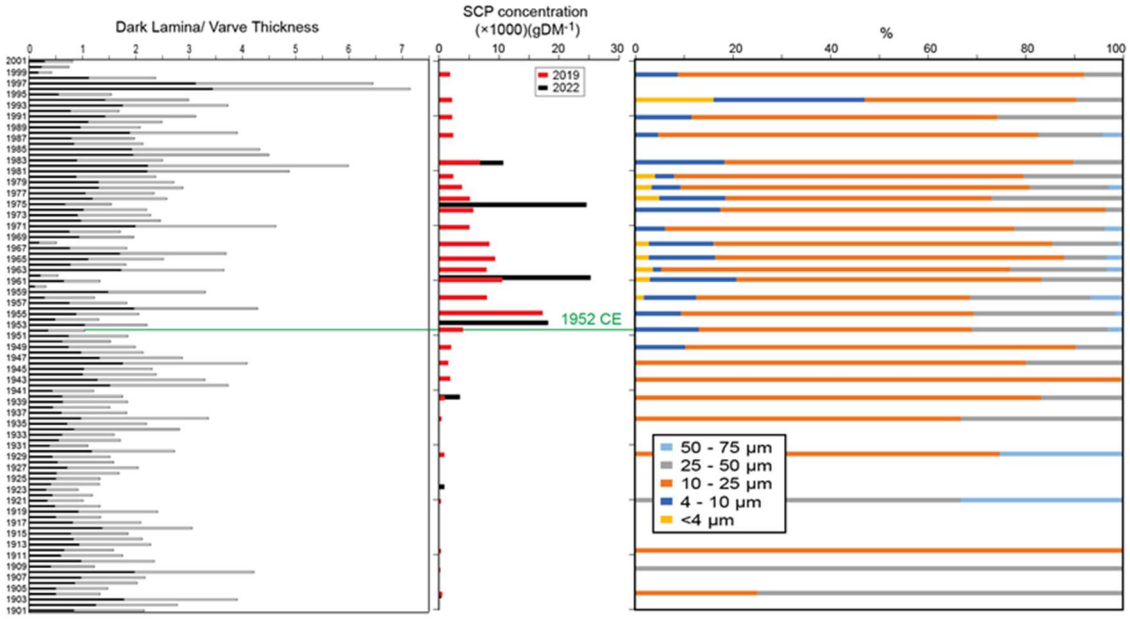

Figure CL6. Concentrations of spheroidal carbonaceous particles (SCPs) in freeze cores CRA19-2FT-B2 (red) and CRA22-1FR-A (black) compared with the relative thickness of the dark organic matter component in varves. SCP concentrations increase sharply in 1953 CE, reflecting a rapid increase in high temperature combustion of fossil fuels during the Great Acceleration. From McCarthy et al. (2024).

c) Increased heavy metal concentrations: µXRF analysis of freeze core CL-2011 shows a sharp increase beginning in 1948 CE for Cu, in 1950 CE (at 11.1 cm) for Pb, and in 1952 for Zn and for the elemental ratio Ti/Ca; all show peaks in the dark, calcite-poor sediments deposited through most of the 1950s–early 1970s (Figure CL7). The control exerted by lithology is clear, as the varves with prominent calcite laminae dated 1957, 1958 and 1959 CE show lower elemental concentrations and ratios. Highest activities attributed to metals also correlate with peak SCP concentrations (Figure CL6), consistent with combustion for steel production as the main source of heavy metals in the sediments of Crawford Lake. The gradual decline in heavy metal concentrations up-core reflects enactment of air quality legislation in North America in the 1970s.

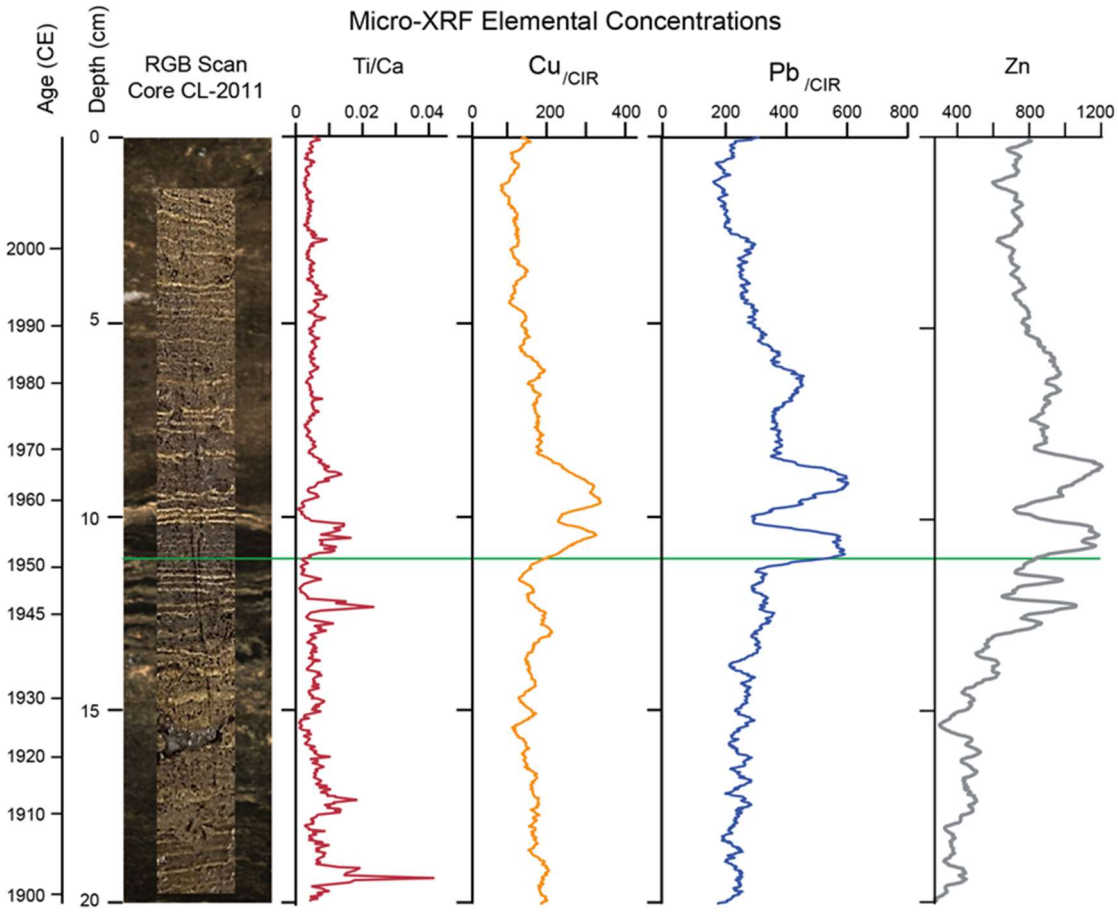

Figure CL7. Micro-XRF measurements of heavy metal elemental activities normalised to conservative elements (Si,Ca), total counts/second, or X-ray scatter (CIR) and ratios using ITRAX exhibit a sharp increase around the GSSP level, particularly in calcite-poor (high Ti/Ca) dark-coloured sediments separated by the sharp triplet of calcite laminae deposited in 1957, 1958 and 1959 CE. Peaks in Ti/Ca are attributed to increased terrigenous influx from increased erosion due to land disturbance and/ or increased precipitation and runoff from the small catchment. Heavy metals associated with fly ash are especially abundant in sediments deposited between 1952 (green line marking the proposed base of the Anthropocene) and 1980 CE. From McCarthy et al. (2024).

d) Detectable decline in $\delta^{15}N$ values attributable to industrial and motor vehicle emissions of NOx: A steady decline to lowest values of the 20th century in 1971 CE (2.70‰), compared to the 20th century mean (5.15‰, n=100) follows a gradual decline 1910–1954 CE (Figure CL8). Although analysis at annual resolution highlights the influence of lithology on organic proxies, with less depleted values in calcite-rich varves, nitrogen isotope data record increased fossil fuel combustion and production of chemical fertilisers using the Haber-Bosch method since 1910 CE.

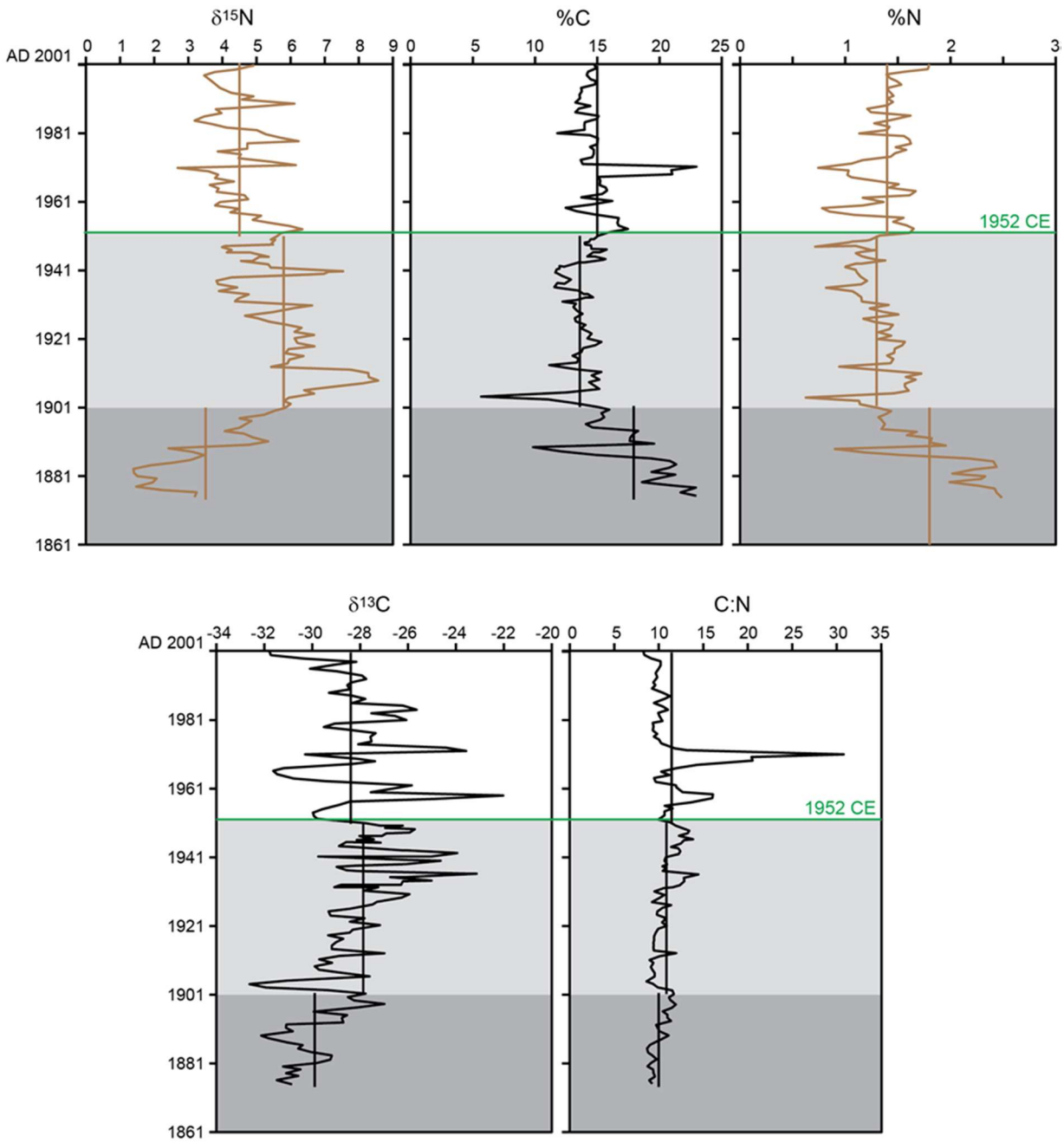

Figure CL8. Measurements of organic proxies in individual varves from core CRA23-2FT-A1. C:N ratios tend to hover around the mean in core CRA23-2FT-A until the mid-20th century when very high C:N ratios and less depleted values of $\delta^{13}C$ were measured in varves with prominent calcite laminae. Stable isotopes are most depleted in dark calcite-poor, highly organic sediments (mean %C=17.9%, %N=1.8%) deposited in the late 19th century, when a lumber mill operated on the south shore of the lake. The proposed Anthropocene epoch (above the green line, 1952 CE) is characterised by depleted values of $\delta^{15}N$ (mean ~1.3 ‰ lower than during the first half of the 20th century). Vertical lines illustrate mean values of organic proxies in individual varves during the late 19th C (dark grey shading), early 20th Century (light grey) and late 20th Century (no shading). From McCarthy et al. (2024).

e) Marked change in phytoplankton assemblages: analysis of siliceous microfossils and non-pollen palynomorphs records a sharp change in water column characteristics around 1952 CE that is attributed to the Great Acceleration as well as changes in the lake catchment (Figure CL9). Increases in deep-dwelling passive phytoplankton (scaled chrysophytes and *Botryococcus*) and non-planktonic diatoms are attributed to the effects of acid rain on pH and increased water clarity resulting from decreased calcite precipitation during the summer months. Increasing abundance of loricae of the chrysophyte genus *Dinobryon* and the diatom species *Asterionella formosa* upcore is attributed to warmer temperatures, particularly since the 1980s. The decline in the planktonic diatoms of the genus *Fragilaria* and species *Lindavia michiganiana*, and in exceptionally preserved cellulosic dinoflagellate thecae, record a decline in nutrients associated with abandonment of the lumber mill in 1900 CE.

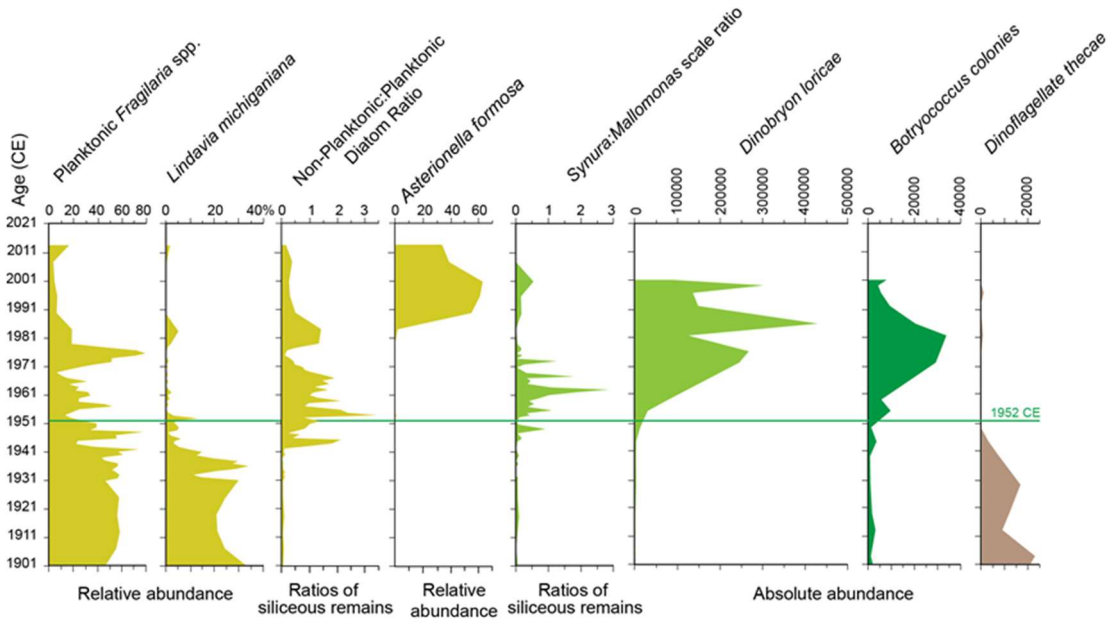

Figure CL9. A marked change in phytoplankton assemblages is recorded by diatoms (yellow), chrysophytes (light green), chlorophytes (dark green) and dinoflagellates (light brown) in varved sediments from Crawford Lake. Siliceous microfossils were analysed from individual varves between 1931 and 1991 CE in core CRA19-2FT-D1, at multiple varve resolution in core CRA19-2FT-B2 through the rest of the record. Non-pollen palynomorphs were analysed in centimetre-thick samples from the section of freeze core CL-2011 that was analysed using ITRAX.

f) Regional decline in elm (*Ulmus*) pollen and local decline in non-arboreal pollen in freeze core CL-2011 (Figure CL10). The decline in *Ulmus* from the mid-1950s is due to Dutch elm disease, whereas that of non-arboreal pollen, including ragweed (*Ambrosia*) relates to restoration of forests within the conservation area.

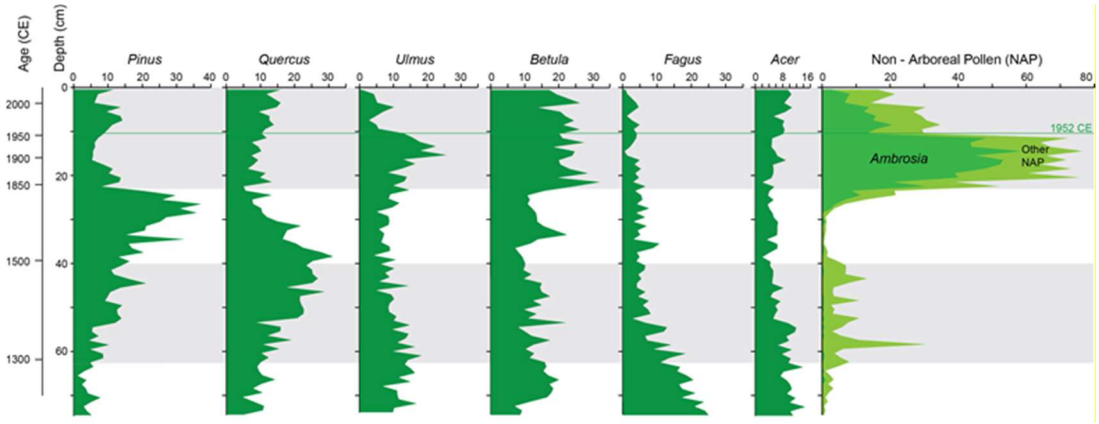

Figure CL10. Pollen spectra spanning the last ~800 years. Grey bands represent intervals of significant human impact in the area, firstly through introduction of Indigenous Agriculture ('Iroquoian' language group people) that spanned the late 13th through 15th centuries in containing abundant non-arboreal pollen (NAP). A second phase is associated with rapid land clearing marked by the rapid rise in Ambrosia *(ragweed) and other NAP from 1830–1840 CE, and the long tail associated with increased abundance of NAP (mainly grasses) below the* Ambrosia *rise is attributed to the emigration of United Empire Loyalists to the area following the American War of Independence (late 1770s–1780s). Following 1950 CE, restoration of forests in the area led to decreases in abundance of pollen from* Ambrosia *and other NAP and increased pollen from pine (*Pinus*), oak (*Quercus*) and maple (*Acer*) trees. The subsequent dramatic change is the rapid decline in elm (*Ulmus*) due to the westward spread of Dutch elm disease into the Great Lakes region. From McCarthy et al. (2023).*

3. THE PROPOSED STANDARD AUXILIARY BOUNDARY STRATOTYPES (SABSs)

Standard Auxiliary Boundary Stratotypes are a new concept detailed in Head *et al*. (2023c, d). These have a crucial role in supporting the GSSP by assisting global correlation, notably in different depositional environments. The guidance is that:

- The boundary interval of the primary guide be identified in the proposed SABSs without designation of a specific point, but with designation of a specific depth interval.
- The requirements for selected SABSs broadly conform to ICS guidelines for GSSPs, but can be applied with greater flexibility.
- SABSs will be the responsibility of the Working Group to propose, but will also require final approval by their respective subcommission (in this case, SQS).
- SABSs are intended to support a GSSP, so their approval cannot come into force until the GSSP has been ratified.
- SABSs can be included with a GSSP proposal, and also at a later date.
- As with a GSSP, selected SABSs will need to receive supermajority (60% or more) approval of the voting membership.
- There is no limit to how many SABSs can be selected, but Head *et al*. (2023c, d) advise on restraint on numbers to avoid a confusing proliferation. This will allow for future SABSs to be proposed in light of subsequent research.

The following three sites are submitted as candidate SABSs for the base of the proposed Crawfordian stage.

3.1 Beppu Bay, Japan

Project Leader and submission by Michinobu Kuwae.

Details of the proposed SABS core and of the site are provided by Kuwae *et al*. (2023).

1. Location and geological setting

Borehole core BMC21 S1-5 was collected on 21 June 2021 in Beppu Bay at a water depth of 71.1m (Figure BB1), located in northeastern Kyushu, Japan at 33.277800°N, 131.537333°E. Beppu Bay is a stable tectonic depression deepening towards the innermost part of the bay from a 50 m-deep sill at the bay mouth. This depression has received sedimentation for about 0.7 million years. Horizontal and vertical tidal mixing is suppressed in the deeper water below the depth of the sill with resultant thermal stratification, the deep area of the bay having seasonally oxygen-deficient bottom water below 60 m depth from June to December. As a result, varves have formed through the restriction of bioturbation by benthic organisms. Beppu Bay is surrounded by two cities, Beppu and Oita, and orchards in the north. The Ohno River, the Oita River, and the Asami River drain from catchments and through the cities before entering the bay.

2. *Lithology and indication in the field*

Each varve comprises a dark/low-density layer of organic matter including algae along with a pale/high-density detrital layer, with the combination representing one year. There are 16 age-known event layers in core BMC21 S1-5 (Figure BB2). A massive and thick flood event layer at 60.8–64.6 cm in BMC21 S1-5 and 56.4–60.7 cm in BMC19 S1-2 corresponds to the historically biggest flood event observed on 26th June 1953 in the Oita River and can be used as a reliable age control for the Anthropocene onset as described later. This is a distinctive bed within this part of the succession and is associated with upturns in many of the proxy signals. A minor flood layer from 1951 CE is also found at 65.3 cm depth in BMC21 S1-5. The onset of the Anthropocene as determined at the GSSP of the autumn of 1952 would occur between the two flood events. The base of the 1953 flood layer is the pragmatic level to place the base of the Anthropocene in this core, though the onset may occur a few mm beneath this boundary.

3. Accessibility

The core BMC21 S1-5 is vacuum-packed in a plastic bag and archived in cool storage (4℃) at the Center for Marine Environmental Studies (CMES), Ehime University, Matsuyama, Japan, but in 2024 will move to Kochi University. The core site is accessible by boat and there are no restrictions to the collection of additional cores. Several frozen samples including a gravity core (back to 1820 CE) and a 20 m-long core (BP15-1) (back to 7300 cal BP), and other cores are stored in the Environmental Specimen Bank for Global Monitoring (es-BANK) of CMES under strict thermal control. Samples in the es-BANK are open for researchers. BP15-1 comprises marine sediments throughout its length, with water depth comparable to modern levels, and

was dated by ^{14}C of marine and terrestrial materials. This core ensures that the succession has an investigated record extending far back into the Holocene and confirms that the nature of the Anthropocene succession is at variance to a lengthy run of Holocene sediments.

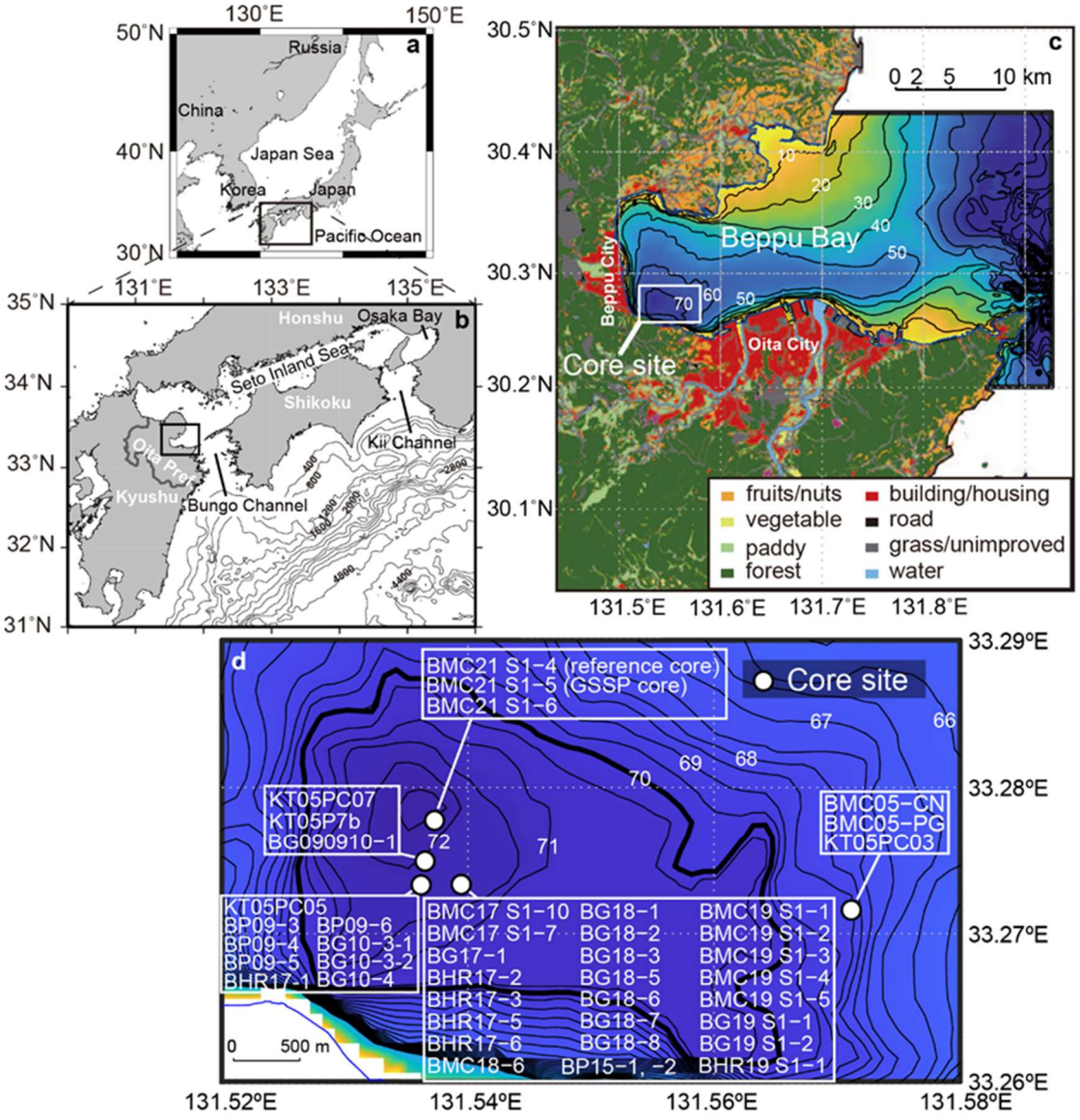

Figure BB1. Study area and core site. (a) study area in Japan; (b) Beppu Bay in the Seto Inland Sea in the open black rectangle in (a); (c) the surrounding land use; and (d) the core sites in the open white rectangle in (c). SABS core: BMC21 S1-5; the reference core: BMC21 S1-4. From Kuwae et al. (2023, fig. 1).

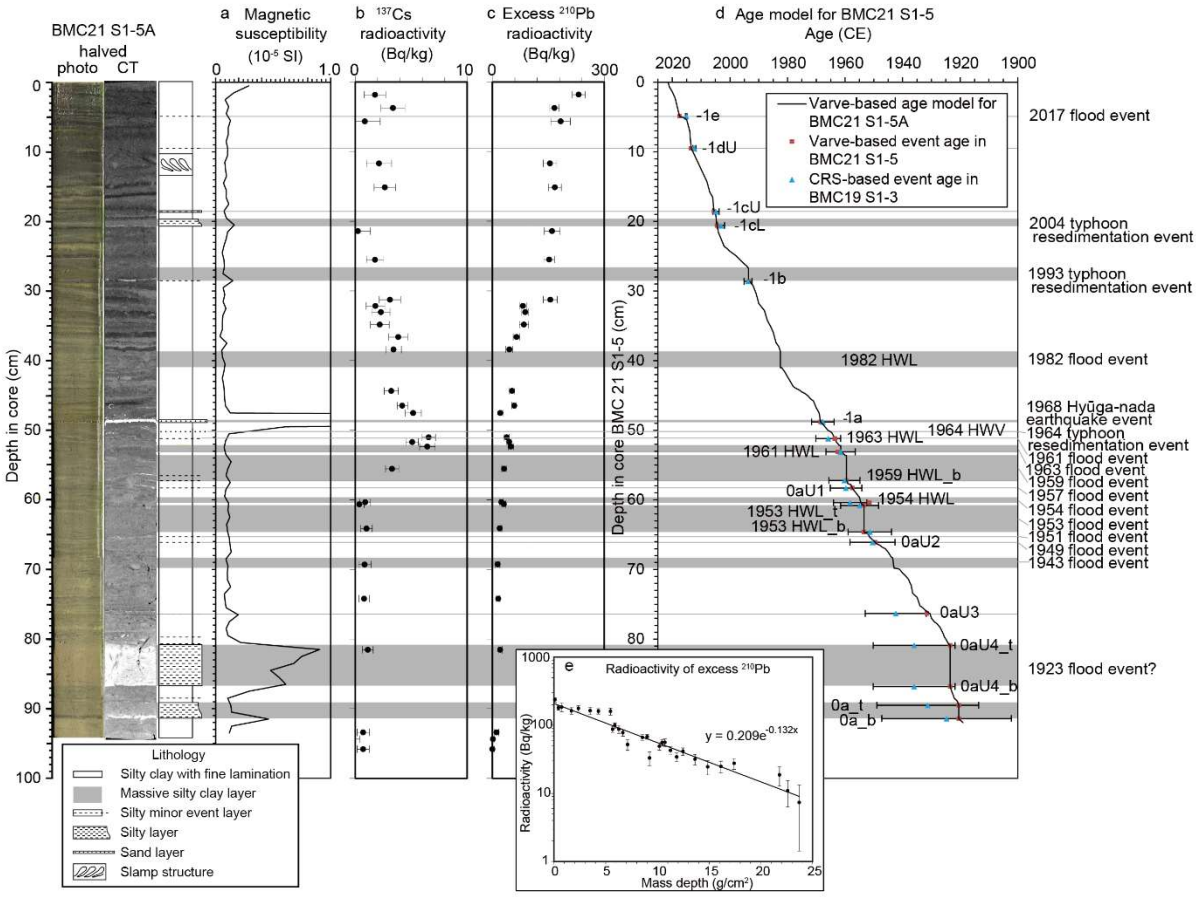

Figure BB2. Photo, CT, lithology, and magnetic susceptibility (a) of core BMC21 S1-5, ^{137}Cs (b) and excess ^{210}Pb radioactivity (c) and comparison between varve-based age model for core BMC21 S1-5 and ^{210}Pb-based age model for core BMC19 S1-3 (d). (e): radioactivity of excess ^{210}Pb against cumulative weight. The error bars in panels (b), (c), (d), and (e) show ±1SD errors. (d): age model (blue triangle) projected against the SABS core depth from that estimated from the constant rate of supply (CRS) model of excess ^{210}Pb data. From Kuwae et al. (2023, fig. 4).

4. Conservation

The cores are conserved as described above. The bay is not protected. The Japan Coast Guard agency requires work permit applications from developers for the bay, providing some protection of the core site from development.

5. Stratigraphic completeness of the section

The core comprises varve sediment that spans from 1916 to 2021 CE, with high sedimentation rates ranging from 0.6 to 1.8 cm/yr outside of event layers. There are potential year-long minor gaps beneath some event layers in the SABS core (1992 CE/28.6 cm layer below the 1993 CE high-wave event layer; 1968 CE/48.8 cm layer below the 1968 CE earthquake event layer) and a slump structure (2009–2012 CE/14.1–9.9 cm, but without any slump in the reference core BMC21 S1-4, located 30 cm distant from the SABS core) in the succession.

6. Age constraints

The core ages are determined by varve counting together with age-known event layers. Analysis of ^{210}Pb and ^{137}Cs provide cross-validation for the varve-counting results. Excess ^{210}Pb activities decrease exponentially with depth providing radiometric chronological reconstructions, independently calibrated by the ^{137}Cs peak (indicative of 1963 CE) at 50.5 cm depth (Figure BB2). The dark varve formed after spring 1952 CE occurs at a depth of 64.8 cm (marked in yellow + in Figure BB3). Event layers formed by floods, typhoon-induced high waves, and earthquakes provide 16 time constraints for this core. Ages of these event layers are consistent with those obtained from the constant rate of supply (CRS) model. The 1953 flood layer is consistent with the start of the Great Acceleration signature, indicated by the sharp increase in anthropogenic fingerprint above the layer as described below (Figure BB4p).

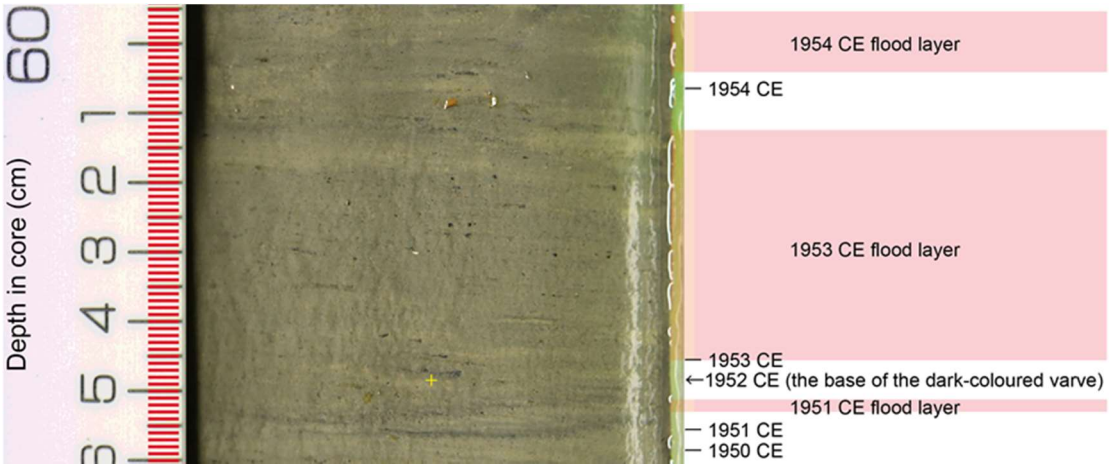

Figure BB3. Photo of core BMC21 S1-5 and the summer to autumn 1952 CE level (yellow +). The start of 1952 deposition is located at the base of the pale varve below the level.

7. Proxies that allow correlation with the base of the proposed Crawfordian stage GSSP

The GSSP interval is recognised within the 1952-dated varve at 64.8 cm depth. Correlation with the proposed base of the Crawfordian stage is marked in the core BMC21 S1-5 for this SABS proposal by the following:

a) The base of the plutonium bomb-spike: A rapid increase in $^{239+240}$Pu activities from 60.5 cm depth (corresponding to 1954 CE; Figure BB4b), and a further abrupt increase in ^{239}Pu+^{240}Pu at 58.5 cm (rd/cd), between the event layers 1954 HWL and 0 aU1 (1957 HWL; 57.5 cm) in core BMC21 S1-5, coincident with a spike of ^{239}Pu/^{240}Pu ratio. There is a large $^{239+240}$Pu peak at 51.5 cm (1963 CE), while $^{239+240}$Pu activities decrease above 49.5 cm depth (1967 CE) (Yokoyama *et al*., 2022; Kuwae *et al*., 2023);

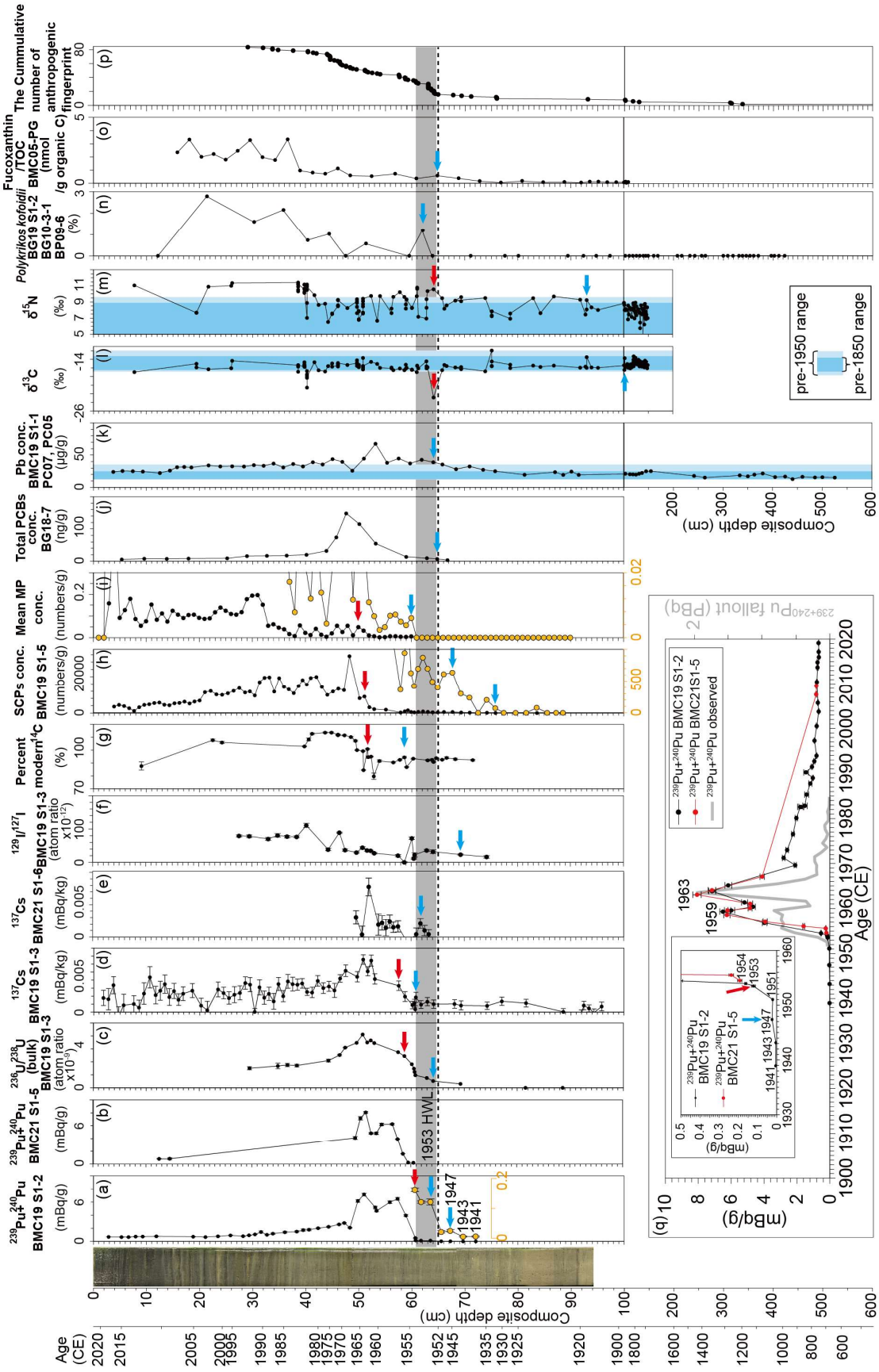
(a) 239+240Pu BMC19 S1-2 (mBq/g)
(b) 239Pu+240Pu BMC21 S1-5 (mBq/g)
(c) 236U/238U (bulk) BMC19 S1-3 (atom ratio x10-8)
(d) 137Cs BMC19 S1-3 (mBq/kg)
(e) 137Cs BMC21 S1-6 (mBq/kg)
(f) 129I/127I BMC19 S1-3 (atom ratio x10-12)
(g) Percent modern 14C (%)
(h) SCPs conc. BMC19 S1-5 (numbers/g)
(i) Mean MP conc. (numbers/g)
(j) Total PCBs conc. BG18-7 (ng/g)
(k) Pb conc. BMC19 S1-1 PC07, PC05 (µg/g)
(l) δ13C (‰)
(m) δ15N (‰)
Polykrikos kofoidii BG19 S1-2 BG10-3-1 BP09-6 (%)
Fucoxanthin /TOC BMC05-PG (nmol /g organic C)
The Cummulative number of anthropogenic fingerprint
1953 HWL
1947
1943
1941
pre-1950 range
pre-1850 range
Composite depth (cm)
Age (CE)
(q) 239+240Pu fallout (PBq)
239Pu+240Pu BMC19 S1-2
239Pu+240Pu BMC21S1-5
239Pu+240Pu observed
1963
1959
(mBq/g)

Figure BB4. [previous page] Variations of anthropogenic proxies versus depth and age in sediment cores from Beppu Bay. The core photo denotes the SABS core, BMC21 S1-5, which provides a standard depth scale for the upper sediment sequences (composite depth; not raw depth of each core). Depth scale of other cores was converted from raw depth to composite depth based on the event layer correlations and linear interpolation between the raw depth and composite depth of two successive event layers. Composite depth is the depth scale of a simple stack of master sections: the uppermost master section is from the core top to the base of the Event 0a (1920 CE) in BMC21 S1-5: with the second master section, from the base of Event 0a to the base of Event 0 (1711 CE) in BG10-3-1: and the third master section, if present, which is made up of lower sections in other cores like BP09-3. The light blue (red) arrow denotes the first (second) detection of an anthropogenic fingerprint. Grey shade denotes the 1953 CE flood layer: HWL - high water level. Dashed black line is 1952 CE varve level. (a) $^{239+240}$Pu activities in core BMC19 S1-2; (b) $^{239+240}$Pu activities in core BMC21 S1-5; (c) ^{236}U/^{238}U activity ratios in core BMC19 S1-3; (d) ^{137}Cs activities in core BMC19 S1-3; (e) ^{137}Cs activities in core BMC21 S1-5; (f) ^{129}I/^{127}I ratios in core BMC19 S1-3; (g) percent modern ^{14}C in multiple cores; (h) SCP concentrations in BMC19 S1-5; (i) mean microplastic concentrations in multiple cores; (j) total PCB concentrations in core BG18-7; (k) lead concentrations in cores BMC19 S1-1, PC07 and PC05; (l) δ^{13}C and (m) δ^{15}N of fish scales in multiple cores; (n) relative abundance of Polykrikos kofoidii *(dinoflagellate) in cores BG19 S1-2, BG10-3-1 and BP09-6; (o) Fucoxanthin/organic carbon ratio in core BMC05-PG; (p) the cumulative number of anthropogenic finger-prints and (q) temporal variations in the plutonium records and an observed record from Hancock et al. (2014). Orange circle in several panels denotes the same as the black circle at the corresponding depth, but enlarged on the horizontal scale. Modified from Kuwae et al. (2023, fig. 17).*

Additional proxies from additional cores from the same locality:

b) The base of the plutonium bomb-spike: A slight increase in $^{239+240}$Pu activities starts from 59.5 cm raw depth (63.5 cm in composite depth, cd; Figure BB4a) in the event layer 1953 HWL in core BMC19 S1-2. This occurs above an initial increase at 63.5 cm in rd (67.3 cm in cd, 1947 CE) and base level at 67.5-65.5 cm rd (72.1-69.7 cm cd in 1938-1943 CE). The records also show an abrupt increase in ^{239}Pu+^{240}Pu between the event layers 1954 HWL and 0 aU1 (1957 HWL) in BMC19 S1-2 at 53.5 cm rd (58.9 cm cd), coincident with a spike of ^{239}Pu/^{240}Pu ratio. A large $^{239+240}$Pu peak at 51.5 cm (1963 CE) while $^{239+240}$Pu activities decrease rapidly and to a consistently low level above 45.5 cm depth (1969 CE) (Yokoyama *et al*., 2022; Kuwae *et al*., 2023). Core BMC19 S1-2 (as well as BMC21 S1-5) shows an earlier peak (1958–1959 CE; Figure BB4a and 2b) prior to the primary peak in 1963 CE and a successive decrease in $^{239+240}$Pu activities in 1960–1961 CE, the latter corresponding to the moratorium on nuclear testing (UNSCEAR, 2000). These temporal patterns with the upturn in 1953 CE were consistent with those in the observed record of plutonium fallout (Hancock *et al*., 2014; Figure BB4q);

c) The base of the uranium bomb-spike: A rapid increase in a ratio of ^{236}U/^{238}U is present from 62.5 cm depth (corresponding to 1953 CE; Figure BB4c) in core BMC19 S1-3, with a large ^{236}U/^{238}U peak at 50.5 cm (1964 CE) while the ratios

decrease rapidly and to a consistently low level above 44.5 cm depth (1976 CE) (Kuwae *et al*., 2023; Takahashi *et al*., 2023);

d) The base of the caesium bomb-spike: ^{137}Cs activity increases slightly above 59.4 cm depth (corresponding to 1953 CE; Figure BB4d), rapidly increases above 55.5 cm depth in core BMC19 S1-3 (1956 CE), with a large ^{137}Cs peak at 50.5 cm (1964 CE) and decreases rapidly and to a consistently low level above 45.5 cm depth (1974 CE);

e) The base of the caesium bomb-spike: ^{137}Cs activity increases slightly above 59.5 cm depth (corresponding to 1953 CE; Figure BB4e), with a large ^{137}Cs peak at 50.5 cm (1963 CE) in core BMC21 S1-6, while the activities decreased rapidly at 48.5 cm depth (1966 CE; Figure BB4e);

f) Increase in artificial radiogenic iodine: ^{129}I/^{127}I ratios in core BMC19 S1-3 increases slightly at 66.5 cm (1943 CE; Figure BB4f), then increases irregularly, with higher values in the 1953 CE layer;

g) The base of the percent modern ^{14}C bomb-spike: A percent modern ^{14}C (pM^{14}C) activity in anchovy fish scales, reconstructed from cores BG19 S1-1, BMC19 S1-3, BG18-2, and BG18-3, shows an initial increase at 37.5 cm in core BG19 S1-1 (1957 CE; Figure BB4g), as well as an abrupt increase at 51.5 cm in core BMC19 S1-3 (1963 CE). pM^{14}C shows a broad peak from 29.5 to 23.5 cm in BG19 S1-1 (1968–1982 CE; Figure BB4g), while it shows moderate levels at 16.5 cm in core BG18-3 (1982 CE) and from 22.5 to 7.5 cm in core BG19 S1-1 (1982–2001 CE), and low levels at 1.5 cm (2014 CE);

h) Increase in spheroidal carbonaceous particles (SCPs) in core BMC19 S1-5: Constant and low SCP concentrations occur below 70.5 cm depth (before 1929 CE; Figure BB4h) (Inoue *et al*., 2022; Kuwae *et al*., 2023). A slight SCP increase occurs above 69.5 cm depth (after 1932 CE) with a minor abrupt increase above 64.5 cm depth (after 1946 CE). SCP concentrations increase markedly above 49.5 cm (after 1964 CE) with the highest value at 46.5 cm (1969 CE; Figure BB4h);

i) Lowest detection of microplastic particles in cores BG18-1, -2, -3, -4, and -5, BHR17-2, -3, -5, and -6, BMC19 S1-4, and BHR19 S1-1: The lowest level of detection of a microplastic particle is at 22.5 cm in BG18-4 (1954 CE; Figure BB4i), with an abrupt increase at 49.5 cm in BMC19 S1-4 (1966 CE) (Hinata *et al*., 2023; Kuwae *et al*., 2023);

j) Lowest detection of total polychlorinated biphenyls (PCBs) in core BG18-7: The lowest level of detection of PCBs is at 28.5 cm (1953 CE; Figure BB4j), with an abrupt increase at 22.5 cm (1963 CE) (Takahashi *et al*., 2020; Kuwae *et al.,* 2023);

k) Increase in bulk heavy metal concentrations in BMC19 S1-1, PC07, and PC05: Elemental concentrations for the last 1300 years show an abrupt shift at 61.5 cm in BMC19 S1-1 (1953 CE), corresponding to increases in concentrations of Cu, Zn, As, Sb, Hg, Pb, and Bi (only Pb shown in Figure BB4k) (Kuwae *et al*., 2022, 2023). This indicates intensified mining activity around the bay;

l) Increase in δ^{13}C values in anchovy fish scales in cores BG10-3-2, BG10-4, BG17-1, BMC17 S1-7, BG18-2, -3, -4, and -5, BMC19 S1-3 and BG19 S1-1: The lowest occurrence exceeding the out-of-range δ^{13}C values between 1660 and 1850 CE is at 62.5 cm in core BG17-1 (1888 CE; Figure BB4l). The lowest occurrence of a

low $\delta^{13}C$ value exceeding the $\delta^{13}C$ ranges between 1660 and 1950 CE is at 62.5 cm in core BMC19 S1-3 (1953 CE). This reflects an increase in fossil fuel burning;

m) Increase in $\delta^{15}N$ values in anchovy fish scales in cores BG10-3-2, BG10-4, BMC17 S1-7, BG18-2, -3, -4, and -5, BMC19 S1-3, and BF19 S1-1: The lowest occurrence of high $\delta^{15}N$ values exceeding the $\delta^{15}N$ range between 1660 and 1850 CE is at 33 cm in core BG10-4 (1917 CE; Figure BB4m) (Kuwae *et al*., 2023). The lowest occurrence of high $\delta^{15}N$ values exceeding the $\delta^{15}N$ ranges between 1660 and 1950 CE is at 62.5 cm in core BMC19 S1-3 (1953 CE). The elevated $\delta^{15}N$ after 1953 CE may be attributed to the increased supply of terrestrial denitrification-derived ^{15}N-rich reactive nitrogen into the coastal waters due to the increased use of airborne-derived nitrogen fertiliser by farms.

n) Lowest detection of red-tide-associated dinoflagellate species *Polykrikos kofoidii* at 36.5 cm depth in BG19 S1-2 (1953 CE; Figure BB4n) (Matsuoka *et al.*, 2022; Kuwae *et al*., 2023), indicating an increase in red tides in the bay due to increased fertiliser-derived reactive nitrogen supply;

o) Increase in algal pigments in core BMC05-PG: Algal pigment compositions (fucoxanthin, chlorophyll-b and pheophytin-b, β-carotene, etc., normalised to total organic carbon) show an initial major change at 37.0 cm (1950 CE; only fucoxanthin shown in Figure BB4o) with an initial increase in fucoxanthin/organic carbon ratio, indicating an increased abundance of dinoflagellates and/or diatoms (Kuwae *et al*., 2022, 2023);

p) Increase in persistent organic pollutants, POPs dichloro-diphenyl-dichloroethylene (DDE) and alpha-hexachlorocyclohexane (α-HCH), polycyclic aromatic hydrocarbons (PAHs) chrysene + triphenylene, fluoranthene, anthracene, 1,4-dichlorobenzene, 4-methyl-2,6-di-t-butylphenol: Concentrations in dichloro-diphenyl-trichloroethane (DDT) derivatives (DDE) and PAHs (chrysene + triphenylene, fluoranthene and anthracene) show an initial increase at 28 cm depth in core BG18-7 (1953 CE; Figure BB5) (Nishimuta *et al*., 2020; Kuwae *et al*., 2023). α-HCH, 1,4-dichlorobenzene, and 4-methyl-2,6-di-t-butylphenol were first detected at 28 cm depth in core BG18-7 (1953 CE; Figure BB5). The increase in DDE and α-HCH concentrations indicates the start of the use of pesticides in the catchments around the bay;

q) Increase in biogenic opal in core BG17-1: Biogenic opal concentrations show an initial increase at 37 cm depth (1953 CE; Figure BB5) (Kuwae *et al*., 2022, 2023);

r) Increase in Ni content in core BG17-1: Water content-corrected Ni, measured by a micro-X-ray fluorescence spectrometer (ITRAX), shows an initial increase at 37 cm depth (1953 CE; Figure BB5), indicating an increase in diatom frustules which contain abundant Ni (Kuwae *et al*., 2022, 2023);

s) Decrease in the authigenic Re/Mo ratio in BMC19 S1-1: Authigenic Re/Mo ratio decreases at 57.5 cm depth (1954 CE; Figure BB5), indicating start of enhanced anoxic conditions in the innermost/deepest area of the bay;

t) Lowest lithological change in BG17-1: ITRAX-derived element compositions show a major change at 35.6 cm (1953 CE; Figure BB5), associated with the signature of enhanced anoxic conditions (authigenic Re/Mo) and an increase in algal abundance (opal, Ni, and fucoxanthin);

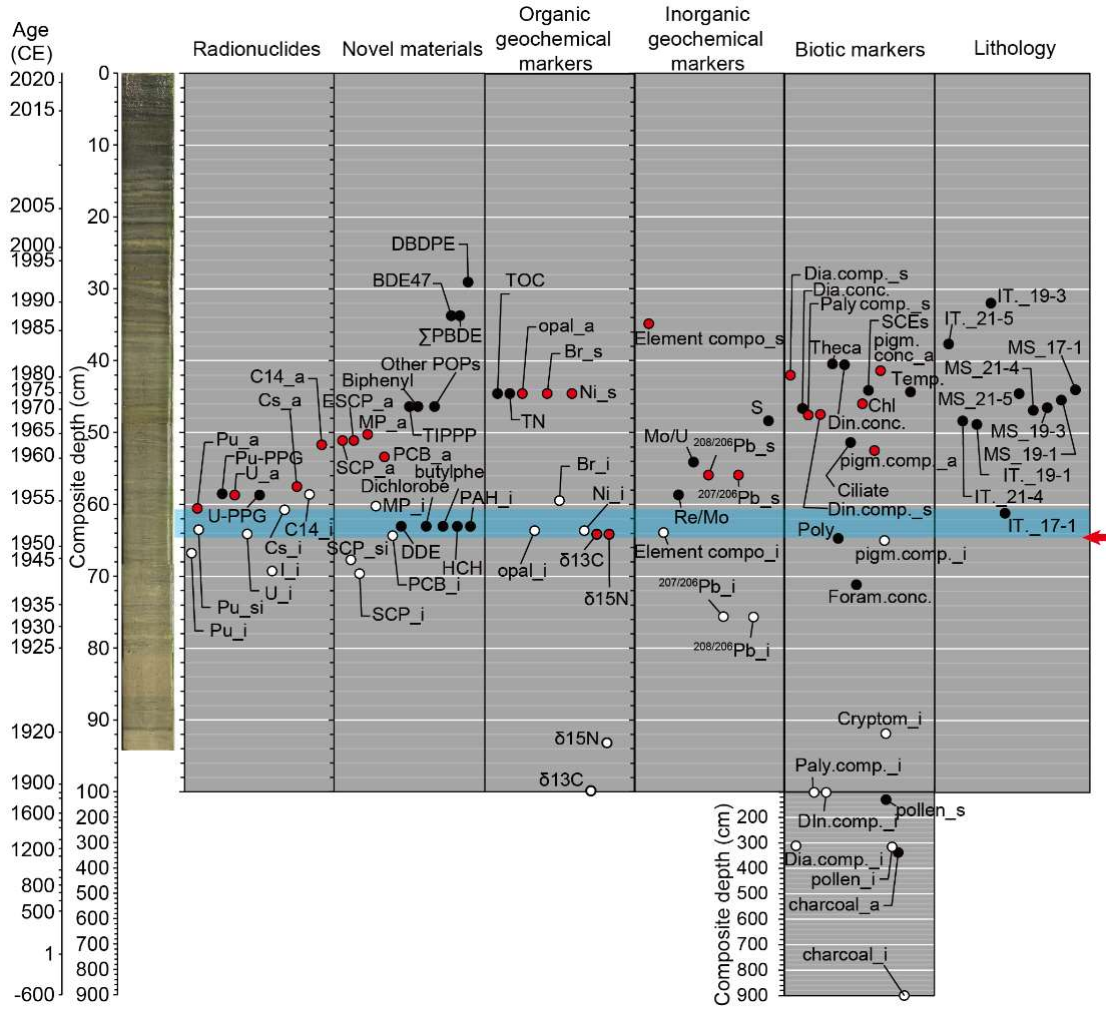

Figure BB5. The detected levels of anthropogenic fingerprints in the Beppu Bay succession. Closed white circle denotes a lowest occurrence level of the anthropogenic fingerprint detected for a given marker (named as e.g., Pu_i for an initial detection of the signature in 1947 CE, followed by Pu_si for a slight increase in 1953 CE). Closed red circle denotes the secondary change level (e.g., Br_s) or the abrupt change level (e.g., Pu_a) for the given marker. Closed black circle denotes an occurrence level of the first detection or unprecedented change in the marker record. Pu: plutonium, U: uranium, I: iodine, Cs: caesium, C14: carbon-14, PPG: Pacific Proving Ground, butylphe: 4-methyl-2,6-di-t-butylphenol, dichlotobe: 1,4-dichlorobenzene, HCH: α-HCH, PAH: chrysene + triphenylene, fluoranthene, and anthracene, SCP: spheroidal carbonaceous particles, ESCP: elemental compositions of SCPs, MP: microplastics, DDE: DDT derivatives, PCB: total PCBs, BDE/∑PBDE/DBEPE: chemicals of brominated flame retardants, Element compo: Element compositions, Re/Mo: rhenium/molybdenum ratio, Mo/U: molybdenum/uranium ratio, $^{207/206}$Pb and $^{208/206}$Pb: lead isotope ratio, opal: biogenic opal, δ13C and δ15N: stable carbon and nitrogen isotope ratio of anchovy scales, Br and Ni: bromine and nickel contents, TOC: total organic carbon, TN: total nitrogen, S: total sulfur, dia. comp.: diatom compositions, Paly. comp.: marine palynomorph compositions except for dinoflagellates, Din. comp.: dinoflagellate compositions, Poly: Polykrikos kofoidii *concentrations, Theca: Testate amoeba concentrations, Pollen: pollen grain compositions, Cryptom:* Cryptomeria

japonica *pollen grain deposition rates, Foram conc.: benthic foraminifer concentrations, Dia. conc.: diatom concentrations, pigm. comp.: pigment compositions, Din. conc.: dinoflagellate concentrations, Chl: chlorophyll a concentrations, SCEs: steryl chlorine esters, Temp: spring air temperatures, pigm. conc.: pigment concentrations, Ciliate: ciliates, IT (with core ID): element compositions analysed by ITRAX, MS (with core ID): magnetic susceptibility. Horizontal light blue shade denotes the 1953 CE flood event layer and red arrow denotes the level above which a sharp increase in the number of anthropogenic fingerprints occurs. From Kuwae et al. (2023, fig. 5).*

u) Sharp increase in the number of anthropogenic fingerprints (all cores in which an anthropogenic fingerprint was detected): Figure BB5 shows levels of occurrences of anthropogenic fingerprints including those around 1950 CE as mentioned in a)—t) and others. Anthropogenic fingerprints were rare between the 1953 flood event layer at 64.6–60.8 cm composite depth (1953 CE) and 900 cm composite depth (620 BCE). In contrast, anthropogenic fingerprints including radionuclides, novel materials, geochemical markers, and biotic markers were abundant between 1953 and 1993 CE, reflecting the Great Acceleration signature in the strata. An inflexion point of the cumulative number of anthropogenic fingerprints was detected at the level of the 1953 CE flood layer (Figure BB4p).

3.2 Sihailongwan Maar Lake, China

Details of the proposed SABS core and of the site are provided by Han *et al*. (2023).

1. Location and geological setting

Freeze core SHLW21-Fr-13, along with another 23 parallel freeze cores, was collected in February 2021 from a water depth of 50 m in Sihailongwan Maar Lake, located in Jingyu County, Jilin Province in northeast China at 42.286881°N, 126.601247°E. Sihailongwan Maar Lake is a near-circular low-rimmed volcanic crater lake (or maar lake, Figure SHL1) with a diameter of ~750 m that is relatively deep for its size (maximum depth of ~50 m). Thermal stratification in such deep waters under warmer water temperatures, together with possibly decreasing dissolved oxygen concentrations over time, has led to lowering of dissolved oxygen concentrations over the past 70 years, in turn leading to the deposition of undisturbed dark organic-rich laminae seen in the upper parts of the cores.

Sihailongwan Maar Lake is located in a relatively remote area with little human disturbance and is now a part of the Jilin Longwan National Nature Reserve in northeast China. It is distant from any large cities and is not impacted by any industrial activities in the surrounding area (>200 km) or local pollution to the lake. There are a further seven small maar lakes near to Sihailongwan Maar Lake (within 30 km), providing together abundant materials for scientific research (Figure SHL1).

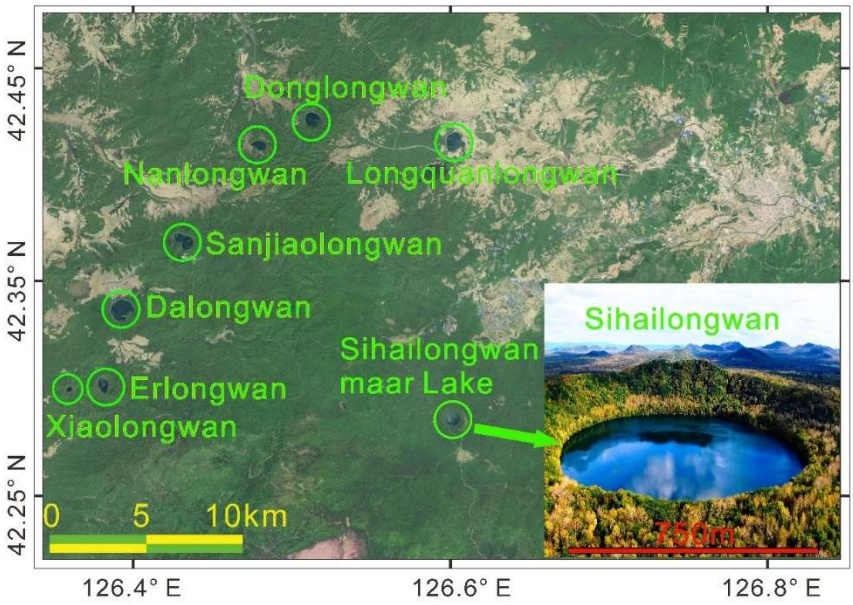

Figure SHL1. The location of Sihailongwan Maar Lake and other maar lakes in the Longwan volcanic region, Jilin Province of NE China. Figure from Han et al. (2023).

2. *Lithology and indication in the field*

Each varve comprises a dark layer of organic matter including algae along with a pale detrital layer, with the combination representing 1 year. There is a gradual colour change from yellow in the lower parts of the core to alternating dark-yellow bands and then to darker colours in the upper sections (Figure SHL2). The alternating dark-yellow layers begin at a depth of 85 mm (dated at 1955–1956 CE). There are two distinct siliciclastic marker layers occurring at depths of 61 mm (1977–1978 CE) and 75 mm (1963–1964 CE). These markers have been found between 55–65 and 70–80 mm depth in all cores.

3. Accessibility

Several freeze cores are archived in the cold storage Core Repository at the Institute of Earth Environment, Chinese Academy of Sciences (IEECAS) in Xi'an, China. Public visits and scientific collaborations using these cores are welcome. A paved road connects Jingyu County with Sihailongwan Maar Lake, allowing recollection of future cores following permission from the relevant management department of Sihailongwan Maar Lake.

4. Conservation

The cores are conserved as described above. Sihailongwan Maar Lake is located inside the Jilin Longwan National Natural Reserve (JLWNNR) in a remote and pristine area. The Longwan Natural Reserve was established in 1991, and upgraded as a national Nature Reserve in 2003. The reserve area is protected from any industrial and agriculture activities, with little human disturbance or pollution in the area.

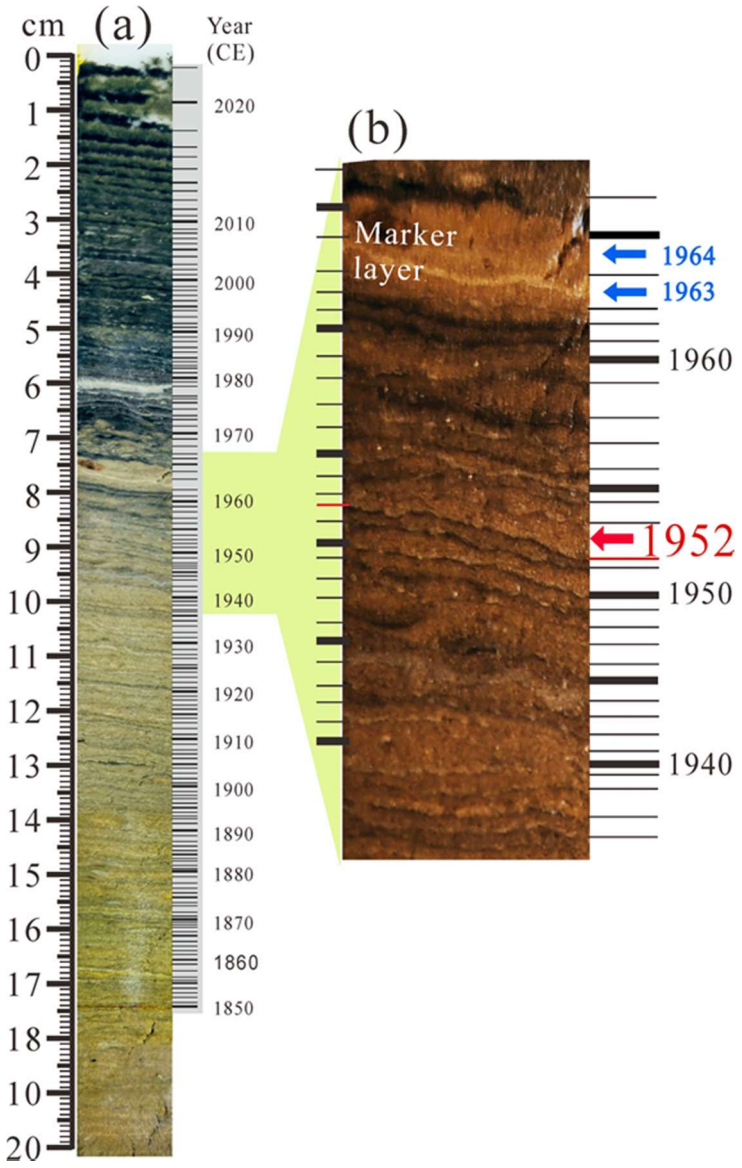

Figure SHL2. Core SHLW21-Fr-13 showing prominent colour change and annual varves. (a) Varve counting results of depth versus age; (b) Enlarged picture of varves representing 1935–1965 CE, with enhanced contrast ratio brightness. From figure 2 of Han et al. (2023). Blue arrows show a siliciclastic marker layer in 1963–1964.

5. Stratigraphic completeness of the section

There are no river inlets and outlets to the lake, and the sediments are almost entirely from atmospheric deposition and biotic accumulation from the water column. The core comprises varves that span from 1808 to 2020 CE, with an average sedimentation rate of ~1 mm/yr. The combination of varve-counting and radiometric analysis and the lack of facies change in the core suggests that there are no gaps in the succession.

6. Age constraints

The core ages studied here are determined by varve counting using core images and thin-sections, and cross-checking was conducted among parallel cores. Analysis of ^{210}Pb, ^{137}Cs and ^{226}Ra provide cross-validation for the varve-counting results. Excess

^{210}Pb (^{210}Pb$_{ex}$) activities decrease exponentially with depth providing radiometric chronological reconstructions, independently calibrated by the ^{137}Cs onset (indicative of 1953 CE) and peak (indicative of 1964 CE), at 88 mm and 77 mm depth, respectively. A comparison of radionuclide dating and varve counting shows comparable results for the post-1940 CE period (above 97 mm) and the chronology has no uncertainty. However, at lower depths (below 97 mm), the radiometric dating tends to have relatively older ages compared with the varve counting results and at the lowest core depth (200 mm, 1808 CE) the uncertainty is ± 3 years. Considering the accuracy in annual time resolution, independence of the varve counting results and the relative high dating uncertainty of ^{210}Pb for the older sediments, the varve-counting method is chosen for the chronology. Extensive deforestation over the Longwan region in 1977/1978 CE coincides with the upper siliciclastic marker layer at 61 mm depth.

7. Proxies that allow correlation with the base of the proposed Crawfordian stage GSSP

The base of the Crawfordian stage is recognised within the 1952-dated varve at 89 mm depth. Correlation with the proposed base of the Crawfordian stage is marked in the core SHLW21-Fr-13 for this SABS proposal by the following:

a) The base of the plutonium bomb-spike: A rapid increase in $^{239+240}$Pu activities from 88 mm depth (corresponding to 1953 CE; Figure SHL3a), with a large $^{239+240}$Pu peak at 79 mm (1963 CE) while $^{239+240}$Pu activities decreased rapidly and to a consistently low level above ~67 mm depth (1970 CE). Measured ^{240}Pu/^{239}Pu atomic ratios in most samples were in the range of global fallout (0.180 ± 0.014; Figure SHL3b). These dates are consistent with annual global detonation yields from above-ground nuclear weapons testing of thermonuclear devices since 1952 CE, with a global 1–2 year lag for deposition given average retention time of radionuclides injected to the stratosphere here is 18 months (UNSCEAR, 2000). Note that fallout of $^{239+240}$Pu is not only from thermonuclear detonation (hydrogen bomb), but also from uranium (atomic) bombs. There are total 18 tests in 1951 (mostly at high latitude) and 11 tests in 1952, including the first thermonuclear detonation at Enewetak, Pacific on 1st November 1952. The contribution of the first thermonuclear test might not be the dominant contribution all over the world, especially to high latitude regions;

Additional proxies from additional cores from the same locality:

b) A marked upturn in the fraction of the soot component attributable to fossil fuel (FF) burning (SHLW21-Fr-1); this was determined via the resulting dilution in ^{14}C values (measured as F^{14}C: Figure SHL3d). FF soot increased from 10% to 25% in the 120–86 mm depth range (1910–1950 CE), increased rapidly after 1950 CE and reached a peak of ~60% at 72 mm depth (~1964 CE), then decreased from 1966 CE, with the lowest values at 52 mm depth (1978 CE);

c) Marked increase in ^{129}I activities and ^{129}I/^{127}I ratios (core SHLW21-Fr-7): ^{129}I concentrations are very low (1.3×10^8 atoms/g) below 88 mm depth (before 1950 CE). Above 88 mm depth (1950 CE), ^{129}I activities and ^{129}I/^{127}I ratios increased by two orders of magnitude compared to the pre-nuclear level, initially reflecting the

bomb-spike (Figure SHL3c). From 78 to 44 mm depth (1960s to early 1990s), ^{129}I showed large fluctuations superimposed on a persistent $^{129}I/^{127}I$ increase related to releases from nuclear fuel reprocessing plants;

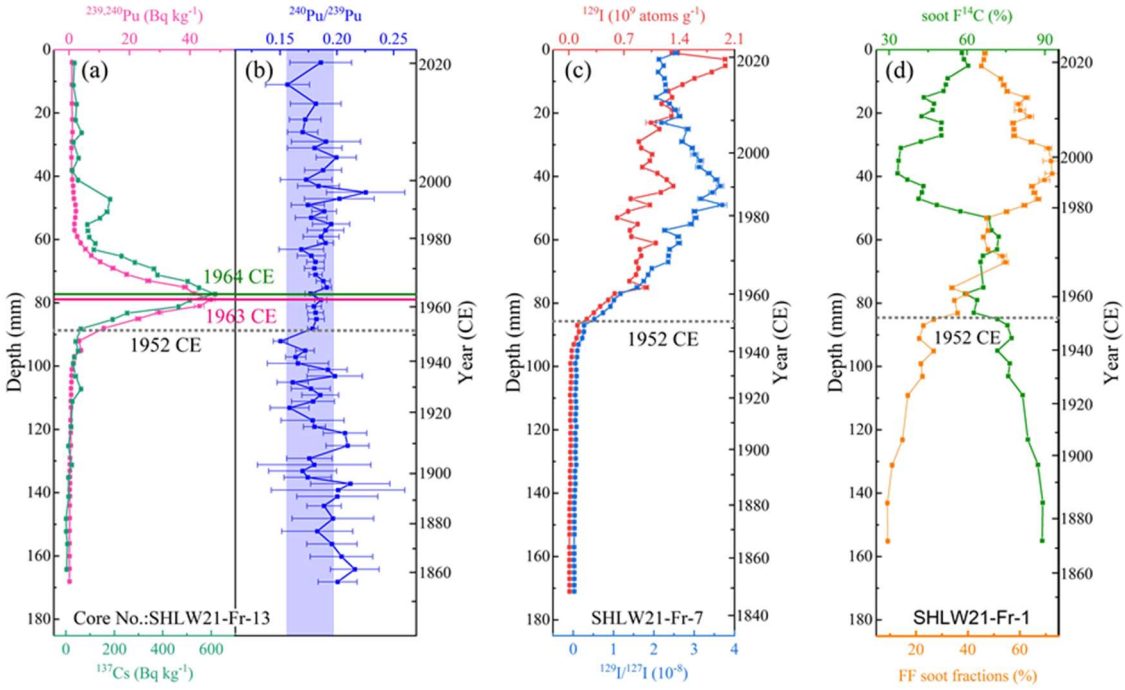

Figure SHL3. Variations of radionuclide activities versus depth and age in sediment cores from Sihailongwan Maar Lake. (a) $^{239+240}Pu$ and ^{137}Cs activity concentrations; (b) $^{240}Pu/^{239}Pu$ ratios in core SHLW21-Fr-13; (c) ^{129}I and $^{129}I/^{127}I$ in core SHLW21-Fr-7; (d) Soot $F^{14}C$ and calculated fossil fuel (FF) soot fractions in core SHLW21-Fr-1. Error bars of the proxies in the figures indicate uncertainties. The horizontal dotted line indicates the year 1952 CE, highlighting the rapid increase in $^{239+240}Pu$ and ^{129}I activities at that time. The vertical light blue area in panel (b) indicates the range of global fallout $^{240}Pu/^{239}Pu$ (0.180 ± 0.014). From figure 4 of Han et al. (2023). Each varve layer in the SHLW lake sediment core from 1945-1977 (77-101 mm), i.e. 23 samples, were analysed for $^{239+240}Pu$. Each varve is ~1mm thick and reported depths relates to mid-points of layers.

d) Marked increase in spheroidal carbonaceous particles (SCPs) (core SHLW21-Fr-1): SCP are absent below 93 mm depth (before ~1940 CE) with a rapid increase in concentration and flux above a depth of 86 mm (1950 CE; Figure SHL4a). The highest concentrations and fluxes are at 42 mm depth (early 1990s). The SCPs profile is similar to that for the FF soot fraction;

e) Increase in polycyclic aromatic hydrocarbons (PAHs) (core SHLW20-6): The sum of 16 parent (unsubstituted) PAHs (Figure SHL4b), high-molecular weight (HMW; Figure SHL4c) and low-molecular-weight (LMW; Figure SHL4d) PAHs. These all show constant and low concentrations below 86 mm depth (before 1950 CE) then start to increase, reaching a plateau in the depth interval from 67 to 55 mm (late 1960s to late 1970s). After that period, they continue to increase and peak at 38

mm depth (end of the 20th century). The overall PAH profiles with depth are very similar to those of FF soot fractions and SCPs;

f) Increase in black carbon soot particles (core SHLW21-Fr-1): Constant and low soot concentrations occur below 86 mm depth (before 1950 CE; Figure SHL4f). An overall increasing soot trend occurs above 86 mm depth (after 1950 CE), while char decreases. The highest soot concentration is at 35 mm depth (1997 CE), followed by an overall decrease;

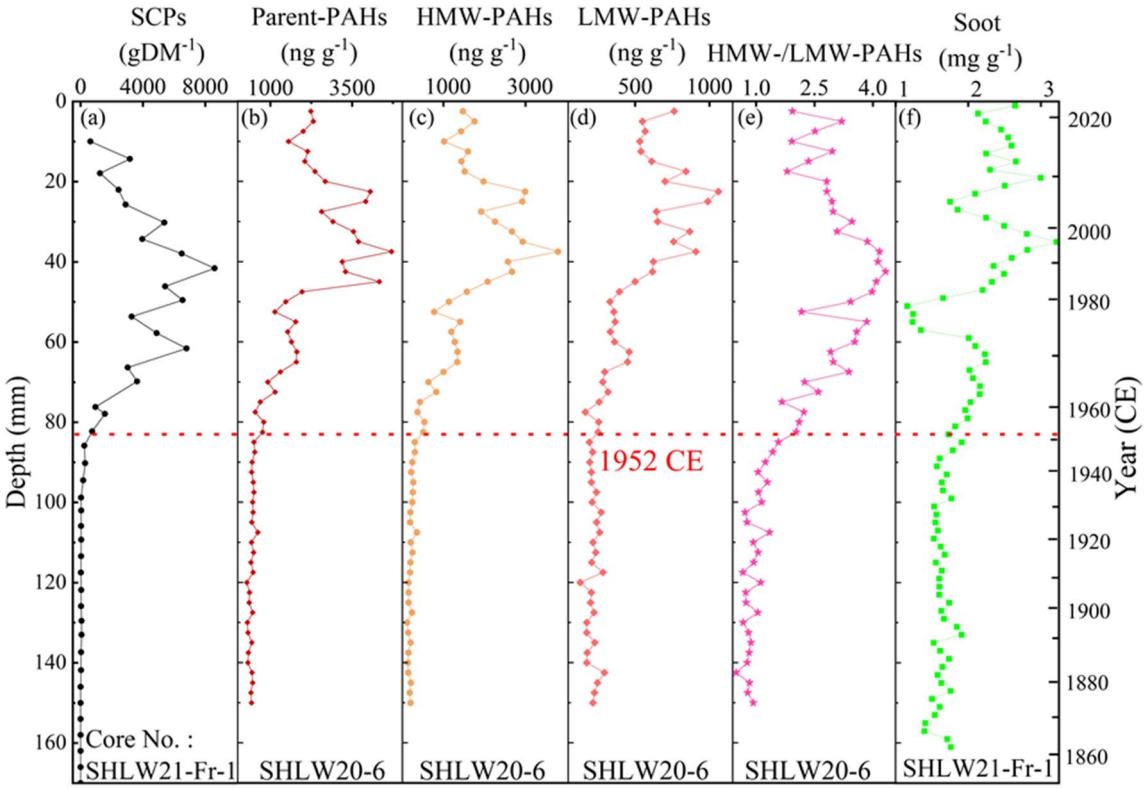

Figure SHL4. Variations in combustion-product novel materials versus depth and age in sediment cores from Sihailongwan Maar Lake. (a) Concentrations of spheroidal carbonaceous particles (SCPs) in core SHLW21-Fr-1; (b–d) Concentrations of parent polycyclic aromatic hydrocarbons (parent-PAHs), high- (4–7 ring) and low-molecular weight (HMW- and LMW-) PAHs; (e) Ratio of HMW-/LMW-PAHs in core SHLW20-6; (f) Concentrations of soot in core SHLW21-Fr-1. The horizontal dashed line marks the varve deposited in 1952 CE. From figure 5 of Han et al. (2023).

g) Slightly increased heavy metal concentrations (core SHLW21-Fr-9): Pb, Cu, Zn and Cd show increasing trends starting at a depth of 90 mm (1950 CE; Figure SHL5). Further, more prominent increases in these elements occur above a depth of 53 mm (after 1982 CE) and the highest heavy metal concentrations were found in sediments deposited at 36 mm depth (early 2000s);

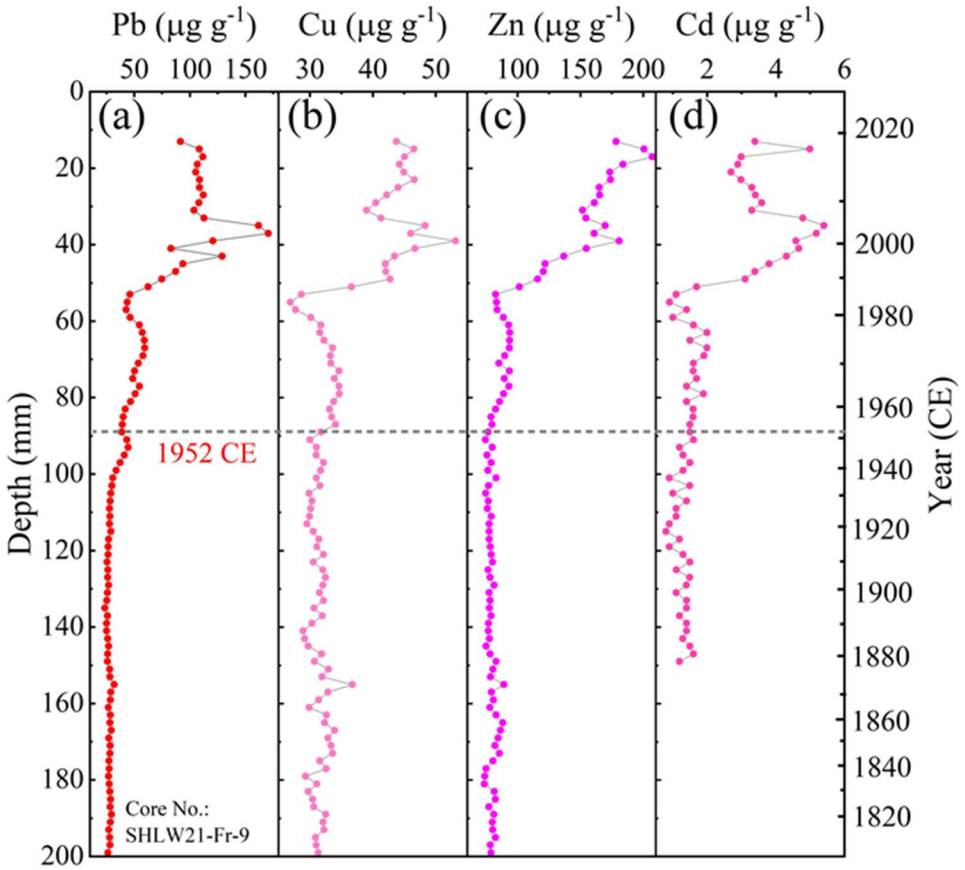

Figure SHL5. Depth distributions of heavy metals in sediment cores from Sihailongwan Maar Lake. (a–d) Pb, Cu, Zn and Cd concentrations in core SHLW21-Fr-9. The horizontal dashed line marks the varve deposited in 1952 CE. From figure 7 of Han et al. (2023).

h) Decrease in eDNA composition and Shannon index of phytoplankton (SHLW21-Fr-14): There is an overall decreasing trend in eDNA composition above 110 mm depth (since the 1920s) and further reductions above 90 mm depth (after 1950 CE; Figure SHL6). The Shannon index of phytoplankton, which can indicate biological diversity, also decreases rapidly above 90 mm depth (1950 CE).

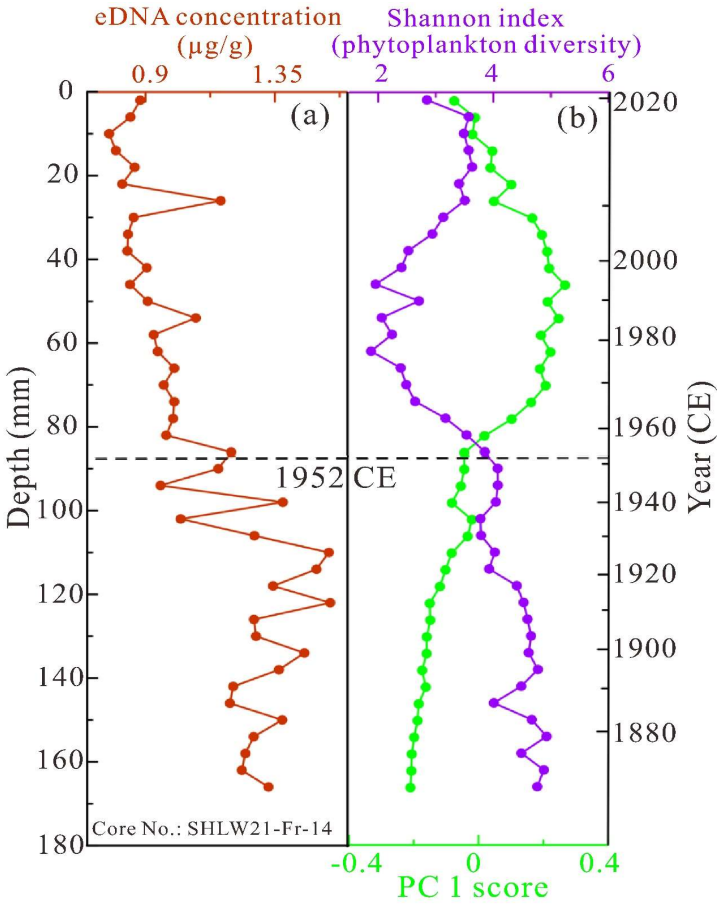

Figure SHL6. Vertical profiles of sedimentary DNA content and diversity and community structure changes in phytoplankton in core SHLW21-Fr-14 from Sihailongwan Maar Lake. (a) Environmental DNA concentrations; (b) Shannon index of the phytoplankton diversity (purple curve), and PC1 (green curve) extracted from the PCA (principal component analysis) based on the phytoplankton composition data. From figure 8 of Han et al. (2023).

3.3 Śnieżka Peatland, Poland

Project Leader and submission by Barbara Fiałkiewicz-Kozieł.

Details of the proposed SABS core and of the site are provided by Fiałkiewicz-Kozieł *et al*. (2023).

1. Location and geological setting

The Śnieżka Peatland is located in the Polish part of the Sudetes mountains, in the Karkonosze National Park (Figure SP1). The proposed SABS core (Sn0) was collected in the summer of 2020 at the study site (50.739139°N, 15.707786°E), located in peat developed on a plateau (1433 m asl) in the Karkonosze range, close to the highest summit, Mt. Śnieżka (1602 m asl). Additional cores Sn1 and Sn2 had been collected earlier from the same site (within 15 m) in spring 2012. The mountain range is a significant orographic barrier for regional-continental air masses. The dominant winds are westerlies (Sobik *et al*., 2014).

The present plant community of the peatland consists of*: Sphagnum lindbergii, Sphagnum balticum, Carex limosa*, *Carex rostrata*, *Baeothryon caespitosum*, *Eriophorum vaginatum*, *Carex limosa*, *Carex rostrata*, *Empetrum hermaphroditum*, *Andromeda polifolia*, *Oxycoccus palustris* and *Rubus chamaemorus* as well as dwarf *Pinus mugo,* indicating the ombrotrophic character of the peatland.

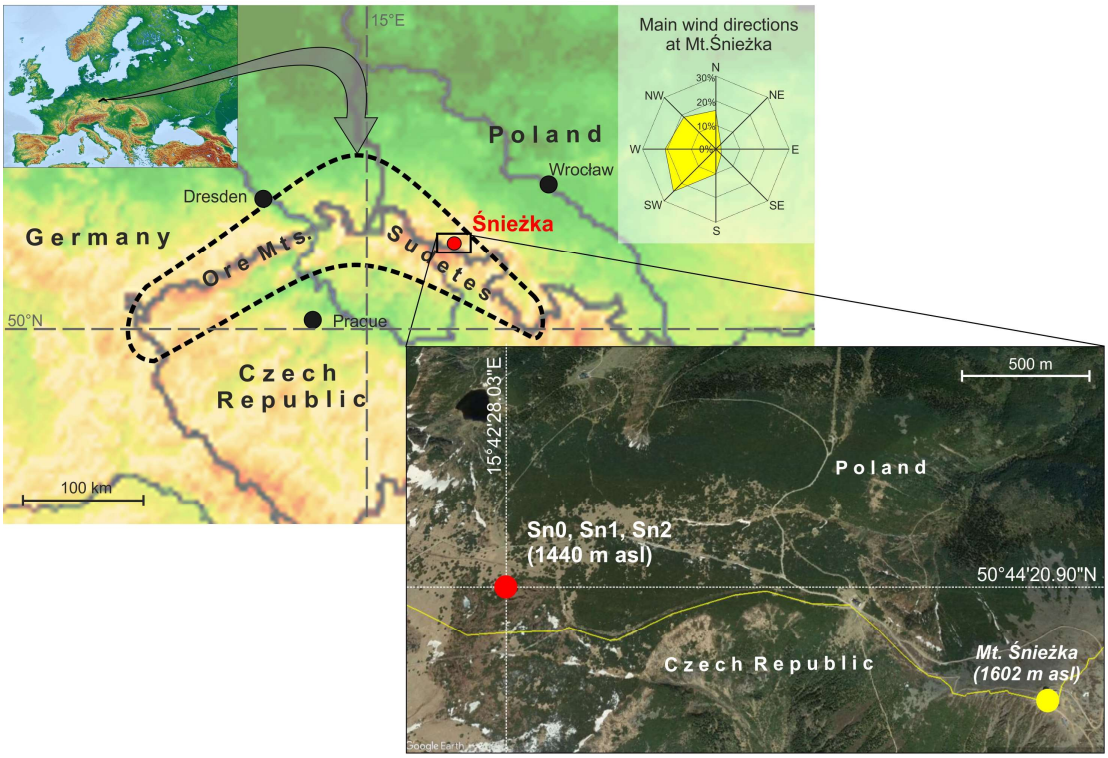

Figure SP1. Map of the study site. The wind rose is after Sobik et al. (2014). From Fiałkiewicz-Kozieł et al. (2023, fig. 1).

2. Lithology and indication in the field

The Śnieżka peat core provides a significant volume (10 × 10 × 50 cm) of deposited organic matter to support investigations (Figure SP2). The lower peat intervals (50–29 cm depth) are mainly composed of minerotrophic mosses such as *Sphagnum russowii* and *Straminergon stramineum* (ma1 in Figure SP2). The overlying peat (ma2 from 29–15 cm) lacks *S. stramineum* and only contains *Sphagnum angustifolium* in the basal part, whereas *Polytrichum strictum* becomes a significant peat-forming species. In the topmost part of Sn0 (ma3 from 15–0 cm) *Andromeda polifolia* becomes a significant component, whereas at the top of the biostratigraphic zone *P. strictum* becomes less abundant and Ericaceae rootlets are absent. Importantly, the inferred base of the proposed Crawfordian stage at 39.5 cm depth (1952 CE) does not coincide with a local macrofossil zone boundary.

The ash content (AC) in core Sn0 is low (up to 6%) and shows more complex patterns than the botanical layering of the peat. This core has two zones with a boundary at ~18 cm depth (Figure SP2). The lower zone has 2%–4% higher ash content values than the

upper one. The bulk density is low throughout (typically 0.02–0.06 g/cm), though of lower density in the upper 10 cm.

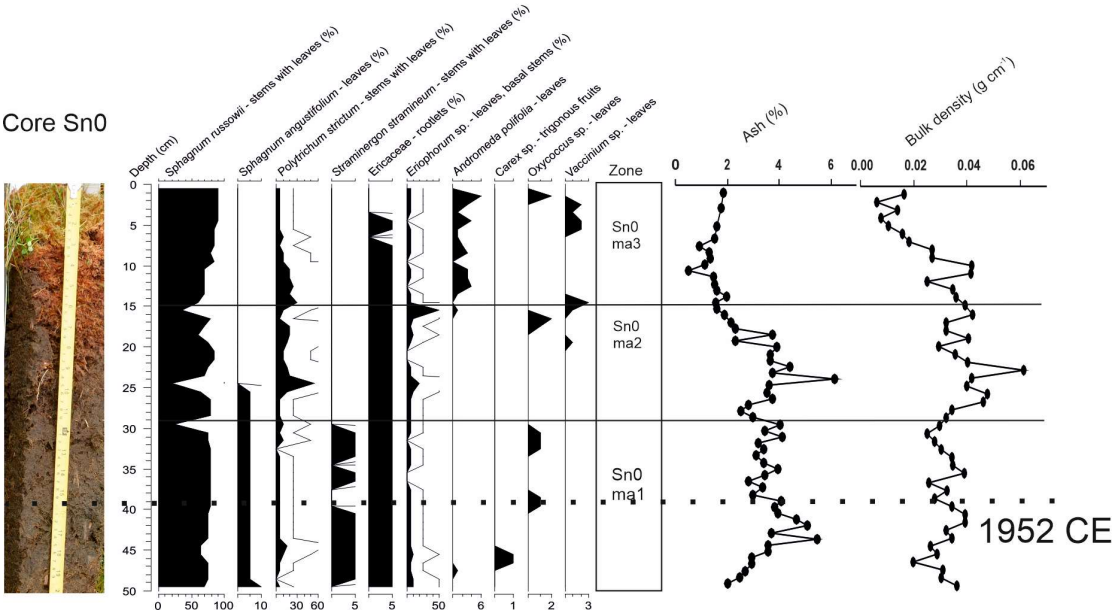

Figure SP2. Image of core Sn0 profile compared with macrofossil analysis used to assess the trophic state and pattern of peatland development; physical properties (ash % and bulk density) are used to confirm the trophic state and continuity of the peat profile. From Fiałkiewicz-Kozieł et al. (2023, fig. 2).

3. Accessibility

Core Sn0 was only partially subsampled, and a complete 5 cm × 5 cm × 50 cm part of the core (i.e., 25% of the original core) is retained as an archive in the cold room (4°C) of the Faculty of Geographical and Geological Sciences, Adam Mickiewicz University. The Śnieżka site is located in a protected area of the Karkonosze National Park, but is easily accessible for further studies. Access to the peatland is facilitated by proximity to tourist tracks. Permission to collect peat material is mandatory, and may be granted by the Ministry of Climate and Environments as well as by the National Park Administration.

4. Conservation

The proposed SABS peat profile is retained as an archive at Adam Mickiewicz University. The peatland is protected by national regulations. The Karkonosze National Park was created in 1959, with most of the park area, around 33.80 km^2, consisting of forests. In 1992 the Karkonosze National Park, together with the neighbouring Czech Krkonoše National Park, became part of the Krkonoše/Karkonosze Transboundary Biosphere Reserve under UNESCO's Man and the Biosphere Programme. Forty hectares of peat bogs in the reserve are designated a Ramsar international wetland site. The site was studied via extraction of cores for site protection reasons as this is a less disturbing sampling methodology than through a dug section.

5. Stratigraphic completeness of the section

The Sn0 peat profile provides a continuous geological record for the last ~200 years (i.e., no hiatuses, gaps and other disturbances were identified), verified based on physical properties of the peat core, macrofossils (Figure SP2) and age-depth model (see below). Macrofossils indicate typical development of peatland towards ombrotrophic status, while physical properties – ash content and bulk density – revealed typical natural values, with the exception of ash content which increased slightly at 24.5 cm depth as a result of fly ash deposition. The profile is characterised by a relatively high peat accumulation rate (0.66 cm/yr on average) which provides a high-resolution geological record (around 2 years per 1 cm) across the boundary between the Holocene and Anthropocene series.

6. *Age constraints*

Despite an absence of annual layering, the proposed SABS core (Sn0) has a well-constrained chronology. Repetition of certain analyses (especially the plutonium signal) for the two investigated cores Sn1 (2012) and Sn0 (2020), both show consistent profiles, providing confidence that future profiles will duplicate the results seen in the proposed SABS core.

The chronological control of core Sn0 is based on dates provided by activity concentration of ^{210}Pb and fraction modern ^{14}C ($F^{14}C$) and validated with activity concentrations of ^{137}Cs results. The supported level of $^{210}Pb_{sup}$ was obtained as the mean value (±SD, 1σ) of activities for the lowermost layers, where the level of $^{210}Pb_{tot}$ has reached a steady state. By subtracting $^{210}Pb_{sup}$ activity from $^{210}Pb_{tot}$ activity on a level-by-level basis, the unsupported fraction ($^{210}Pb_{uns}$) was calculated and used in the dating model. The Constant Flux Constant Sedimentation model (CF/CS; Sanchez-Cabeza and Ruiz-Fernández, 2012) was applied allowing calculations of the peat ages at different depth intervals. Annual accumulation rates (SAR, g/cm^2 /yr) were calculated from peat bulk density and the thickness of individual slices.

Results of ^{14}C in core Sn0 samples are expressed as $F^{14}C$ (fraction modern ^{14}C) and calibrated using the Bayesian sequence model of the OxCal calibration program (Bronk Ramsey, 2009) with the bomb peak atmospheric data for the Northern Hemisphere (Hua *et al*., 2021). Except for one sample with ^{210}Pb modelled age of 1941 ± 7 CE, all the samples follow the atmospheric NH bomb peak data (Figure SP3a). The high value of $F^{14}C$ measured for 1941 ± 7 CE was not included in the OxCal model. Based on the CF/CS model applied to ^{210}Pb activities the bottom of Sn0 (50 cm) was dated to 1931 ± 8 CE. Thus, the core encompassed 90 ± 8 years. The linear accumulation rates in cores Sn0 and Sn1 were 0.65 ± 0.11 cm/yr.

Three ^{137}Cs maxima were observed (Figures SP3b; 4). The uppermost was located just below the 2020 peat surface. The second and largest activity peak occurred between 20 and 18 cm and can be related to the Chernobyl event (1986) (^{210}Pb model age 1992 ± 2 CE). The lowest and smallest Cs peak, at 29–27 cm, was assigned to the bomb-peak for above-ground nuclear weapon tests (1963 CE), which was corroborated by the nearby position of Pu maximum at 30.5 cm depth. The cause of the discrepancy between the ^{137}Cs record when compared with ^{14}C and $^{239+240}$Pu is the partial upward mobility of caesium in organic environments.

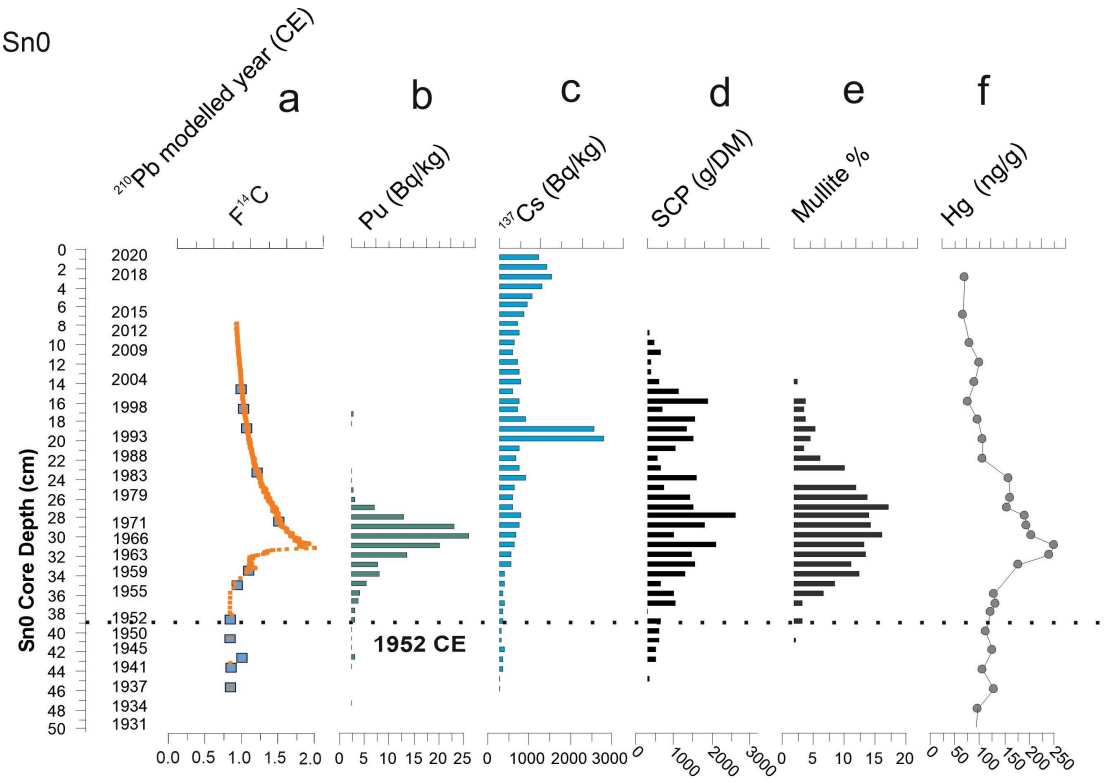

Figure SP3. Summary of the most important Anthropocene markers in core Sn0. The horizontal dashed line is referred to the proposed base of the Anthropocene (1952 CE). (a) ^{14}C in core Sn0 samples expressed as F^{14}C (fraction modern ^{14}C) and compared with the bomb peak atmospheric data for the Northern Hemisphere (Hua et al., 2021); (b) plutonium activity; (c) caesium activity; (d) concentrations of spheroidal carbonaceous particles; (e) mullite content; and (f) concentration of mercury. From Fiałkiewicz-Kozieł et al. (2023, fig. 7).

7. Proxies that allow correlation with the base of the proposed Crawfordian stage GSSP

The proposed basal interval of the Crawfordian stage evident in core Sn0 for this SABS proposal is marked by the following:

a) The base of the plutonium bomb-spike: The 1952 upturn in Pu activity is observed at 39.5 cm depth (^{210}Pb model age 1949 ± 6 CE) for Sn0 and is taken to equate with the base of the Crawfordian stage. The maximum peak, which correlates with the 1963 nuclear weapon tests, appears at 30–31 cm depth. The shift in the levels of the F^{14}C for Sn0 (Figure SP3a) compared with the atmospheric curve NH1 (Hua *et al.*, 2021) reveals a similarity to the Pu curve plotted vs. the ^{210}Pb model, confirming the robustness of the modelling used.

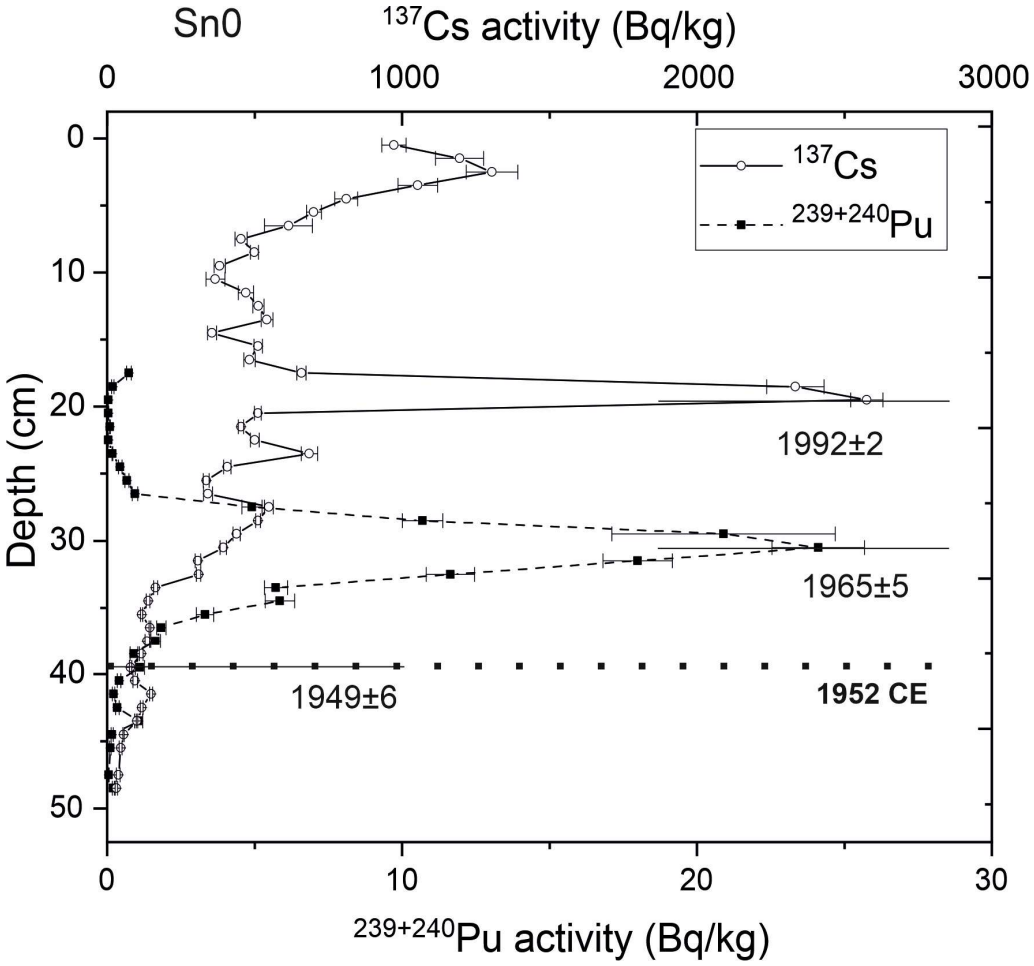

Figure SP4. Comparison of $^{239+240}$Pu and ^{137}Cs versus CF/CS modelled dates in the Sn0 core. From Fiałkiewicz-Kozieł et al. (2023, fig. 3).

b) Fly ash particles: High-temperature fossil fuel combustion produced spheroidal carbonaceous particles (SCPs) while spheroidal aluminosilicates (SAPs) are produced by coal burning. Both are easily detected in peat profiles. In Sn0, the first appearances of SCPs and SAPs are at 44–45cm (~1939 ± 7 CE) (Figure SP3d). However, a significant upturn is visible in the 1950s, following the first appearance of the primary Pu marker. Mullite, which is a crystalline phase of the technogenic mineral fraction, first appears close to the first global fallout of Pu, at the depth of 40.5 cm (Figure SP3e).

c) Inorganic geochemistry. Despite the long-term history of mining and processing precious ores, the most pronounced upturn in heavy metals released by industrial activity in Sn0 is represented by Hg, which has elevated concentrations from ~1960–1980 CE (Figure SP3f).

Additional proxies from core Sn1, located adjacent to core Sn0:

d) Trace metals: There are significant upturns in Al, Zn and Pb in the 1950s peat interval (Figure SP5b, c, d). While peats in different countries may show varying dates for the onset of trace metal contamination and for peak metal concentrations making them unsuitable as a global synchronous marker, the rise in trace metal inputs for Pb and Zn in the 1950s does appear to be globally synchronous for all

peat deposits studied. This increase in almost all trace elements and rare earth elements (REE) investigated is visible in the Śnieżka Peatland (Figure SP5) and here may be attributed to lignite combustion in 'Black Triangle' countries.

e) Biostratigraphy: Globalisation phenomena and climate change have altered the distribution of non-native species, which have become invasive in new environments. In Europe, one of the best-known alien plants is *Ambrosia artemisiifolia* (common ragweed) which has expanded over Europe, especially rapidly and widely since 1940 CE due to its contamination within crop seeds and transboundary transport. Because the Śnieżka peatland is located above the main track of pollen dispersal, in core Sn1 *A. artemisiifolia* first appeared in 1956 ± 3 CE (Figure SP5e). The signal of hydroclimatic impact induced by global warming, strengthened by pollution and dust deposition, is indicated in core Sn1 by the absence of sensitive testate amoebae mixotrophs (*Archerella flavum*) above 36.5 cm (1959 ± 3 CE) (Figure SP5g).

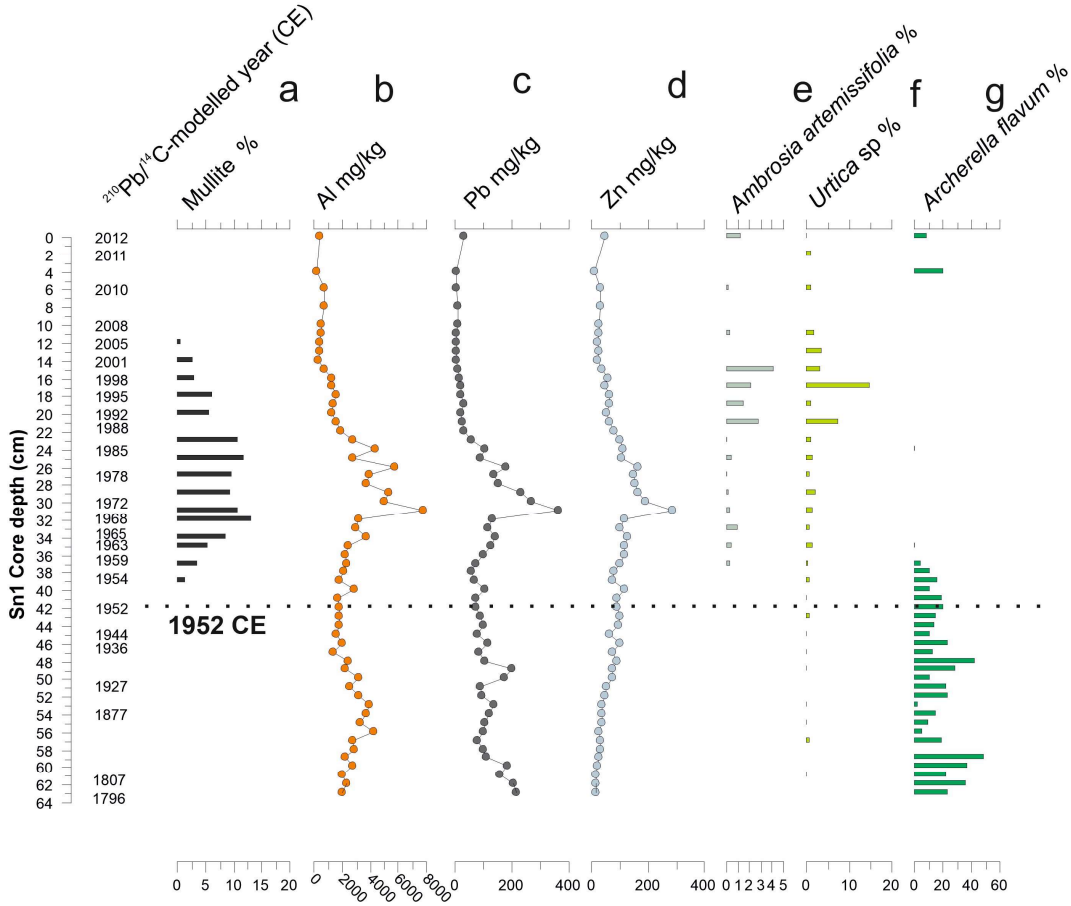

Figure SP5. Summary of additional Anthropocene markers investigated from peat profile Sn1, adjacent to the proposed SABS core. The horizontal dotted line correlates with the base of the proposed Crawfordian stage (1952 CE). (a) Mullite content; (b, c, d) associated industrial activity geochemical elements concentration for Al, Pb and Zn; (e) Ambrosia artemisiifolia *as an example of a non-native (for Europe) invasive plant pollen profile; (f) the increase in* Urtica *pollen percentages linked to further nitrification of peatland from the input of industrial dust; (g)* Archerella flavum *profile as an example of a testate amoebae mixotroph, which disappeared in the late 1950s. From Fiałkiewicz-Kozieł et al. (2023, fig. 7).*

4. SUMMARY

The AWG has developed a proposal for the formal definition of an Anthropocene epoch/series, and its associated Crawfordian age/stage commencing in the mid-20th century (specifically the year 1952 CE). The proposal recommends that the Anthropocene be constrained by a Global boundary Stratotype Section and Point (GSSP) in the sediment core CRA23-BC-1F-B from Crawford Lake, Ontario, Canada at the contact between the thin (0.33 mm) pale calcite lamina and overlying dark organic lamina, both assigned a varve age 1952 CE, with the contact specifically marking *the fall of 1952 CE.* This lithological boundary is at a depth of 17.5 cm and occurs at the base of the primary marker, the first main upturn in $^{239+240}$Pu activity in the core. The GSSP proposal is supported by three Standard Auxiliary Boundary Stratotypes (SABSs) in cores from Beppu Bay (Japan), Sihailongwan Maar Lake (China), and Śnieżka Peatland (Poland), and eight reference sections that permit correlation of the base of the Anthropocene into many of the diverse depositional environments in which it is clearly recorded (see Appendix 2). Global correlation is achieved using the many geosignatures of the Great Acceleration Event Array (GAEA: Waters *et al*., 2022; Head *et al*., 2023a, b). In the analysis of 12 candidate sites and other reference sections for potential formalisation of the Anthropocene (Waters *et al*., 2023, Table 2, Figure 2), more than one hundred separate proxy signals were used to characterise the stratigraphy at decadal to annual, in some cases sub-annual, level. Many of the signals are entirely new within Earth history, reflecting a proliferation of new forms of stratigraphic evidence associated with the Anthropocene. These include several artificial radionuclides, microplastics, industrial fly ash, various kinds of synthetic persistent organic compounds and novel biostratigraphic signals, notably the rapid and near-global spread of introduced species.

Table 2 [overpage]. Timing of important markers across the 12 candidate sites. Colour for sites reflects environment of formation, as shown in Figure 1. The following abbreviations are used: SCPs: spheroidal carbonaceous particles; PAHs: polycyclic aromatic hydrocarbons; PCBs: polychlorinated biphenyls; DDT: dichlorodiphenyltrichloroethane. Key: Green boxes show analysis has been undertaken – timing of event onset; Nil – no useful variation; none – not detected; × – unsuitable. Nature of signal change; (↑) rapid upturn, (↓) rapid downturn, others written in full. Modified from Waters et al. (2023, table 3).

GSSP Sites and Analyses (direction of change)	Gotland Basin, Baltic Sea	San Francisco Estuary, USA	Beppu Bay, Japan	Searsville Lake, USA	Crawford Lake, Canada	Sihailongwan Maar Lake, China	Flinders Reef, Australia	Gulf of Mexico, USA	Antarctic Peninsula Ice Core	Ernesto Cave Spleothem, Italy	Śnieżka peatland, Poland	Anthropo-genic deposits, Vienna
Lithological change	1956±4	~1952	1953	Nil	1950	1955-56	Nil	Nil	Nil	1840±12		
^{210}Pb dating	x	x	√	x	√	√	x	x			√	
^{241}Am, ^{137}Cs	1953±4 (onset)	1980s (^{137}Cs onset)	1956 (↑)	1958 (onset)	1955 (↑)	1953 (↑)	x	None			1957 (↑)	1945 (onset)
Pu isotopes	1953±4 (onset)	1983 (↑)	1954 (↑)	1946-7 (onset) 1952 (↑)	1952 (↑)	1953 (↑)	1960 (peak)	1956 (↑)	1945 (onset)		1952 (↑)	1945 (onset)
^{14}C (+ A bomb)	1956±4 (↑)	x	1963 (↑)	x	Mid-1950s (↑)	1953 (↑)	1958 (↑)	1957 (↑)		1960±3 (↑)	1951±6 (↑)	
Pb isotopes	1947±4 (↓)		1959 (peak)	Nil							~1961 (↓)	
Total C & N	1956±4 (↑)	1978 (↑)	1977 (peak)	~1929 (↑)	1954-64 (peak)	Nil	1960 (N, ↑)				Nil	
C stable isotopes	1952±4 (↑)	nil	1953 (low)	~1929 (↓)	1932 (peak)	1950 (↓)	1970 (↓)	1956 (↓)		1841±10 (↑)	1940s-70s (↓)	
N stable isotopes	1956±4 (plateau)	1952 (↑)	1953 (onset)	Nil	1971 (low)	~1980 (↓)	1955 (plateau)	1963 (↑)			1940s-70s (↓)	
Fly ash (SCP/SAP)	1953±4 (↑)	1967 (onset)	1964 (↑)	~1934 (onset)	1953 (↑)	1950 (↑)	None	None	1936 (onset)		1959±6 (SCP ↑) 1947±7 (mullite, onset)	
Trace elements (and/or Hg)	1947±4 (↑)	Early 1960s (↑)	1953 (↑)	~1965 (Hg ↑)	1950 (Pb); 1952 (Zn) (↑)	~1950 (↑)	1929 (peak)	1975 (peak)		~1902 (↑)	1952 (1939±7) (↑)	1867-1899 (peak)
Plastics	1960 (↑)		1954 (onset)									1945 (onset)
PAH	1863±10 (↑)		1953 (↑)			1952 (↑)						
PCB			1953 (onset)	Above 1962 (↑)								

DDT	1950±4 (onset)		1953 (onset)									
Black Carbon/ microcharcoal			617 BCE (↑)			1978-9 (low)					1936±5 (↑)	
Oxygen Isotopes							~1950 (↑)	1933 (↑)	Nil	Nil		
CH_4 / S, SO_4^2			1963 (S↑)						~1958 ±5 (↑)	1960±3 (↑)		
Trace (Sr/Ca)							~1950 (peak)	1922 (↓)				
Molluscs (neobiota)		1986 (onset)										
Foraminifera (neobiota)		1983 (onset)	1941 (low)									
Ostracods (neobiota)		1975 (onset)		1952								
Pollen		Nil	1751	~1947	Mid-1950s (*Ulmus* ↓)						1956±3	
Diatoms (variable)			1970 (↑)	None	1952							
Dinoflagellates			1953 (onset)									
Pigments/ Biomarkers	1956±4 (↑)		1950 (onset)		~1800 (↑)	~1950 (↓)						
Testate amoebae (variable)			1970								1959±3	

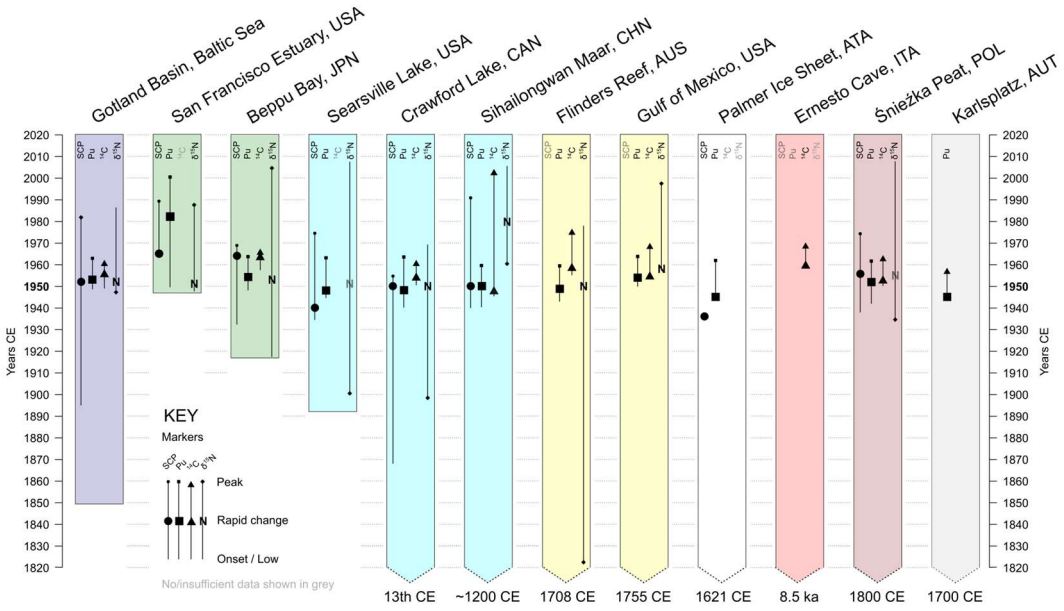

Figure 2. Correlation of significant shifts in or appearances of markers between the 12 candidate sites. Colour of cores reflects environment of formation, as shown in Figure 1 and Table 2. SCP: spheroidal carbonaceous particle; Pu: plutonium; ^{14}C: radiocarbon; $\delta^{15}N$: stable nitrogen isotopes. Reproduced from Waters et al. (2023, figure 2).

REFERENCES (*AWG publications written in full, including defining papers for 12 sites and thematic sets)

*AWG, 2019. Announcement by the Anthropocene Working Group. Available at: http://quaternary.stratigraphy.org/working-groups/anthropocene/ *[Accessed June 16, 2022]*.

*Borsato, A., Fairchild, I.J., Frisia, S., Wynn, P.M., Fohlmeister, J., 2023. The Ernesto Cave, northern Italy, as a candidate auxiliary reference section for the definition of the Anthropocene series. *The Anthropocene Review* **10**(1): 269–287. https://doi.org/10.1177/20530196221144094

Crutzen, P.J., Stoermer, E.F., 2000. The "Anthropocene." *IGBP Global Change Newsletter* **41**: 17–18.

*DeLong, K.L., Palmer, K., Wagner, A.J., Weerabaddana, M.M., Slowey, N., Herrmann, A.D., Duprey, N., Martínez-García, A., Jung, J., Hajdas, I., Rose, N.L., Roberts, S.L., Roberts, L.R., Cundy, A.B., Gaca, P., Milton, J.A., Yang, H., Turner, S.D., Huang, C.-Y., Shen, C.-C., Zinke, J., 2023. The Flower Garden Banks *Siderastrea siderea* coral as a candidate Global boundary Stratotype Section and Point for the Anthropocene series. *The Anthropocene Review* **10**(1): 225–250. https://doi.org/10.1177/20530196221147616

*Fiałkiewicz-Kozieł, B., Łokas, E., Smieja-Król, B., Turner, S., De Vleeschouwer, F., Woszczyk, M., Marcisz, K., Gałka, M., Lamentowicz, M., Kołaczek, P., Hajdas, I., Karpińska-Kołaczek, M., Kołtonik, K., Mróz, T., Roberts, S., Rose, N., Krzykawski, T., Boom, A., Yang, H., 2023. The Śnieżka peatland as a candidate Global boundary

Stratotype Section and Point for the Anthropocene series. *The Anthropocene Review* **10**(1): 288–315. https://doi.org/10.1177/20530196221136425

*Han, Y., Zhisheng, A., Lei, D., Zhou, W., Zhang, L. Zhao, X., Yan, D., Arimoto, R., Rose, N.L., Roberts, S.L., Li, L., Tang, Y., Liu, X., Fu, X., Schneider, T., Hou, X., Lan, J., Tan, L., Liu, X., Hu, J., Cao, Y., Liu, W., Wu, F., Wang, T., Qiang, X., Chen, N., Cheng, P., Hao, Y., Wang, Q., Chu, G., Guo, M., Han, M., Tan, Z., Wei, C., Dusek, U., 2023. The Sihailongwan Maar Lake, northeastern China as a candidate Global boundary Stratotype Section and Point for the Anthropocene series. *The Anthropocene Review* **10**(1): 177–200. https://doi.org/10.1177/20530196231167019

Hancock, G.J., Tims, S.G., Fifield, L.K., Webster, I.T., 2014. The release and persistence of radioactive anthropogenic nuclides. In: Waters, C.N., Zalasiewicz, J., Williams, M. et al. (Eds.) *A Stratigraphical Basis for the Anthropocene*. Geological Society, London, Special Publications **395**, pp. 265–281. https://doi.org/10.1144/SP395.15

Head, M.J., Gibbard, P.L., 2015. Formal subdivision of the Quaternary System/Period: Past, present, and future. *Quaternary International* **383**: 4–35. https://doi.org/10.1016/j.quaint.2015.06.039

*Head, M.J., Waters, C.N., Zalasiewicz, J.A., Barnosky, A.D., Turner, S.D., Cearreta, A., Leinfelder, R., McCarthy, F.M.G., Richter, D. de B., Rose, N.L., Saito, Y., Vidas, D., Wagreich, M., Han, Y., Summerhayes, C.P., Williams, M., Zinke, J., 2023a. The Anthropocene as an epoch is distinct from all other concepts known by this term. *Journal of Quaternary Science*. https://doi.org/10.1002/jqs.3513

*Head, M.J., Zalasiewicz, J.A., Waters, C.N., Turner, S.D., Williams, M., Barnosky, A.D., Steffen, W., Wagreich, M., Haff, P.K., Syvitski, J., Leinfelder, R., McCarthy, F.M.G., Rose, N.L., Wing, Scott, L., An, Z., Cearreta, A., Cundy, A.B., Fairchild, I.J., Han, Y., Ivar do Sul, J.A., Jeandel, C., McNeill, J.R., Summerhayes, C.P., 2023b. The Anthropocene is a prospective epoch/series, not a geological event. *Episodes* **46**(2): 229–238. https://doi.org/10.18814/epiiugs/2022/022025

Head, M.J., Aubry, M.-P., Piller, W.E., Walker, M., 2023c. The Standard Auxiliary Boundary Stratotype: a replacement for the Auxiliary Stratotype Point in supporting a Global boundary Stratotype Section and Point (GSSP). *Episodes* **46**(1): 35-45. https://doi.org/10.18814/epiiugs/2022/022012

Head, M.J., Aubry, M.-P., Piller, W.E., Walker, M., 2023d. Standard Auxiliary Boundary Stratotype (SABS) approved to support the Global boundary Stratotype Section and Point (GSSP). *Episodes* **46**(1): 99-100. https://doi.org/10.18814/epiiugs/2022/022044

*Himson, S., Williams, M., Zalasiewicz, J., Waters, C., McGann, M., England, R., Boom, A., Holmes, R., Sampson, S., Pye, C., Berrio, J.C., Tyrrell, G., Wilkinson, I.P., Rose, N., Cundy, A., 2023. The San Francisco Estuary, USA as a reference section for the Anthropocene series. *The Anthropocene Review* **10**(1): 87–115. https://doi.org/10.1177/20530196221147607

Hinata, H., Kuwae, M., Tsugeki, N. *et al*., 2023. A 75-year history of microplastic fragment accumulation rates in a semi-enclosed hypoxic basin. *Science of the Total Environment* **854**: 158751. https://doi.org/10.1016/j.scitotenv.2022.158751

Hua, Q., Turnbull, J.C., Santos, G.M. *et al*., 2021. Atmospheric Radiocarbon for the Period 1950–2019. *Radiocarbon* **64**: 723-745. https://doi.org/10.1017/rdc.2021.95

Inoue, J., Takenaka, N., Okudaira, T., Kuwae, M., 2022. The record of sedimentary spheroidal carbonaceous particles (SCPs) in Beppu Bay, southern Japan, compared to historical trends of industrial activity and atmospheric pollution: Further evidence for SCPs as a marker for Anthropocene industrialization. *The Anthropocene Review* **10**(2), https://doi.org/10.1177/20530196221076577

*Kaiser, J., Abel, S., Arz, H.W. Cundy, A.B., Dellwig, O., Gaca, P., Gerdts, G., Hajdas, I., Labrenz, M., Milton, J.A., Moros, M., Primpke, S., Roberts, S.L., Rose, N.L., Turner, S.D., Voss, M., Ivar do Sul., J.A., 2023. The East Gotland Basin (Baltic Sea) as a candidate Global boundary Stratotype Section and Point for the Anthropocene series. *The Anthropocene Review* **10**(1): 25–48. https://doi.org/10.1177/20530196221132709

Kuwae, M., Tsugeki, N.K., Amano, A., *et al*., 2022. Human-induced marine degradation in anoxic coastal sediments of Beppu Bay, Japan, as an Anthropocene marker in East Asia. *Anthropocene* **37**: 100318. https://doi.org/10.1016/j.ancene.2021.100318

*Kuwae, M., Finney, B.P., Shi, Z., Sakaguchi, A., Tsugeki, N., Omori, T., Agusa, T., Suzuki, Y., Yokoyama, Y., Hinata, H., Hatada, Y., Inoue, J., Matsuoka, K., Shimada, M., Takahara, H., Takahashi, S., Ueno, D., Amano, A., Tsutsumi, J., Yamamoto, M., Takemura, K., Yamada, K., Ikehara, K., Haraguchi, T., Tims S., Froehlich, M., Fifield, L.K., Aze, T., Sasa, K., Takahashi, T., Matsumura, M., Tani, Y., Leavitt, P.R., Doi, H., Irino, T., Moriya, K., Hayashida, A., Hirose, K., Suzuki, H., Saito, Y., 2023. Beppu Bay, Japan, as a candidate Global boundary Stratotype Section and Point for the Anthropocene series. *The Anthropocene Review* **10**(1): 49–86. https://doi.org/10.1177/20530196221135077

Llew-Williams, B.M., McCarthy, F.M.G., Krueger, A.M. *et al*., 2024. Varve formation in meromictic Crawford Lake, Ontario, Canada: important process for characterizing the Anthropocene epoch. Accepted for publication in *Journal of Paleolimnology,* 71: 101–124.

Matsuoka, K., Kojima, N., Kuwae, M., 2022. Marine environmental change induced by anthropogenic activities – from a viewpoint of aquatic palynomorph assemblages preserved in sediment cores of Beppu Bay, west Japan. *Frontiers in Marine Science* **9**. https://doi.org/10.3389/fmars.2022.843824

*McCarthy, F.M.G., Patterson, R.T., Head, M.J., Riddick, N.L., Cumming, B.F., Hamilton, P.B., Pisaric, M.F.J., Gushulak, A.C., Leavitt, P.R., Lafond, K.M., Llew-Williams, B., Marshall, M., Heyde, A., Pilkington, P.M., Moraal, J., Boyce, J.I., Nasser, N.A., Walsh, C., Garvie, M., Roberts, S., Rose, N.L., Cundy, A.B., Gaca, P., Milton, A., Hajdas, I., Crann, C.A., Boom, A., Finkelstein, S.A., McAndrews, J.H. *et al*., 2023. The varved succession of Crawford Lake, Milton, Ontario, Canada as a candidate Global boundary Stratotype Section and Point for the Anthropocene series. *The Anthropocene Review* **10**(1), 146–176. https://doi.org/10.1177/20530196221149281

*McCarthy, F.M.G., Patterson, R.T., Walsh, C., Lafond, K.M., Cumming, B.F., Cundy, A.B., Hain, K., Gaca, P., Steier, P., Boom, A., Hamilton, P.B., Pisaric, M.F.J., Head, M.J., Boyce, J.I., Rose, N.L., Turner, S.D. 2024. High-resolution analysis of the varved succession at Crawford Lake across the base of the proposed Crawfordian Stage and Anthropocene Series. *The Anthropocene Review,* accepted subject to revision.

Nishimuta, K., Ueno, D., Takahashi, S. *et al*., 2020. Use of comprehensive target analysis for determination of contaminants of emerging concern in a sediment core collected from Beppu Bay, Japan. *Environmental Pollution* **272:** 115587. https://doi.org/10.1016/j.envpol.2020.115587

*Rosol, C., Schäfer, G.N., Turner, S.D., Waters, C.N., Head, M.J., Zalasiewicz, J., Rossée, C., Renn, J., Klingan, K., Scherer, B.M., 2023. Evidence and experiment: Curating contexts of Anthropocene geology. *The Anthropocene Review* **10**(1): 330–339. https://doi.org/10.1177/20530196231165621

Sanchez-Cabeza, J.-A. Ruiz-Fernández, A.C., 2012. ^{210}Pb sediment radiochronology: An integrated formulation and classification of dating models. *Geochimica et Cosmochimica Acta* **82**:183–200. https://doi.org/10.1016/j.gca.2010.12.024

Scholz, D., Frisia, S., Borsato, A. *et al*., 2012. Holocene climate variability in north-eastern Italy: potential influence of the NAO and solar activity recorded by speleothem data. *Climate of the Past* **8**: 1367–1383. https://doi.org/10.5194/cp-8-1367-2012

Sobik, M., Błaś, M., Migała, M. *et al*., 2014. Klimat. In: Knapik R and Raj A (eds) *Przyroda Karkonoskiego Parku Narodowego* [Karkonoski Park Narodowy]. Jelenia Gora, Bielsko-Biała: DIMOGRAF, pp.147–186.

*Stegner, M.A., Hadly, E.A., Barnosky, A.D., La Selle, S., Sherrod, B., Anderson, R.S., Redondo, S.A., Viteri, M.C., Weaver, K.L., Cundy, A.B., Gaca, P., Rose, N.L., Yang, H., Roberts, S.L., Hajdas, I., Black, B.A., Spanbauer, T.L., 2023. The Searsville Lake Site (California, USA) as a candidate Global boundary Stratotype Section and Point for the Anthropocene series. *The Anthropocene Review* **10**(1): 116–145. https://doi.org/10.1177/20530196221144098

Takahashi, H., Sakaguchi, A., Hain, K., *et al*., 2023. Reconstructing the chronology of the natural and anthropogenic uranium isotopic signals in a marine sediment core from Beppu Bay, Japan. *Heliyon* **9**: e14153. https://doi.org/10.1016/j.heliyon.2023.e14153

Takahashi, S., Anh, H.Q., Watanabe, I. *et al*., 2020. Characterization of mono- to deca-chlorinated biphenyls in a well-preserved sediment core from Beppu Bay, Southwestern Japan: Historical profiles, emission sources, and inventory. *Science of the Total Environment* **743**: 140767. https://doi.org/10.1016/j.scitotenv.2020.140767

*Thomas, E.R., Vladimirova, D.O., Tetzner, D.R., Emanuelsson, D.B., Humby, J., Turner, S.D., Rose, N.L., Roberts, S.L., Gaca, P., Cundy, A.B., 2023a. The Palmer ice core as a candidate Global boundary Stratotype Section and Point for the Anthropocene series. *The Anthropocene Review* **10**(1): 251–268. https://doi.org/10.1177/20530196231155191

Thomas, E.R., Tetzner, D.R., Roberts, S.L., Turner, S.D., Rose, N.L., 2023b. First evidence of industrial fly-ash in an Antarctic ice core. *Scientific Reports* **13**: 6529. https://doi.org/10.1038/s41598-023-33849-x

UNSCEAR (United Nations Scientific Committee on the Effects of Atomic Radiation) 2000. *Sources and Effects of Ionizing Radiation*, 2000 Report, Vol. 1. New York: United Nations. https://www.unscear.org/unscear/en/publications/2000_1.html

*Wagreich, M., Meszar, M., Lappé, K., Wolf, J., Mosser, M., Hornek, K., Koukal, V., Litschauer, C., Piperakis, N., Hain, K., 2023. The urban sediments of Karlsplatz,

Vienna (Austria) as a reference section for the Anthropocene series. *The Anthropocene Review* **10**(1): 316–329. https://doi.org/10.1177/20530196221136427

*Waters, C.N., Turner, S.D., 2022. Defining the onset of the Anthropocene. *Science* **378** (6621): 706–708. https://doi.org/10.1126/science.ade2310

*Waters, C.N., Williams, M., Zalasiewicz, J., Turner, S.D., Barnosky, A.D., Head, M.J., Wing, S.L., Wagreich, M., Steffen, W., Summerhayes, C.P., Cundy, A.B., Zinke, J., Fiałkiewicz-Kozieł, B., Leinfelder, R., Haff, P.K., McNeill, J.R., Rose, N.L., Hajdas, I., McCarthy, F.M.G., Cearreta, A., Gałuszka, A., Syvitski, J., Han, Y., An, Z., Fairchild, I.J., Ivar do Sul, J.A., Jeandel, C., 2022. Epochs, events and episodes: Marking the geological impact of humans. *Earth-Science Reviews* **234**: 104171. https://doi.org/10.1016/j.earscirev.2022.104171

*Waters, C.N., Turner, S.D., Zalasiewicz, J., Head, M.J. (Eds.), 2023. Candidate sites and other reference sections for the Global boundary Stratotype Section and Point of the Anthropocene series. *The Anthropocene Review* **10**(1): 3–24. https://doi.org/10.1177/20530196221136422

Yokoyama, Y., Tims, S., Froehlich, M. *et al*., 2022. Plutonium isotopes in the North Western Pacific sediments coupled with radiocarbon in corals recording precise timing of the Anthropocene. *Scientific Reports* **12**: 10068. https://doi.org/10.1038/s41598-022-14179-w

*Zinke, J., Cantin, N.E., DeLong, K.L., Palmer, K., Boom, A., Hajdas, I., Duprey, N., Martínez-García, A., Rose, N.L., Roberts, S.L., Yang, H., Roberts, L.R., Cundy, A.B., Gaca, P., Milton, J.A., Frank, G., Cox, A., Sampson, S., Tyrrell, G., Agg, M., Turner, S.D., 2023. North Flinders Reef (Coral Sea, Australia) *Porites* sp. corals as a candidate Global boundary Stratotype Section and Point for the Anthropocene series. *The Anthropocene Review* **10**(1): 201–224. https://doi.org/10.1177/20530196221142963

Appendices for Part 2: Descriptions of the proposed Crawford Lake GSSP and supporting SABSs

APPENDIX 1: REQUIREMENTS FOR A GSSP/SABS

Table 1. Requirements for a GSSP based on Remane et al. (1996) and Head & Gibbard (2015), with comments relevant to the Anthropocene as an epoch/series and on suitability of specific sites (from Waters et al., 2023).

Requirement	Explanation	Relevance for Anthropocene	Potential problem sites
Best possible record of the relevant marker events	Especially important for the primary event, but also any relevant secondary markers, for maximum correlation potential.	Requires environments that record the primary marker and ideally multiple secondary markers.	Ernesto Cave (absence of Pu primary marker)
Adequate thickness	Exposure over sufficient thickness to allow secondary markers to be recognized in relation to the boundary.	Needs sufficient thickness below and above the boundary to adequately show distinction between Holocene and Anthropocene strata; this can be achieved in thin, highly resolved successions.	San Francisco Estuary (insufficient Holocene interval in core)
Continuous sedimentation	There should be no gaps, condensation, or mass flows, close to the boundary.	Avoid evidence of erosional surfaces, scours or palaeosols; problematic for most anthropogenic deposits.	Karlsplatz
High sedimentation rates	The rate of sedimentation should be sufficiently high to separate successive, including near-contemporaneous, events.	This discounts modern abyssal marine sediments.	No sites
Absence of disturbance	Absence of synsedimentary or tectonic disturbance so as to facilitate unambiguous interpretation of the sedimentary sequence both vertically and laterally.	Bioturbation and anthroturbation can be problematic in many marine and lacustrine settings, though inhospitable bottom waters can limit disturbance; earthquakes can fluidise sediments.	Beppu Bay (turbidites/ earthquakes); San Francisco Estuary (bioturbation); Karlsplatz (anthroturbation)
Absence of alteration	Absence of metamorphism and strong diagenetic alteration to allow recognition of primary geochemical signals, free from serious overprinting.	Metamorphism and diagenetic alteration of Anthropocene strata is not currently an issue; leaching of terrestrial profiles may be problematic.	No sites
Abundance and diversity of fossils	Abundant and diverse well-preserved fossils throughout critical interval; traditionally an open-marine continental shelf setting is best as both oceanic and neritic species, and indeed pollen and other small fossils washed in from rivers, may co-occur, allowing	Oceanic biotas are insufficiently isochronous in dispersal/ disappearance to represent a primary marker in this case; precedents in the Quaternary comprise GSSPs in non-fossiliferous archives.	East Gotland Basin; Flinders Reef; West Flower Garden Bank; Antarctic Peninsula; Ernesto Cave; Karlsplatz

Requirement	Explanation	Relevance for Anthropocene	Potential problem sites
	integration of marine and terrestrial records.		
Absence of vertical litho/ biofacies changes	Absence of vertical litho- or biofacies changes at or near the boundary minimizes the risk of a break in sedimentation or local palaeo-environmental perturbation responsible for a biofacies change. However, distinctive lithological boundaries can be used to provide visual correlation.	Deeper-water settings are typically favourable, but given the Anthropocene's brevity many environments will be suitable. Optimal to have a clear lithological boundary to place the GSSP to allow visual correlation between cores provided chronology shows no missing strata.	San Francisco Estuary, Flinders Reef, West Flower Garden Bank, Antarctic Peninsula, Ernesto Cave, Śnieżka, Karlsplatz (absence of lithological marker at boundary level)
Non-biostrat-igraphical methods of correlation	Non-biostratigraphical methods of correlation should be given more weight than biostratigraphical methods when choosing boundary levels and type-sections.	This requirement is most applicable to the Anthropocene where there are numerous near-isochronous novel particulate and geochemical markers and opens up non-traditional environments where biotic markers are absent.	No sites
Absolute dating	Whenever possible, a GSSP should be amenable to direct quantitative calibration, e.g., radiometric dating of an interbedded ash layer.	^{210}Pb dating is appropriate in many environments and there are many local, regional and global events that can be used to develop robust chronologies, e.g., the bomb-spike. Absolute quantitative dating due to annual/sub-annual layers used in combination with the above is considered most ideal.	East Gotland Basin, San Francisco Estuary, Śnieżka, Karlsplatz (lack annual layers)
Magneto-stratigraphy	A palaeomagnetic reversal is a desirable feature of any GSSP because it potentially allows precise correlation both in marine and terrestrial sequences, and even in ice cores using the ^{10}Be flux as proxy for palaeomagnetic field intensity.	There are no palaeomagnetic reversals or excursions around the Holocene–Anthropocene boundary; however, mineral-magnetic records can identify major deforestation and soil-erosion events or reflect particulate pollution from fossil-fuel burning, although these will tend to give localized signals.	Not applicable to Anthropocene
Astro-chronology	It is highly desirable for a GSSP to be tuned to the orbital time scale.	Orbital variations, even precession and its harmonics, have periodicities too long to be relevant for the Anthropocene.	Not applicable to Anthropocene
Chemo-stratigraphy	The chemostratigraphical record may yield secular excursions of direct or indirect global correlative value.	The chemostratigraphical record is most useful for displaying changes in anthropogenic pollution, but it can also record recent temperature increases, acidification and eutrophication.	No sites

Requirement	Explanation	Relevance for Anthropocene	Potential problem sites
Intensive research	The section should be well studied, with the results published in the peer-reviewed literature (and preferably international literature), allowing the GSSP to have maximum utility for local, regional, and global correlation.	This thematic set of articles represents the publication of the candidate and reference sites; all have received comprehensive analysis of multiple proxies.	Not applicable to Anthropocene
Accessibility	A GSSP should normally be easily accessible, both physically and politically, for all stratigraphers regardless of nationality. It should be available for responsible re-sampling by *bona fide* geologists.	The candidate GSSPs are mainly in cores that are held at suitable repositories and available for future investigation; new material can also be collected from the sites, which is why a visual marker of the GSSP is advantageous.	Karlsplatz (redeveloped)
Protection	The GSSP should be protected from degradation and development so that it can continue to serve its purpose as a standard reference indefinitely.	See above comment concerning core storage. The source locations of the cores may in cases be at risk of anthropogenic destruction and protected sites would be preferred.	Karlsplatz (no reference core in storage)

APPENDIX 2 DETAILS OF SELECTED REFERENCE SECTIONS

The following eight sites are included in this submission as reference sections for the base of the proposed Crawfordian stage. Despite having no formal basis, and not requiring final approval by their respective subcommission (in this case the SQS), they support the GSSP and SABSs in demonstrating correlation of the boundary into other depositional environments elsewhere in the world, using a range of stratigraphic proxy signals.

2.1 East Gotland Basin, Baltic Sea

Project Leader: Jerome Kaiser; Summarised by Colin Waters

Stratigraphic event signals representing mid-20th century Great Acceleration are recorded in the EMB201/7-4 core collected in 2018 from the anoxic brackish marine East Gotland Basin (57.2830°N, 020.1204°E), located in the exclusive economic zone of Latvia at a water depth of 241 m bsl. The core is kept refrigerated (4°C) in the core repository of the Leibniz Institute for Baltic Sea Research (IOW, Germany). Collection of core in such deep waters requires a substantial research vessel. Details of the reference section core and of the site are provided by Kaiser *et al*. (2023).

Human-driven eutrophication impacts on the Baltic Sea ecosystem include water deoxygenation with the spread of hypoxic or ‘dead’ zones in deep basins, leading to

almost permanently hypoxic conditions below 80 m since the 1950s with euxinia in its deepest part. This prevents colonization and bioturbation of the sediments by benthic fauna. In the reference core the transition from underlying grey, homogeneous silty clay with low organic carbon content to brown, dark brown and black hemipelagic silty clays with high organic carbon content (5–15%) occurs around 27 cm depth in the core, at the base of the proposed Crawfordian stage (Figure EGB1a and h). Although laminated, the sediments are not annually varved. These anoxic conditions were interrupted by occasional brief Major Baltic Inflows (MBIs) comprising intrusions of oxygen-rich waters which deposited mm-thick Mn carbonate-rich layers and/or increased trace elements such as Co and V. The timing of these inflows is known and they provide useful markers for defining the chronology of the core (1978, 1994, 2003 and 2014 CE, with tentatively four others in 1964, 1967, 1970 and 1972 CE). Other constraints on the age model include the ^{137}Cs peak for the Chernobyl accident in 1986 CE at 15.5 cm depth, the first occurrence of DDT in 1950 CE (see below) and increase in polyaromatic hydrocarbons in 1870 CE.

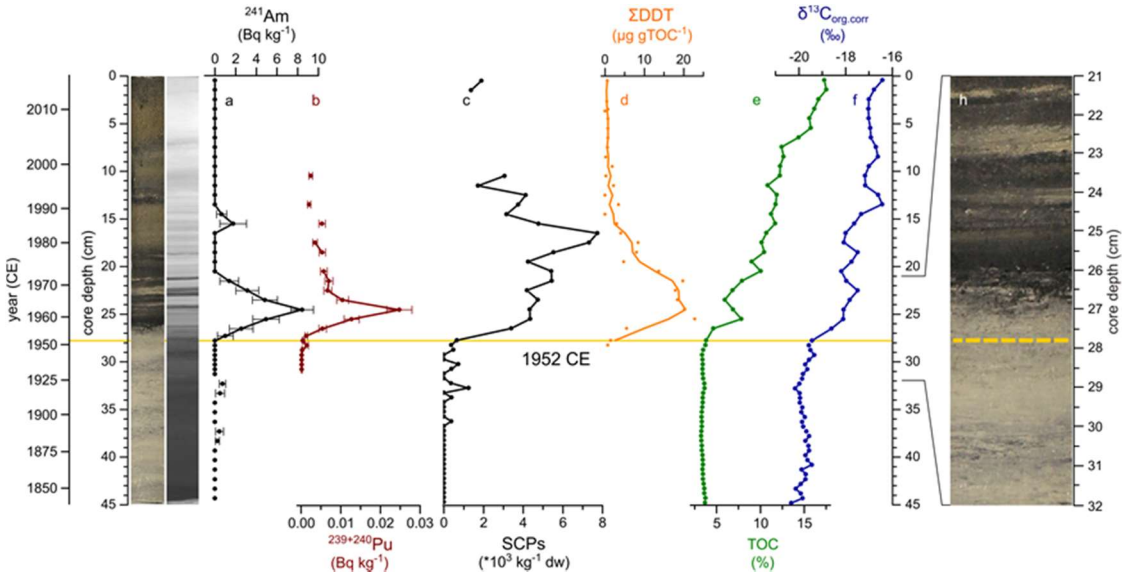

Figure EGB1. Pictures of core EMB201/7-4 (true colour and radiography), with the markers (a) ^{241}Am, (b) $^{239+240}$Pu, (c) spheroidal carbonaceous particles (SCPs), (d) ΣDDT, (e) Total organic carbon (TOC) and (f) δ^{13}Corg. A close-up (h) indicating the level of the base of the Crawfordian stage at 27.8 cm in the core is represented by a yellow dotted line. From Kaiser et al. (2023).

Key markers that allow correlation with the base of the Crawfordian stage GSSP

- ^{241}Am and $^{239+240}$Pu profiles show similar patterns (Figures EGB1b and c; EGB2a and b), with both close to the detection limit below 28.8 cm depth (1947 ± 4 CE), starting to increase at 27.3 cm depth (1953 ± 4 CE) and reaching a maximum at 24.5 cm depth (1963 ± 4 CE). Above this upper depth, the activities of both radionuclides decrease abruptly, but with a second sharp peak coincident with the ^{137}Cs peak at 15.5 cm depth. ^{240}Pu/^{239}Pu values (Figure EGB2c) above 0.30 between 1947 and 1950 CE (28.8–28.3 cm depth) suggest a main radionuclide source from test sites in the Pacific Proving Grounds, while values

below 0.19 since 1953 ± 4 CE (above 27.3 cm depth) are typical of global fallout. The base of the upturn in ^{241}Am and $^{239+240}$Pu profiles and shift to lower ^{240}Pu/^{239}Pu values occur 0.5 cm above the base of the Crawfordian stage in this core.

- F^{14}C (Figure EGB2d), the normalised fraction of ^{14}C, is relatively stable between 30.8 and 27.3 cm depth (1933–1953 CE) and starts increasing at 26.5 cm depth (1956 ± 4 CE), reaching a maximum between 23.5 and 20.5 cm (1966–1974 CE). The base of the upturn in F^{14}C is thus 1.3 cm above the base of the Crawfordian stage as recognised in this core.

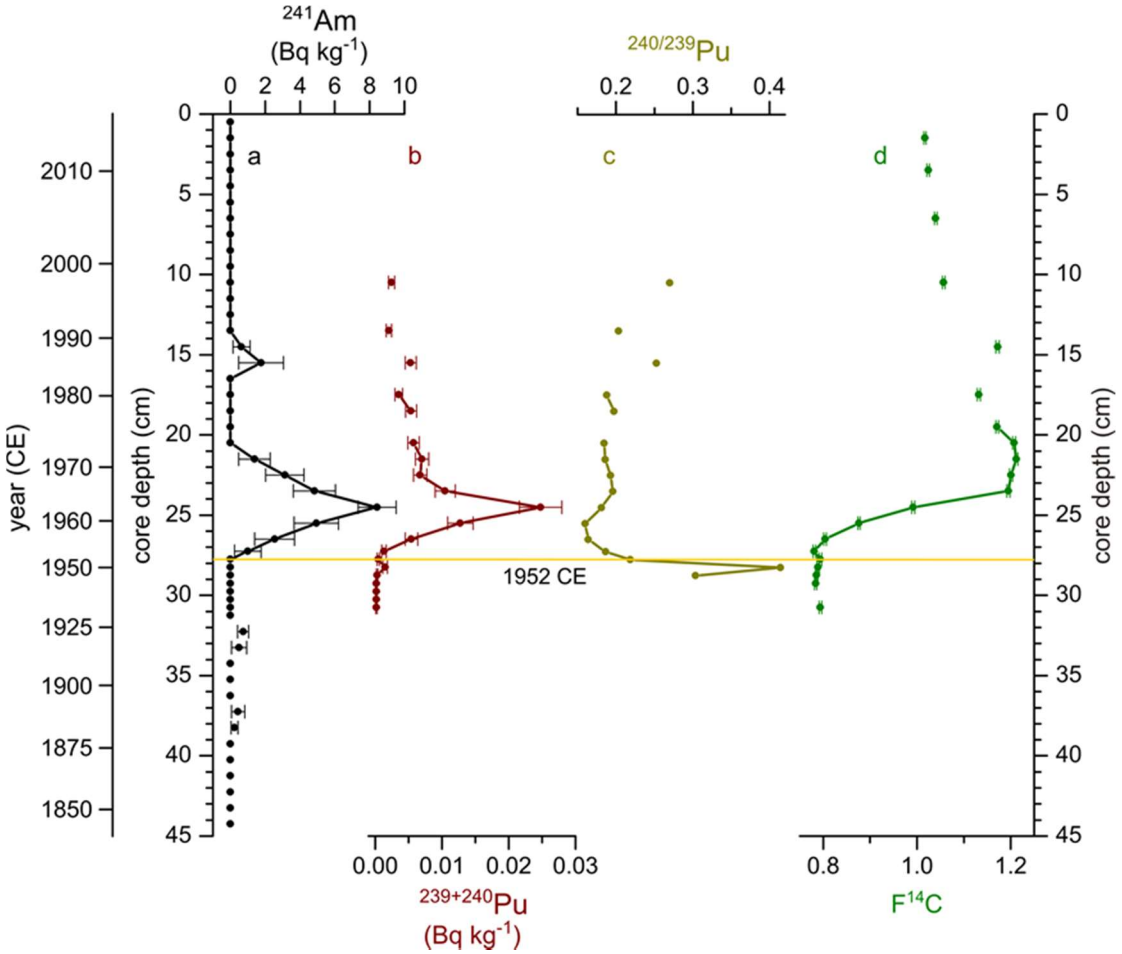

Figure EGB2. Depth profiles of (a) ^{241}Am and (b) $^{239+240}$Pu activities, (c) ^{240}Pu/^{239}Pu, and (d) F^{14}C (fraction modern of radiocarbon) in core EMB201/7-4. From Kaiser et al. (2023).

- A lowest appearance of spheroidal carbonaceous particles (SCPs) (Figure EGB1d) occurs at 36.3 cm depth (1897 ± 8 CE), but SCP contents remain low and sporadic until 27.3 cm depth (1953 ± 4 CE), when SCP contents increase, initially rapidly, through to a peak at 16.5 cm depth (1983 ± 3 CE). The base of the rapid upturn in SCPs is taken to be 0.5 cm above the base of the Crawfordian stage in this core.
- ΣDDT (Figure EGB1e) is below the detection limit between 44.8 and 28.8 cm depth (1840–1947 CE) and increases rapidly at 28.3 cm depth (1950 ± 4 CE) to

reach a maximum between 25.5 and 21.5 cm depth (1960–1971 CE). The base of the rapid upturn in ΣDDT is taken to be 0.5 cm below the base of the Crawfordian stage in this core.

- Both TC and TOC values (Figures EGB1f; EGB3a and b) are relatively constant around 3–4% below 29.8 cm depth (1940 ± 5 CE) above which they increase gradually to reach 19.8 and 17.3% at the top of the core, respectively. The base of the upturn in TC and TOC values is taken to be 2.0 cm below the base of the Crawfordian stage in this core.
- TN values are <0.5% below 27.8 cm depth (1952 ± 4 CE), followed by a gradual increase to the top of the core, where the values reach 2% (Figure EGB3c). The base of the upturn in TN values is taken to be at the base of the Crawfordian stage in this core.
- The C/N ratio (Figure EGB3d) ranges between 10 and 12 below 27.8 cm depth (1952 ± 4 CE), and between 8 and 10 above 23.5 cm depth (1966 ± 4 CE). The base of the decrease in C/N ratio is taken to be at the base of the Crawfordian stage in this core.

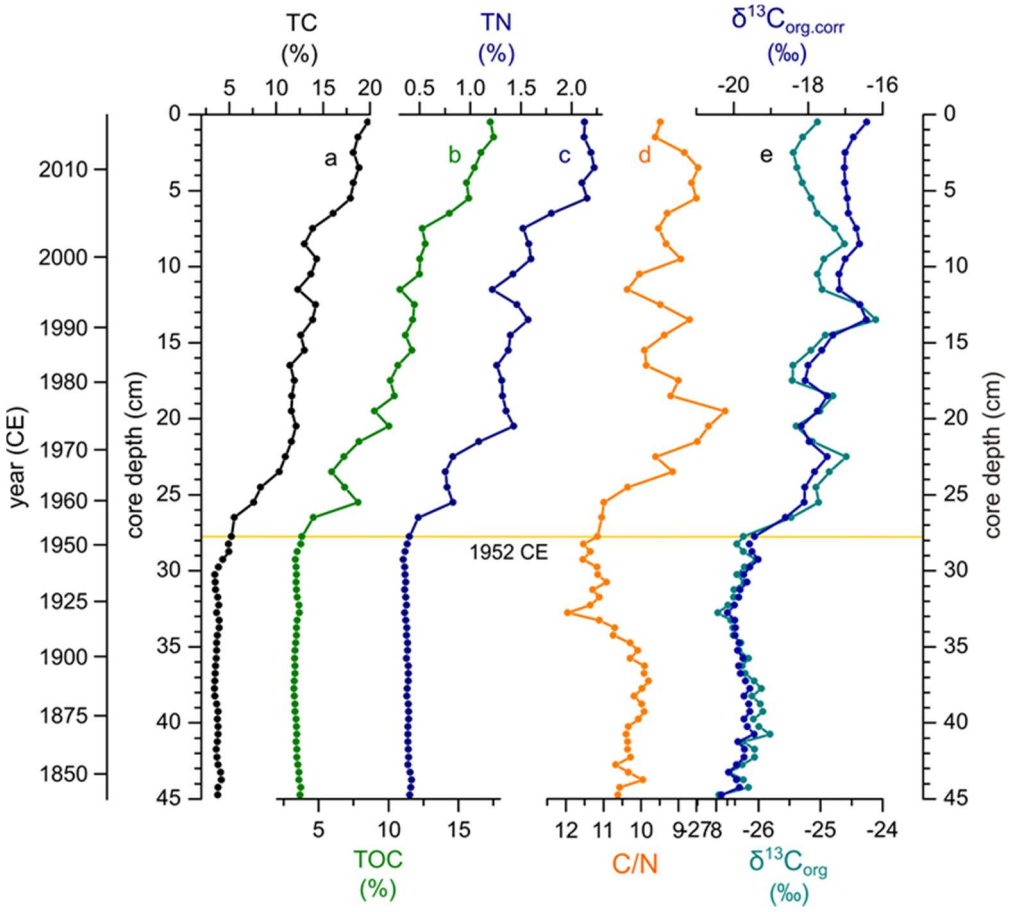

Figure EGB3. Depth profiles of (a) total carbon (TC), (b) total organic carbon (TOC), and (c) total nitrogen (TN) contents, (d) C/N (reversed plotted), (e) δ^{13}Corg and δ^{13}Corg.corr in core EMB201/7-4. From Kaiser et al. (2023).

- The bulk organic matter δ^{13}C (δ^{13}Corg) presents an abrupt 1.2‰ shift from −26.2 ± 0.2‰ below 27.8 cm depth (1952 ± 4 CE) to −25.0 ± 0.3‰ above this

depth (Figures EGB1g; EGB3e). The base of the shift to less negative $\delta^{13}C$ values is taken to be at the base of the Crawfordian stage in this core.

- Hg/Al, Cu/Al, Zn/Al, and Pb/Al values (Figure EGB4a–d) increase markedly from 28.8 cm depth (1947 ± 4 CE), with the ratios highest between 24 and 18 cm depth (1966–1978 CE). The shift to higher Hg/Al, Cu/Al, Zn/Al, and Pb/Al values is taken to be 1 cm below the base of the Crawfordian stage in this core.

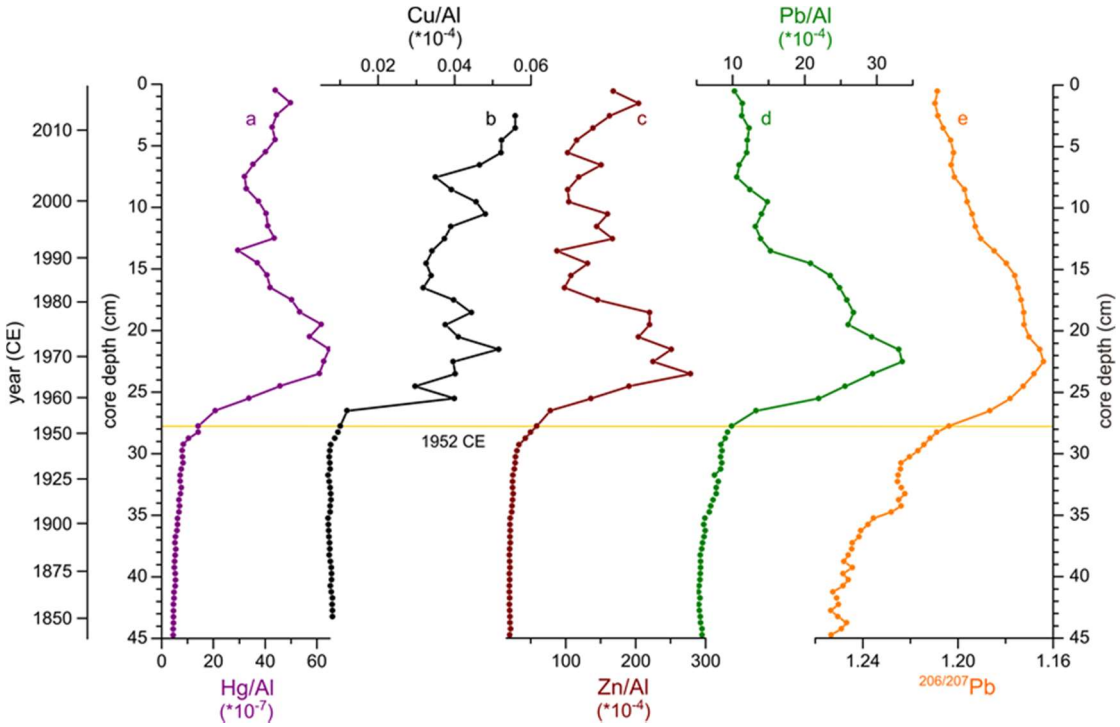

Figure EGB4. Depth profiles of (a) Hg/Al, (b) Cu/Al, (c) Zn/Al, (d) Pb/Al and (e) $^{206}Pb/^{207}Pb$ (reversed plotted) in core EMB201/7-4. From Kaiser et al. (2023).

- Above 22.5 cm depth (1969 ± 4 CE), $^{206}Pb/^{207}Pb$ values increase to the top of the core (Figure EGB4e), reversing a decreasing trend between 38.8–22.5 cm depth (1873–1969 CE), but with a marked inflexion at 28.8 cm depth (1947 ± 4 CE). The marked inflexion in $^{206}Pb/^{207}Pb$ ratio to lower values is taken to be 1 cm below the base of the Crawfordian stage in this core.
- The biotic markers brassicasterol and tetrahymanol contents increase significantly between 26.5 cm depth (1956 ± 4 CE) and the top of the core (Figure EGB5a and b). The lowest occurrence of faecal lipids (the sum of coprostanol and epi-coprostanol) at 26.5 cm depth (1956 ± 4 CE), increasing until the top of the core (Figure EGB5c). These biotic markers occur 1.3 cm above the base of the Crawfordian stage in this core.

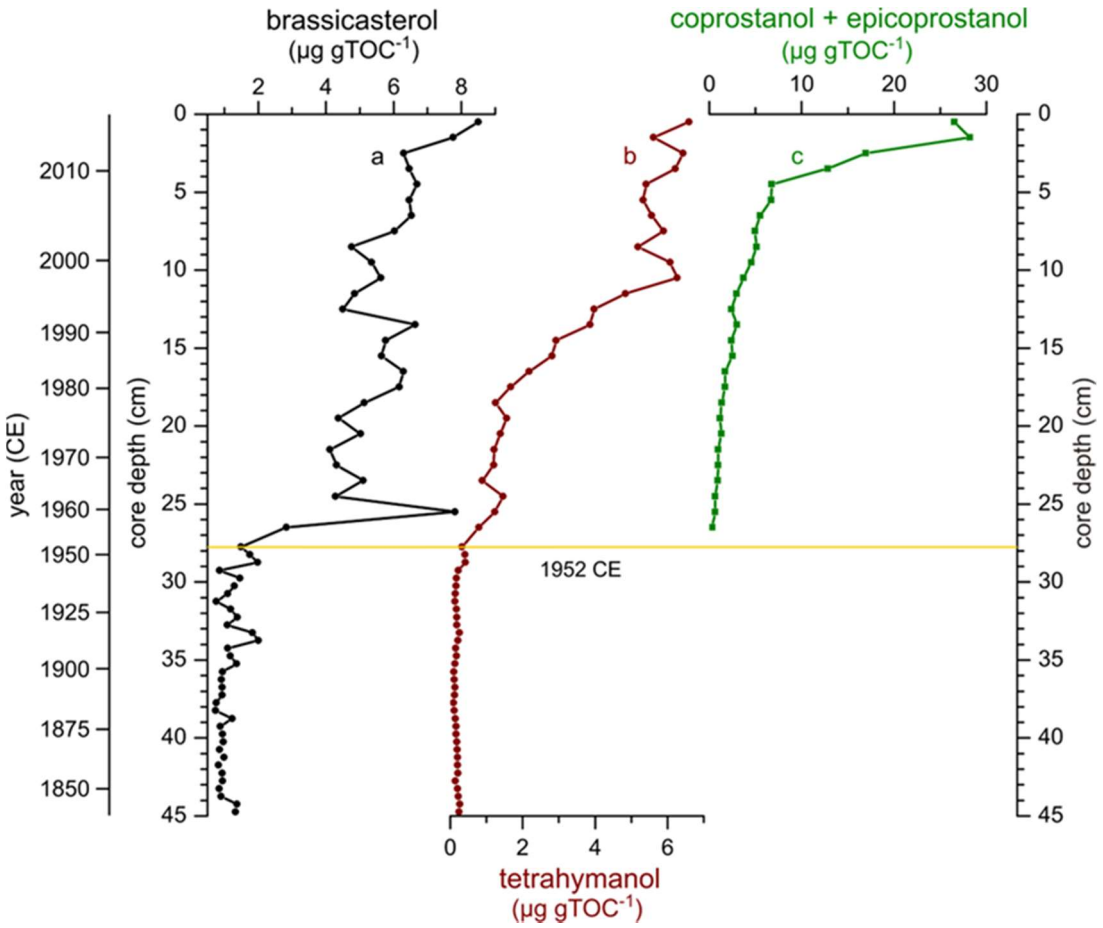

Figure EGB5. Depth profiles of (a) brassicasterol and (b) tetrahymanol contents, and (c) the sum of coprostanol and epicoprostanol contents in core EMB201/7-4. From Kaiser et al. (2023).

2.2 Ernesto Cave, Italy

Project Leader: Andrea Borsato; Summarised by Ian Fairchild

Two annually laminated calcitic stalagmites (ER77 and ER78) from Grotta di Ernesto display sulfur and radiocarbon records that document the base of the proposed Crawfordian stage with a decadal-scale time lag. The cave is located in the Province of Trento (Italy), in the Italian Pre-Alps (11.65751°E, 45.97723°N) at 1167 m asl on the north-facing slope of a forested karst plateau. The cave has a simple morphology of a descending tube and these stalagmites formed 30 m below ground level. A comparable stalagmite from 20 m depth has also been studied and further material could also be collected. Sawn and thin sectioned speleothem material is archived at the Museo delle Scienze in Trento, Italy. Details of the reference section speleothems and of the site are provided by Borsato *et al*. (2023).

The annual chronology has been verified by a series of U-Th dates spanning the last 8000 years. Increased growth rate associated with changed crystal fabric from around 1840 CE (Figures EC1, EC2) corresponds with higher temperatures at the end of the Little Ice Age and an increase in $\delta^{13}C$ likely related to anthropogenic deforestation

(Figure EC2). An exceptionally thick lamina marks the temporary opening of the cave entrance from autumn 1983 CE (Figure EC1).

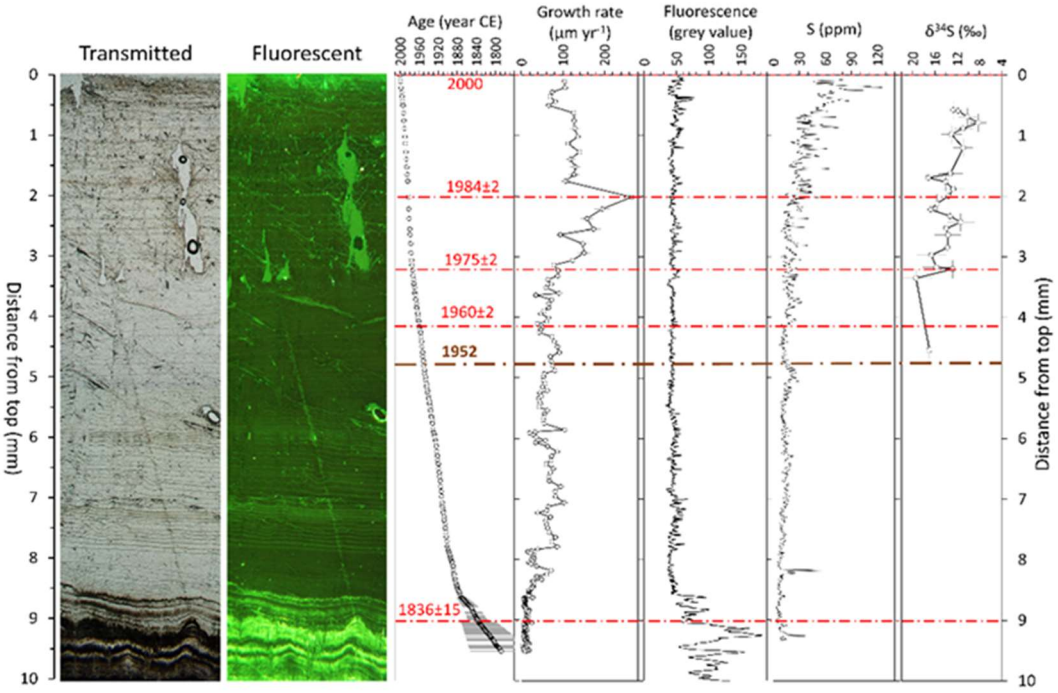

Figure EC1. Thin section image in transmitted and fluorescent light (470 nm) of the topmost section of stalagmite ER78, which was collected in 2000, compared with the annual growth rate and age model derived from layer counting (Frisia et al., 2003), the fluorescence signal (Borsato et al., 2023), the SO_4-S concentration (Frisia et al., 2005), and $\delta^{34}S$-SO_4 (Wynn et al., 2010). The proposed base of the Crawfordian stage at 1952 CE is highlighted together with four other time markers: (1) The passage from porous microcrystalline to compact columnar calcite associated with onset of faster growth at 8.6 mm dft (lamina age 1836 ± 15 CE); (2) the increase in the annual growth rate and S concentration (lamina age 1960 ± 2 CE); (3) a shift towards depleted $\delta^{34}S$–SO_4 (lamina age 1975 ± 2 CE) that demonstrates an additional source of stalagmite sulfur originating from industrial pollution (Wynn et al., 2010); (4) the sudden increase of growth rate along a thin micro-detrital layer that corresponds to the opening of the cave entrance in autumn 1983 followed by archaeological excavations during summer 1984 (Dalmeri, 1985) and re-sealing the entrance in autumn 1984. Note the inverted scale for $\delta^{34}S$.

The site has been intensively studied over 30 years as a model for understanding process controls on the creation of speleothems. The annual lamination reflects a combination of two factors. Seasonal variation in the carbon dioxide level of cave air affects growth rate, carbon isotope systematics and incorporation of some trace elements. A high water-excess in autumn leads to the formation of a thin fluorescent lamina with a distinctive trace element composition, enhanced during periods of deforestation. Most trace element and isotope proxies are related to local environmental processes, whereas sulfur records continental-scale and radiocarbon hemispheric-scale atmospheric pollution. Pu and SCPs are not detectable.

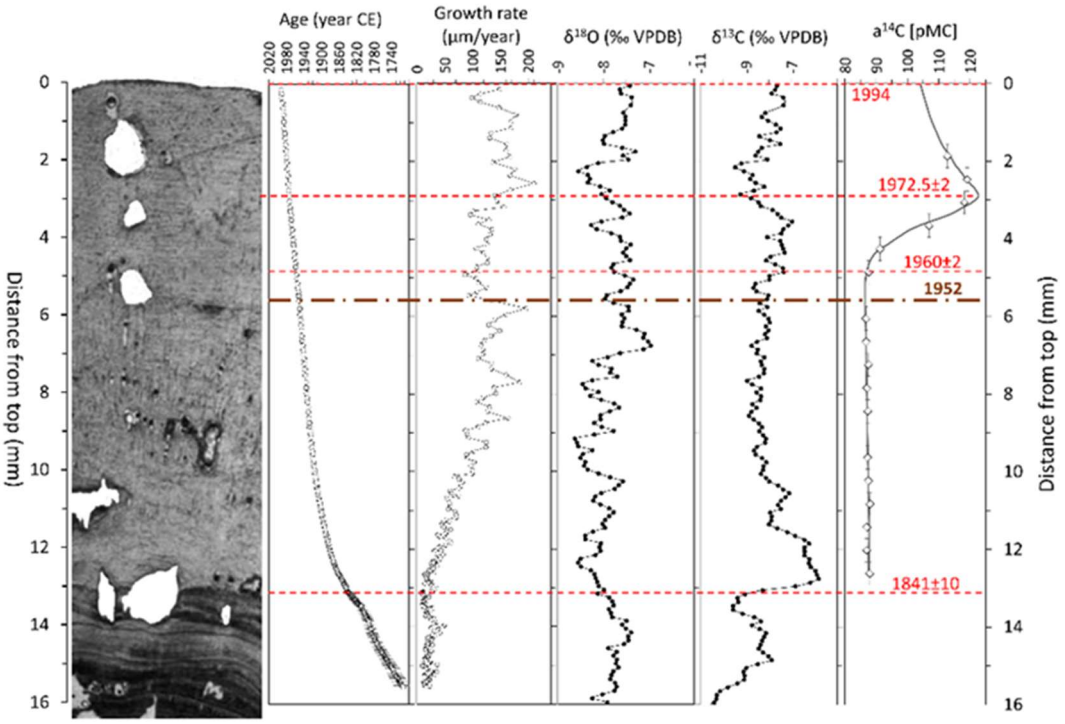

Figure EC2. Thin section image in transmitted light of the topmost section of stalagmite ER77, which was collected in 1994, compared with the age model derived from annual-layer counting (Frisia et al., 2003), the oxygen and carbon isotope ratios (Scholz et al., 2012), and the ^{14}C activity in percent modern carbon (Fohlmeister et al., 2011). The grey line in the a^{14}C graph is the modelled ^{14}C activity. The proposed base of the Crawfordian stage at 1952 CE is highlighted together with three time-markers: (1) The passage from porous microcrystalline to compact columnar calcite corresponding to the onset of faster growth at 13.1 mm dft (lamina age 1841 ± 10 CE) marked by a steady increase in the growth rate and a sharp rise in $\delta^{13}C$; (2) the first increase in ^{14}C activity at 4.8 mm dft (lamina age 1960 ± 2 CE) and (3) the modelled maximum in ^{14}C activity at 1972.5 ± 2 lamina age.

Key markers that allow correlation with the base of the Crawfordian stage GSSP

- Sulfur, present as trace sulfate substituting for carbonate ions in the calcite lattice, shows anthropogenic shifts in concentration and $\delta^{34}S$ composition reflecting an atmospheric pollution episode from around 1950 CE which peaked Europe-wide in the early 1970s (Figure EC1). Sulfate concentration records are noisy because of pH-related seasonal shifts and become noisier with higher mean values around 1960 CE. Annual mean values progressively increase reaching a maximum in the early 1990s, following which cave dripwater monitoring demonstrates a fall in sulfate. This is a 20-year lag from the atmospheric sulfur peak. Sulfur isotope results demonstrate a comparable lag, with the first downward shifts around 1975 CE and minimum value of around +10‰ attained in the early 1990s.
- The anthropogenic increase in ^{14}C is clearly recorded in $CaCO_3$, albeit attenuated and lagged as is typical in cave precipitates (Figure EC2). Minimum

sample size dictated that radiocarbon samples span 4-5 years, corresponding to a spatial resolution of 0.6 mm. The shape of the radiocarbon profile has been optimised using a soil carbon model including different organic matter pools with differing carbon turnover times. There is a steady background prior to nuclear atmospheric testing with the first higher data point corresponding to the sample from the year 1960 ± 2 CE. The modelled best-fit peak is at 122.7 pmC in 1972.5 CE, showing a delay of about 10 years with respect to the northern hemispheric atmospheric ^{14}C peak of 197.3 pmC in 1963.6 CE.

2.3 Karlsplatz, Vienna, Austria

Project Leader: Michael Wagreich; Summarised by Colin Waters

The composite section (Vienna Urban archaeology site # 2019_26) in a temporary exposure of layered urban anthropogenic sediments was studied in 2019–2021 at an archaeological site at the Wien Museum, Karlsplatz, Vienna, Austria (48.199167°N, 16.372611°E). The maximum depth of excavation was 6.3 m, with a 0.64 m-thick main reference section through the mid-20th century interval (Figure KP1). Details of the sections are provided by Wagreich *et al*. (2023). Sample splits are archived at the collection of the Department of Geology, University of Vienna, but the site has been redeveloped and is no longer accessible other than through coring nearby, in front of the museum.

Phases of redevelopment of the site are preserved in the section, with short gaps in deposition between the development phases evident as unconformities, including at the base of the proposed Anthropocene succession. The chronology is determined from artefacts (technofossils) in association with archival records of the site's development (Mosser, 2019; Mosser & Litschauer, 2021); there are no annual lamination, ^{210}Pb dating or ^{137}Cs profiles to provide additional constraints. Key developments include, in order of decreasing age (Figure KP1): (i) The oldest road structures date from the 18th century, and are interbedded with some fluvial sands from flooding events by the Wien River (up to 4.2 m below ground surface; samples AZ31 and AZ34); (ii) road structures of the first half of the 19th century (around 1825), with Wien River embankment including an ash and slag layer (sample AZ29), waste products from the metal-working industry; (iii) in 1867, the first major regulation of the Wien River was finished, the location of the river bed was redirected, and new roads with cobblestone pavements were built; (iv) during 1894–1900, the containment of the Wien River into an underground canal and filling of the natural course of the river with urban rubble (sample WMP3) took place, overlain by a soil (sample AZ10); (v) from 1922 to 1934 a sales hall was located at the site, but it was abandoned and demolished in 1934, resulting in an unbuilt area with gravelly sand and stony material (from 64–44 cm depth; sample AZ7); at the end of WW2 war rubble (a sandy gravel from 44–31 cm depth; sample AZ6 and WM5) was distributed across the site; (vi) groundwork for the Wien Museum started in the 1950s with deposition of sandy to silty, humus-rich layers and soils, with increased bioturbation towards the surface (8–31 cm depth; samples AZ4 and AZ5); and (vii) the opening of the Wien Museum in 1959, with planation of the park in front of the Wien Museum associated with surface topsoils (0–8 cm depth; sample AZ3).

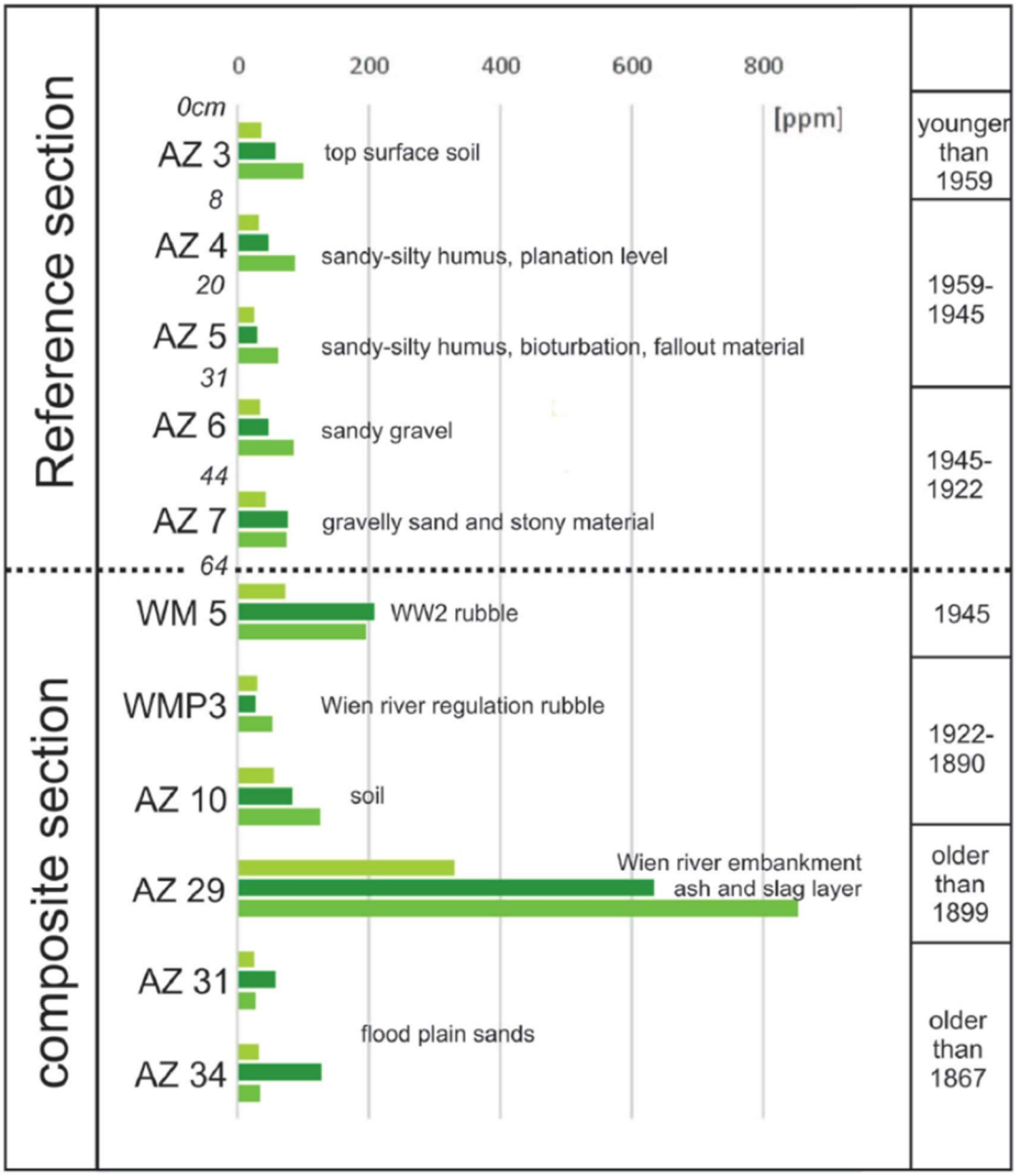

Figure KP1. Copper (light green, top), lead (dark green, middle) and zinc (medium green, base) concentrations in ppm of the reference section and the composite section. The ages are constrained by historical and archaeological site data. From Wagreich et al. (2023, fig. 4).

Key markers that allow correlation with the base of the Crawfordian stage GSSP

- Several artificial radionuclides, including the plutonium and uranium isotopes ^{239}Pu, ^{240}Pu and ^{236}U (Figure KP2), were found in the post-1945 CE layer taken as the basal layer of the Anthropocene (sample AZ5) comprising sediments transported to the area. The ^{240}Pu/^{239}Pu isotope ratio in sample AZ5 clearly points to the presence of global atmospheric atomic bomb fallout material of the 1950s. The post-1959 CE soils (sample AZ3) have the highest ^{239}Pu concentrations, which is expected given that maximum global fallout in the Northern Hemisphere was in 1963 (UNSCEAR, 2000); The ^{240}Pu/^{239}Pu ratio in sample AZ3 is consistent with global fallout signals and not the 1986 Chernobyl

accident. Pu was also present in the topmost part of the WWII debris (WM5), but in considerably lower concentrations, suggesting some mobility from above due to illuviation and/or human activity. No Pu was detected in sediments older than 1922 CE (sample WMP3). Thus, the bomb-spike can be identified and used as a primary stratigraphic marker even in coarse urban anthropogenic sediments, showing the correlation potential of these radionuclide markers across diverse environments.

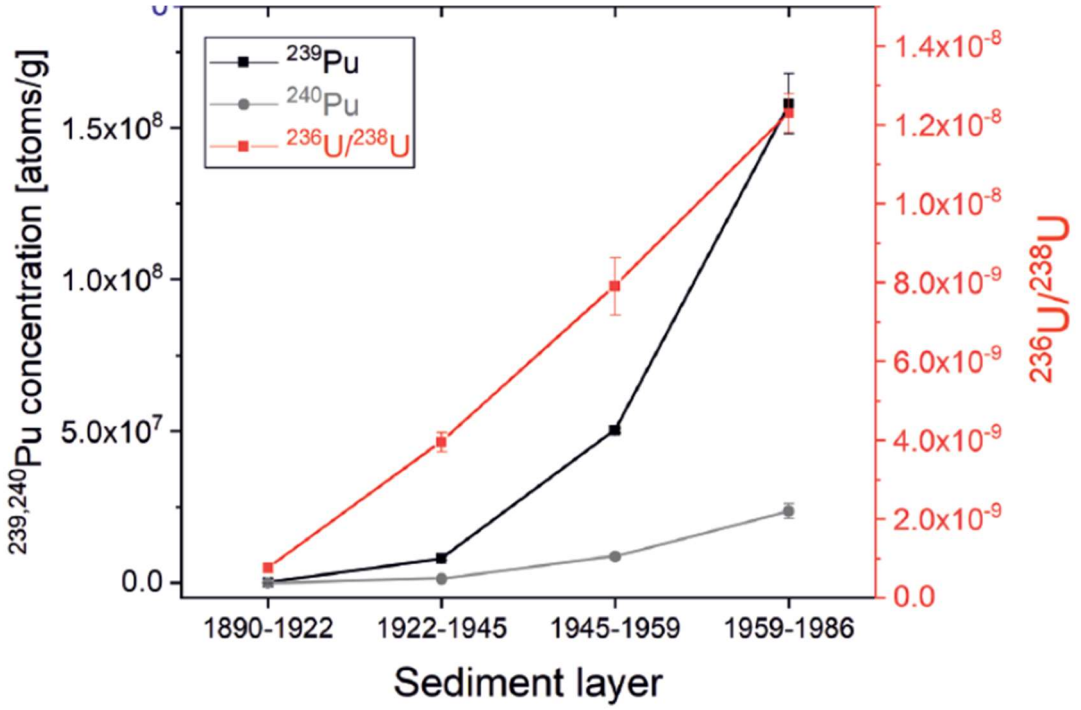

Figure KP2. Summary of main marker concentrations of the four time slices archived in the Karlsplatz section and analysed for plutonium and uranium isotopes lead. Uncertainties are reported as ± 1σ. From Wagreich et al. (2023, fig. 5). Samples WMP3 (1890-1922 CE), WM5 (1922-1945 CE), AZ5 (1945-1959 CE) and AZ3 (1959-1986 CE).

- The earliest macroplastics are found in the layer of WWII debris (sample AZ6) and are present in the topmost post-1959 CE soil (sample AZ3); intervening sediments have been brought into the area and may have been sieved and manually sorted, potentially removing macroplastics from these sediments.
- The layer of WWII debris (sample WM5) shows high trace-metal concentrations, including Pb, Cu and Zn (Figure KP1), having strong affinity with anthropogenic contamination. A second, more prominent peak (sample AZ29) comes from the Wien River embankment and relates to an ash and slag layer probably older than 1867 CE. Anthropocene successions show relatively low trace-element concentrations (samples AZ3–5).

2.4 North Flinders Reef, Australia

Project Leader: Jens Zinke; Summarised by Colin Waters

The coral composite cores were collected from a *Porites* sp. coral colony in 1992 (FLI01A) and 2017 (FLI05A) from the North Flinders Reef, located in the Coral Sea

250 km off the coast of Queensland, NE Australia (17.71790°S, 148.45102°E) at a water depth of 5–10 m bsl. The composite core is 3.33 m long, with the base of the core dated 1708 CE. All cores are stored in the core depository of the Australian Institute of Marine Science. Details of the reference section core and of the site are provided by Zinke *et al*. (2023).

The chronology comes principally from annual growth layer counting. The two Flinders Reef coral cores preserve archives from 1710 to 1992 CE (FLI01A) and 1835 to 2017 CE (FLI05A), respectively, with analyses to ensure a 4-year overlap of cores (FLI05A analysed for 1988 to 2017 CE). The base of the Crawfordian stage is located in FLI01A. The offshore oceanic reef setting is less vulnerable to local human influences than those closer to the coast. It is also part of the Coral Sea Marine Park, one of the largest isolated marine parks in the world, so the area is both protected and actively managed.

Key markers that allow correlation with the base of the Crawfordian stage GSSP

- The plutonium ($^{239+240}$Pu) signal (taken at two-yearly intervals) has low activities and shows marked increases in 1954, 1958, 1960 and 1966 CE (Figure NFR1a). This is consistent with sources from the nearby Pacific Proving Grounds.
- Coral $F^{14}C$ shows a first increase above pre-bomb levels in 1952 CE, with the start of a clear and pronounced radiocarbon bomb-spike ($\Delta^{14}C$ recorded annually in the boundary interval) at 36.9 cm depth (1958 CE), which peaks in 1980 CE (Figure NFR1a). There is a 3-year lag in the onset of the radiocarbon bomb-spike (consistent with a Southern Hemisphere to Northern Hemisphere lag), and a 5–10 years lag in the peak compared with the West Flower Garden Bank Reef (see below). The first increase in coral $F^{14}C$ coincides with the base of the Crawfordian stage in this core at 43.16 cm.
- Sr/Ca annually-resolved records reveal low values (warm SSTs) indicating accelerated warming from 1950 CE with warm SST through to 1992 CE (FLI01) (Figure NFR1d).
- A shift in $\delta^{18}O$ (resolved annually) in 1958 CE in which a long-term decreasing trend is followed by an increase consistent with potential salinification following a long-term warming/freshening trend (Figure NFR1g).
- A reversal in the $\delta^{15}N$ trend (resolved annually) around 1955 CE, from steady decline between 1710 and 1954 CE to stable values through to 1992 CE (FLI01), suggesting ocean denitrification (Figure NFR1e).

Figure NFR1 [over page]. Flinders Reef geochemical signatures for cores FLI01A (F1), FLI02A (Calvo et al., 2007; Pelejero et al., 2005) and FLI05A (F5). All proxies in (d–g) plotted as centred anomalies. (a) radiocarbon (F1/F5 = orange) and plutonium concentrations (F1/F5 = light green); (b) Ba/Ca ratio; (c) reconstructed pH (Pelejero et al., 2005); (d) Sr/Ca ratios; (e) nitrogen isotopes; (f) carbon isotopes; and (g) oxygen isotopes. The proposed base of the Crawfordian stage at 1952 CE is indicated by the pink line. Depth in core (in m) also indicated and years in Common Era (CE).

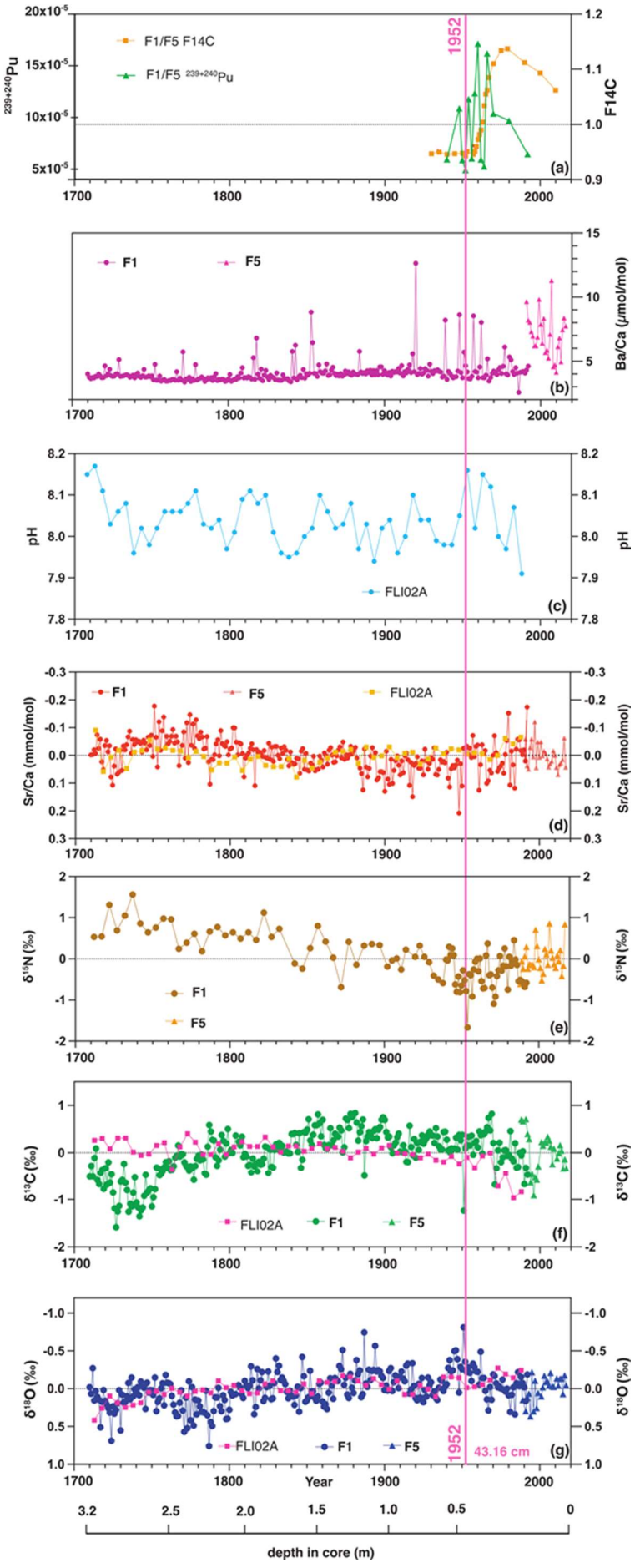
F1/F5 F14C
F1/F5 239+240Pu
239+240Pu
F14C
1952
(a)
F1
F5
Ba/Ca (μmol/mol)
(b)
pH
FLI02A
(c)
Sr/Ca (mmol/mol)
(d)
δ15N (‰)
(e)
δ13C (‰)
(f)
δ18O (‰)
43.16 cm
(g)
Year
depth in core (m)

- A decrease in $\delta^{13}C$ (resolved annually) which accelerates from 1970 CE (FLI01) (Figure NFR1f) probably due to the Suess effect of increasing uptake in surface oceans of isotopically lighter carbon derived from burning of fossil fuels.

2.5 Palmer ice core, Antarctic Peninsula

Project Leader: Elizabeth Thomas; Summarised by Colin Waters

The Palmer ice core was collected in 2012 without use of drilling fluid from close to the ice divide (73.8521°S, 65.4526°W), associated with minimal ice movement, distant from mountains that could provide local dust sources, and at high altitude (1897 m asl) so less sensitive to local climate change and unlikely to be affected by any surface melting. The region receives the highest amount of snowfall of all Antarctic regions (~4 m pa) resulting in greater ice accumulation rates and relatively more recent lock-in of gas chemistries in air bubbles. The Palmer ice core represents one of the most pristine environments on Earth, and here tested the extent to which any anthropogenic record was clearly preserved. Details of the reference section core and of the site are provided by Thomas *et al*. (2023a).

The core is 133.45 m long, with the age of the ice at the base determined to be 1621 CE and the thickness of the Crawfordian stage estimated to be 34.91 m (1952 CE). Collection and transportation of ice core from this extremely remote site is a major undertaking. However, the Protocol on Environmental Protection designated Antarctica as a 'natural reserve' in 1998, ensuring that future scientific exploration of the Palmer site is not at risk of exploitation or political changes. The ice samples, and remaining archive, are kept at −25°C in a monitored, temperature-controlled freezer facility in the dedicated British Antarctic Survey ice core laboratories in Cambridge, UK.

The chronology is resolved through annual layer counting, determined through seasonal variations in non-sea salt sulphate, stable water isotopes and hydrogen peroxide (Emanuelsson *et al*., 2022). This chronology is supported by well-dated volcanic horizons identified in the sulfate record, with an estimated dating error of <6 months. The closest such marker to the base of the Crawfordian stage is a peak associated with the 1963 CE Agung (Indonesia) eruption and documented Chilean eruptions of Llaima (1945 CE) and Villarrica (1948/1949 CE). The Holocene-Anthropocene boundary occurs within the firn column, where air can move freely between the ice layers. The point at which the air-bubbles become fully-sealed is the close-off depth, reached at 62.8 m at this site.

Key markers that allow correlation with the base of the Crawfordian stage GSSP

- The lowest $^{239+240}Pu$ record (measured at bi-annual resolution) is 1945–1946 CE (37.16 m depth; Figure P1a), attributed to the earliest above-ground fission weapon testing, which commenced in the Pacific Proving Grounds in 1946 (UNSCEAR, 2000). Annual samples were analysed from 1900 CE onwards, but the earliest of several peaks in 1952–1953 CE (34.9 m) corresponds with the initiation of aboveground thermonuclear detonations and absolute maximum by 1960–1961 CE (30.48 m). Concentrations are low compared with Greenland

and Alpine ice cores. The lowermost peak in $^{239+240}$Pu coincides with the base of the Crawfordian stage in this core.

- The first documentation of SCPs in an Antarctic ice core is confirmed independently by optical microscopy and by SEM. The lowest SCPs are recorded in the ice layer from 1936 CE (40.48 m), and continue in very low concentrations for the remainder of the 20th century (Figure P1b; Thomas *et al.*, 2023b).

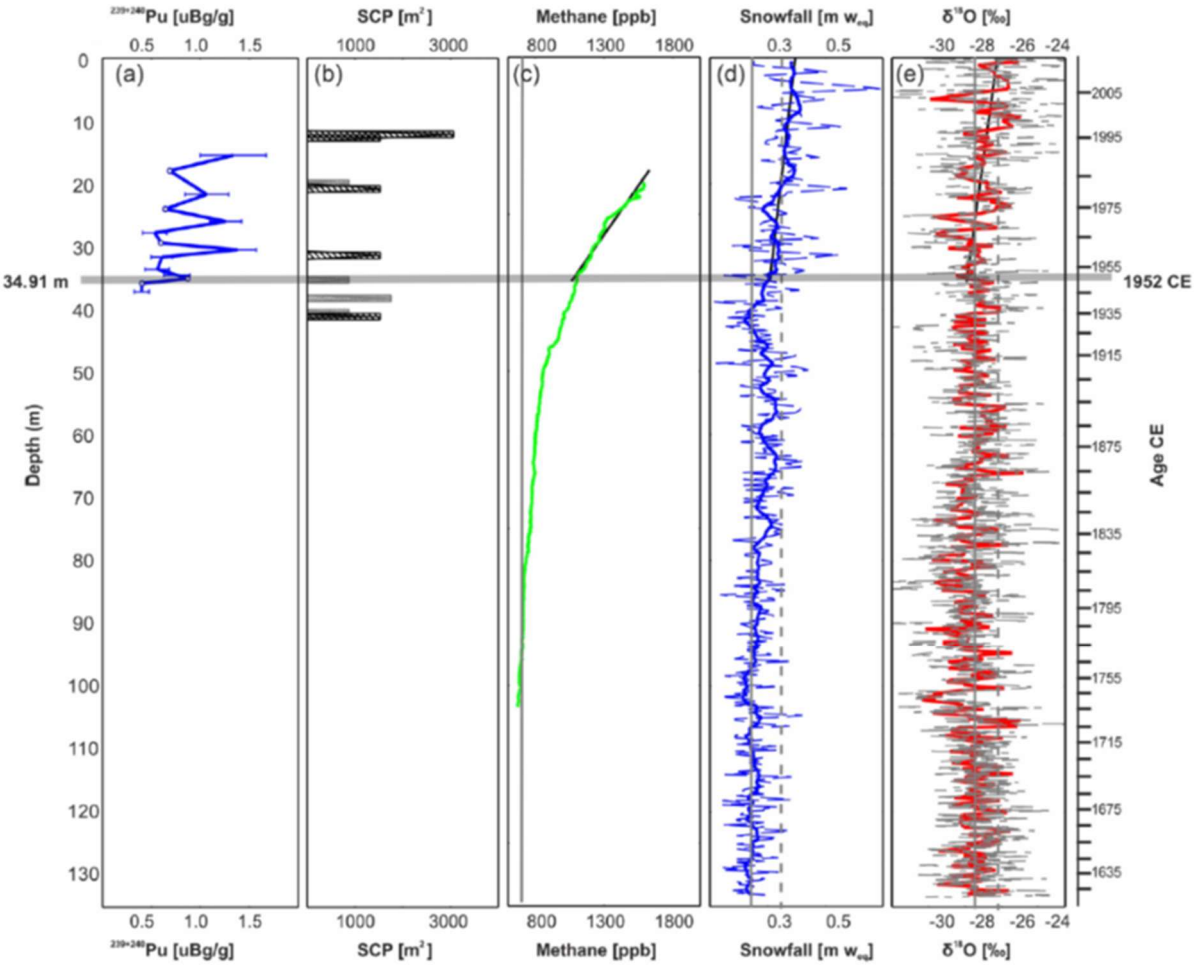

Figure P1. Anthropogenic proxies in the Palmer ice core in the context of the last 391 years. (a) Plutonium ($^{239+240}$Pu), with error bars, presented at 2-yearly resolution. Open circles indicate data below detection limit; (b) SCPs determined using discrete sampling (black bars, annual resolution) and continuous sampling (grey bars, 1–5-year resolution); (c) CH_4, (d) annual snowfall (metres of water equivalent) (dashed line) with running decadal mean (thick solid curve); and (e) $\delta^{18}O$ (‰) at 4 cm resolution (grey dashed curve) and annual averages (solid red curve). All data plotted on a depth scale (left axis), with age-scale shown on right axis. From Thomas et al. (2023).

- Methane analyses can be depth-shifted using a varying depth-age difference, producing a profile with a detectable inflexion as early as 1883 CE (± 5 years) and a more significant change in trend at 1958 CE (± 5 years) (Figure P1c). The oldest measurement corresponds to ~1719 CE (± 5 years) with a concentration of 645 ± 10 ppb and had doubled by 1969 CE. The concentration at the lock-in

depth (56.8 m) is 1839 ± 10 ppb, which corresponds with modern CH_4 concentration in the atmosphere.

- Stable water isotopes ($\delta^{18}O$) show seasonal cycles ranging from −33.12‰ (winter) to −20.51‰ (summer), but with decadal averages indicating warmer surface temperatures and snowfall rates become higher and more irregular towards the present, but both showing a shift from ~1930 CE (Figure P1e). $\delta^{18}O$ has been increasing at a rate of 0.22‰ per decade since 1952 CE.

2.6 San Francisco Estuary, California, USA

Project Leader: Stephen Himson; Summarised by Mark Williams

Details of the proposed reference core for San Francisco Estuary are provided by Himson *et al*. (2023). The reference section core (SFB-20A) was collected in April 2019 in the southern San Francisco Estuary (37.5495°N, 122.1831°W), approximately 4 km north-west of Redwood City, at a mean water depth of 10.5 m, and the core is 2.3 m in length. The core was recovered using a vibracorer on the USGS research vessel R/V Parke Snavely. Core SFB-20A is from an area determined to have experienced continuous deposition since 1858 CE (Foxgrover *et al*., 2022) and hiatuses are expected to be absent. The core is in permanent store at the British Geological Survey (BGS), Keyworth, Nottingham, UK.

The chronology of the core is determined via time series analysis which established a relationship between the annual peak in rainfall and the XRF record of Ti – a proxy for precipitation/fluvial runoff (Peterson & Haug, 2006). The sediment accumulation rate calculated is 3.4 cm/yr and is comparable with peak sedimentation rates measured elsewhere in the San Francisco Estuary (Fuller *et al*., 1999; Himson *et al*., 2023). An age profile is defined to 167 cm depth and then extrapolated to the base of the core, which is estimated to be at ~1952 CE, making the studied section entirely within the proposed Crawfordian Stage. Comparing the time series analysis with key biostratigraphical data from the core suggests that the sediment accumulation rate gives an approximation of age, but for some intervals may be a few years in error (Figure SFB1). Increasing Hg concentration from 190 cm depth and peaking at 130 cm is consistent with the time-series chronology, representing a spike in Hg production in the 1960s and 1970s (Figure SFB2). The ^{210}Pb age profile is also consistent with the time series analysis but is of lower resolution. ^{137}Cs and $^{239+240}Pu$ do not provide a useful chronology, possibly because of remobilisation of sediment more broadly within the estuary.

The importance of Core SFB-20A is its accumulation of a palaeontological record of the Great Acceleration, notably of the pan-Pacific trade. This is evident from the fossil record of four introduced species – all likely via the ballast water of international shipping: the northwest Pacific ostracods *Bicornucythere bisanensis* and *Spinileberis quadriaculeata,* the Japanese foraminifer *Trochammina hadai*, and the East Asian mollusc *Potamocorbula amurensis.* Notably these species have their first occurrence datums in the same relative order in the core as their known time of introduction (Figure SFB2), and they can be used to develop a high-resolution biostratigraphy of the proposed Crawfordian stage across San Francisco Estuary. *Trochammina hadai* is an intercontinental marker for deposits of the proposed Crawfordian stage in shallow

marine and estuarine deposits (e.g., Eichler *et al*., 2016; Tremblin *et al*., 2022; Bouchet *et al*., 2023).

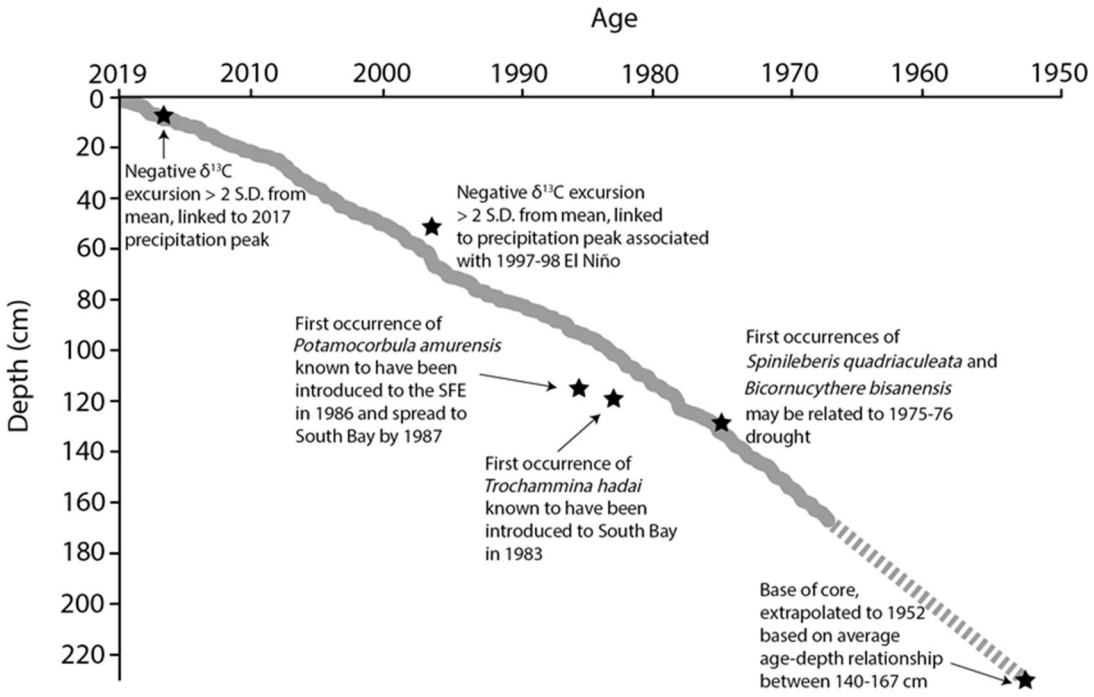

Figure SFB1. Age–depth profile of core SFB-20A derived from the times series analysis (grey curve width includes sampling error). The top of the core represents 2019 CE. The chronology is based on the conversion of rainfall to depth (see Himson et al., 2023). Plotting key biostratigraphical events here suggests that the time series analysis gives an approximation of age, but for some intervals may be a few years in error. Thus, the lowermost core occurrences of the foraminifer Trochammina hadai *and mollusc* Potamocorbula amurensis *are taken as 1983 and 1986 CE, respectively based on widely observed data from the estuary, whereas time series analysis would suggest these levels to be in the late 1970s. The age profile is defined to 167 cm depth (solid grey line) and then extrapolated to the base of the core (dashed grey line). From Himson et al. (2023, fig. 4).*

Key biostratigraphical markers that allow correlation with the Crawfordian stage GSSP

- The first occurrence datum of the ostracods *B. bisanensis* and *S. quadriaculeata* at 128 cm, a level approximating to 1975–1976 CE.
- The first appearance datum of the foraminifer *T. hadai* at 119 cm depth approximating to 1983 CE. The peak concentration of *T. hadai* is at 88 cm, with lower abundance towards the top of the core.
- The first appearance datum of the Amur River clam *P. amurensis* at 115 cm, approximating to 1986 CE.

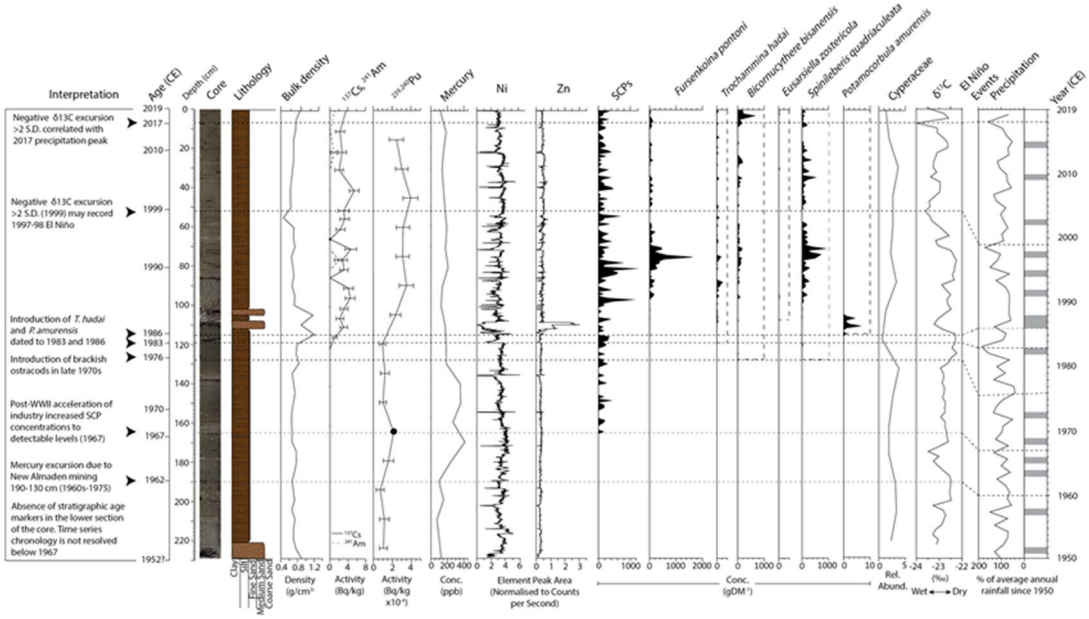

Figure SFB2. Summary of the stratigraphic signature of anthropogenic markers recorded in core SFB-20A. The chronology on the left is derived from the time series analysis and should be considered approximate for some intervals (see Figure SFB1), with the exception of the biostratigraphic signatures in 1983 and 1986 CE, which are considered more robust age markers. The chronology on the right is from historical records of precipitation and El Niño events. Interpreted events are represented by black dashed lines and include the mercury excursion and lowest occurrence of SCPs in the 1960s, the lowest occurrence of the East Asian ostracods Bicorncythere bisanensis *and* Spinileberis quadriaculeata*, which may be associated with the 1975–76 drought, and negative $\delta^{13}C$ excursions greater than 2 standard deviations from the mean at 52.5 and 7.5 cm which are correlated with peaks in the precipitation profile and dated to 1999 and 2017 CE. The sample at 165 cm in the profile of $^{239+240}Pu$ represents the Limit of Detection, LOD, value as $^{239+240}Pu$ was not definitively quantified in that sample. The top surface of the core is 2019 CE. From Himson et al. (2023, fig. 12).*

2.7 Searsville Lake, California, USA

Project Leader: M. Allison Stegner; Summarised by M. Allison Stegner, Anthony Barnosky and Elizabeth Hadly

Searsville Lake is a reservoir presently about 0.8 km^2 in area located within Stanford University's Jasper Ridge Biological Preserve, California, USA, which first filled in 1891 after the construction of Searsville Dam. In 2018, two sediment cores from Searsville Lake were collected from the deepest part of the reservoir, approximately 65 m south-southeast of Searsville Dam, using a vibracorer. The main reference core is JRBP2018-VC01B (37.406844°N, 122.237881°W) collected from a water depth of 2.68 m, near to the additional core VC01A. Both cores will be permanently reposited at the United States Geological Survey (USGS) Southwest Region cold storage facility at Moffett Field in Mountain View, California (USA), where they will be available to

future researchers with permission from the USGS. Details of the reference cores and of this site can be found in Stegner *et al*. (2023).

An annual and highly resolved chronology for JRBP2018-VC01B was constructed using a combination of seasonal-layer counting enabled by distinctive wet-season/dry-season couplets, distinctive sedimentary features, radiometric tie-points (^{137}Cs), and correlation of historic event and climate data to geochemical (Cu, Ca, Ti) and sedimentological signals (1906 and 1989 earthquakes) in the cores (Figure SV1). The core length of 944.5 cm spans from 1900–2018 CE. This very thick and continuous sequence means that the appearance and fluctuations in the markers of the Anthropocene can be mapped to particular years (and, in some cases, to season) with high confidence.

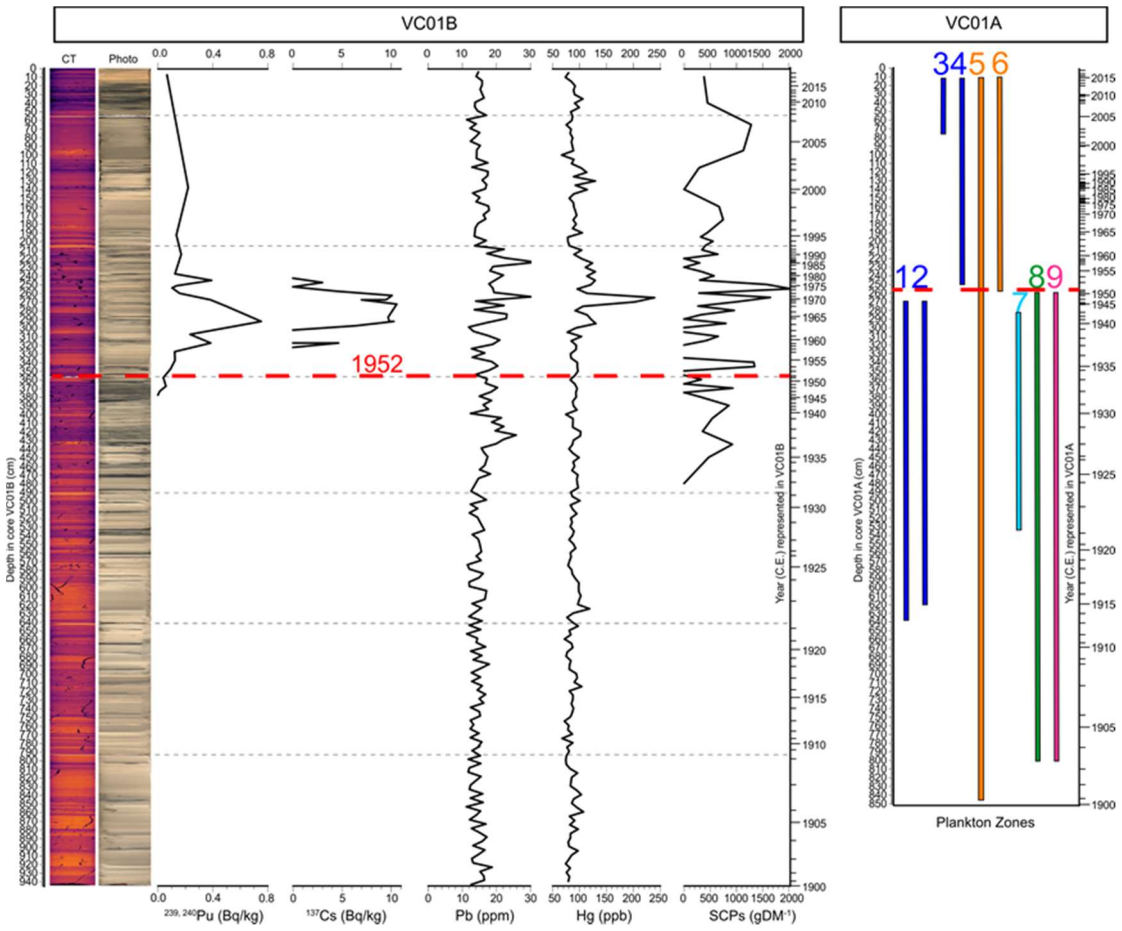

Figure SV1. Selected Searsville Lake global ($^{239+240}$Pu, ^{137}Cs), global/regional (Pb, Hg, SCPs), and local (microcrustacean and plankton zones) signals (latter from VC01A core). High abundance (>10%) zones for Candona *spp. (1), rotifers (7), algae (8), and protozoa (9); High abundance and persistence zones for* Physocypria globula *(4) and* Ceriodaphnia *(6); and occurrence zones for* Ilyocypris gibba *(2),* Cypria ophthalmica *(3), and* Daphnia *(5). From Stegner et al. (2023, fig. 13). Red dashed horizontal line at 1952 CE.*

Searsville Lake cores were analysed for biotic and geochemical markers of anthropogenic activities associated with the onset of the proposed Crawfordian stage. These reflect global processes ($^{239+240}$Pu, ^{137}Cs, δ^{15}N) as well as regional (SCPs) and

local influences (pollen, ostracods). Likely due to the presence of lignite (brown coal) in the watershed, ^{14}C from Searsville Lake sediments did not provide a coherent record. The $\delta^{13}C$ record from Searsville Lake is overprinted by a primarily local signal.

Key markers that allow correlation with the base of the Crawfordian stage GSSP

- In JRBP2018-VC01B, the lowest $^{239+240}Pu$ was detected at 372–374 cm, corresponding to late 1946 and early 1947 CE, with $^{239+240}Pu$ being found in all samples above this level (Figure SV1). Given that the earliest detonation was in 1945 CE, the onset is consistent with a 1- to 2-year lag-time between ejection of plutonium into the atmosphere from the tests and incorporation into geologic deposits. The core tracks the rise in atmospheric $^{239+240}Pu$ concentrations in the 1950s, with an early peak at 319.5–314 cm (1958 ± 0.5 to 1959 ± 0.5 CE), followed by a decline, matching the timing of the 1959 nuclear weapons testing moratorium. A temporary low point in $^{239+2409}Pu$ concentrations corresponds to 1961 CE, considered to represent the 1959–1960 moratorium in testing. A second $^{239+240}Pu$ peak is at 294.5–289 cm (1963 CE), following peak testing in 1962. Samples from 316.5–266.5 cm (1959 ± 0.5 to 1969 ± 1 CE) have $^{240}Pu/^{239}Pu$ ratios between 0.18 and 0.22, which confirms that the signal is from global nuclear fallout (Wu *et al*., 2011).
- The first detection of ^{137}Cs in JRBP2018-VC01B was at 319.5–314 cm (1958 ± 0.5 to 1959 ± 0.5 CE). ^{137}Cs increases up core to a peak at 294.5–289 cm, recognised as 1963 CE, and remains elevated until 259.5–246.5 cm (1971 ± 1 – 1976 ± 1 CE) before declining sharply (Figure SV1).
- The first SCPs were found at 449.5–449 cm (1934 ± 2 CE) (Figure SV1). Above this, SCP concentrations are variable and low overall, likely due to the high sedimentation rates in this reservoir. The SCP profile shows some similar features to other North American cores, with an increase in SCPs in sediments in the 1930s, peak SCPs in the 1970s and lower concentrations persisting through to today.
- Pb concentrations are low and fairly stable from the bottom of the core to ~540 cm (1928 ± 2 CE) (Figure SV1). From ~540 to ~415 cm (1928 ± 2 to 1938 ± 2 CE), Pb concentration increases significantly to a major peak at ~400–430 cm (1936 ± 2 to 1938 ± 1 CE). There are two additional peaks in Pb concentration at 263.5–264 cm (1970 ± 1 CE) and 223.5–224 cm (1985 ± 0.5 CE). Pb then declines from ~210 to ~120 cm (1991 ± 0.5 to 2001 ± 1 CE), returning to early 1900s values and remaining low to the top of the core. Thus, the Pb profile for Searsville Lake closely mirrors the increasing input of Pb into the atmosphere, especially from increasing use of leaded gasoline and other fossil fuels that began ~1930, the peak in Pb concentration in the 1970s, and the decline following environmental regulation and the introduction of unleaded gasoline.
- Average Hg concentration in JRBP2018-VC01B (91.7 ng/g) is roughly double the pre-industrial Hg concentration in cores from nearby Upper Lake Marsh (Redondo, 2022). The highest levels were seen in adjacent samples at 269.5 cm (1967 ± 2 CE) and 264.5 cm (1970 ± 1 CE) (Figure SV1). Elevated concentrations are also present below and above this major peak, from ~294 to ~224 cm (~1963 ± 0.5 to 1985 ± 0.5 CE). Above this, Hg concentration decreases toward the present, with one rebound at 129.5 cm (2000 ± 1 CE). Elevated Hg can therefore be used to identify sediments deposited during the post-industrial but pre-Crawfordian time, and peak Hg, corresponding to the

late 1960s and early 1970s, can identify deposits as securely in the Crawfordian/Anthropocene.

- PCBs were not detected in JRBP2018-VC01B samples below 461.5 cm (pre-1933 ± 2 CE). Above this depth, one congener was found in the sediment from 461.5 – 316.5 cm (1933 ± 2 –1959 ± 0.5 CE), seven congeners were found from 301.5 – 156.5 cm (1962 ± 0.5 –1998 ± 0.5 CE), and two congeners were found from 141.5 – 0.5 cm (1998 ± 1 – 2018 ± 0.25 CE). The pattern of PCB increases after 1950 CE, then decline matches global PCB production (see Part 1Section 3.2.6).

From neighbouring sediment core JRBP2018-VC01A subfossil paleobiological data include pollen, ostracods, and cladoceran ephippia can be used to establish local First and Last Appearance Data (FADs and LADs, respectively) and abundance zones (based on varying abundances of taxa), locally differentiating proposed Crawfordian/Anthropocene layers from underlying Holocene sediments.

- A useful local LAD is the loss of the ostracod *Ilyocypris* cf. *gibba,* which drops out of the record around 1948 CE, 14–16 cm below the proposed base of the Crawfordian stage (Figure SV1). Additionally, the ostracod *Cypria* cf. *ophthalmica* first appears near the top of the record core at 75–73 cm (2002–2003 CE). Local abundance zones also demarcate the transition. *Candona* spp. is the most abundant ostracod taxon in sediments deposited below 269 cm (1947 CE), while *Physocypria globula* is the most abundant ostracod species subsequently, first appearing at 248–250 cm (~1952 CE) and becoming abundant above ~154 cm (~1976 CE). Thus, the replacement of *Candona* spp. by *P. globula* marks the proposed Holocene–Anthropocene boundary in Searsville Lake. This boundary also clearly coincides with the locally rapid decline of rotifers, algae, and protozoa. Accordingly, a *P. globula* abundance zone is recognised from 248 cm (fall/winter 1952 ± 0.75 CE) to the top of the core (characterised by high *P. globula* abundance) as identifying Crawfordian/ Anthropocene sediments at Searsville Lake. A local rotifer-algae-protozoa abundance zone from the bottom of the core to 269 cm (summer of 1947 CE) identifies Holocene sediments, and pronounced decline or lack of those taxa above 264 cm (mid-1948 CE) helps to identify Anthropocene sediments. While the specific taxa involved in these zones may only apply locally at Searsville Lake, we expect that other deposits exhibit contemporaneous changes in microfossil assemblages as a result of intensifying anthropogenic activities in their watersheds. In addition, ongoing analyses of environmental DNA from the core are producing an extraordinarily detailed picture of biotic change associated with the Holocene-Anthropocene transition.

2.8 West Flower Garden Bank Reef, Gulf of Mexico, USA

Project Leader: Kristine DeLong; Summarised by Colin Waters

The 1.74 m-long reference core (05WFGB3) was retrieved in May 2005 from a *Siderastrea siderea* coral colony at West Flower Garden Bank Reef, located 180 km from the coast of Texas (27.8762°N, 93.8147°W) at a water depth of 21.3 m bsl. Details of the proposed reference core and site for the West Flower Garden Bank Reef are provided by DeLong *et al*. (2023).

The chronology ranging from 1755–2005 CE comes principally from annual growth layer counting, supported by seasonal variations in coral Sr/Ca and $\delta^{18}O$ and ^{230}Th dating (<± 1 year for corals <100 years old); ^{210}Pb activities are too low for a precise chronology and ^{137}Cs and ^{241}Am were not detected using gamma spectroscopy. The site was selected due to its distance from river runoff and coastal upwelling, with corals minimally affected by coral bleaching to date. The site is located in the Flower Garden Banks National Marine Sanctuary (FGBNMS), actively managed by the National Oceanic Atmospheric Administration, in which diver and fishing activity is restricted. The core 05WFGB3 is on loan from the FGBNMS and will ultimately be returned to them.

Key markers that allow correlation with the base of the Crawfordian stage

- The $^{239+240}Pu$ activities are not detectable in pre-1952 CE samples (below 31.38 cm), and show an initial peak in 1956 CE (29.03 cm depth), a dip in 1960 CE coinciding with the moratorium in testing (Figure WGF1d), and a second larger peak in 1964 CE (24.0 cm depth);
- The onset of the radiocarbon bomb-spike commences at 28.4–27.8 cm (1957 CE), with a prominent upturn in 1961 CE (Figure WGF1c) and peaks in 1970 CE (20.72 cm depth), later than Northern Hemisphere atmospheric changes probably due to a lag in transferring the $\Delta^{14}C$ signal to the surface ocean;
- Coral $\delta^{13}C$ is stable throughout the 1800s, with an average of −1.43‰ (Figure WGF2a). Coral $\delta^{13}C$ declined from about 1913 to 2005 CE by about 2.5‰ consistent with the Suess effect resulting from the increased burning of fossil fuels. The rate of decrease has accelerated especially after 1956 CE (Figure WGF1e);
- Coral skeleton $\delta^{15}N$ contains stable values from 1928 to 1962 CE with an average of 5.1‰ followed by an upturn to more positive values from 1963 CE (Figure WGF1g). This suggests increasing contribution of the Mississippi and Atchafalaya River system from the 1960s which shows a parallel increase in nitrogen load through increased fertiliser input;
- Monthly coral Sr/Ca has a significant linear decrease of 0.048 mmol/mol which suggests that sea-surface temperatures have risen by 1.1°C from 1932 to 2005 CE (Figure WGF1f). The interval from 1940 to 1970 CE has cooler SSTs with warmer SSTs after 1970 CE. The coldest interval is from 1810 to 1880 CE during the Little Ice Age (Figures WGF1f and WGF2b);
- Mercury concentrations are typically low, but with lowest values in 1945 CE and 1980 CE (Figure WGF1h), followed by consistently very low values except the topmost sample which has elevated Hg concentrations as residues from the coral tissue layer, which concentrates Hg compared to the coral skeleton;
- Monthly coral Ba/Ca records increases from 1965–1983 CE, with a peak in 1983 CE (Figure WGF1i), which coincides with the height of Gulf of Mexico oil drilling, which uses barite ($BaSO_4$) as a drilling mud that is discarded on the seafloor, thus increasing concentrations of barium in the seawater (Weerabaddana *et al*., 2021).

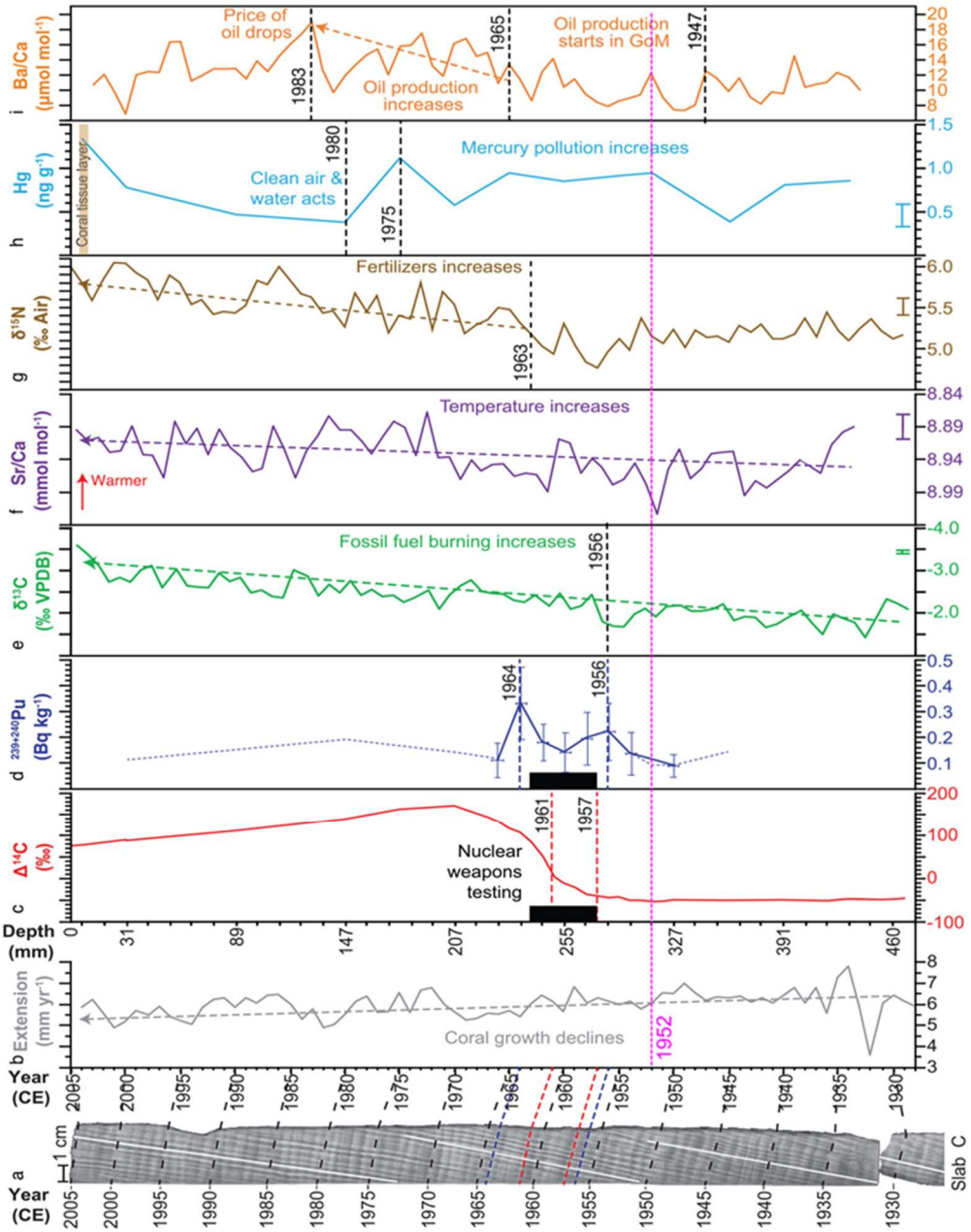

Figure WFG1. Composite of annually-resolved proxies from core 05WFGB3 focusing on the interval 1928–2005 CE: (a) X-radiograph of slab C with examples of counting path (white lines) and every 5 years noted (labels on ~January) connected to (b) years in the coral annual extension (black dashed lines). Years for the $\Delta^{14}C$ markers are noted as red dashed lines in (a and c) and $^{239+240}Pu$ marker with blue dashed lines in (a and d) with blue dotted line as limit of detection values (sample activity is less than this value) rather than actual measured activity. (b) Annual extension was determined from coral growth direction noted as white lines in (a). Depth from core top for (c–i) is aligned with extension (b) and years (a) with depth noted for January of each year or the base of the annual sample for the annually-sampled proxies (c, d, g, and h) and the annual average from monthly samples (e, f, and i). Black boxes span 1957–1963 CE, the period of extensive atmospheric thermonuclear weapons testing (c and d). Linear trends (dashed lines with arrowheads) are significant (1%). Error bars represent analytical precision (1σ) and if not plotted analytical precision is smaller than the line weight. From DeLong et al. (2023, fig. 2).

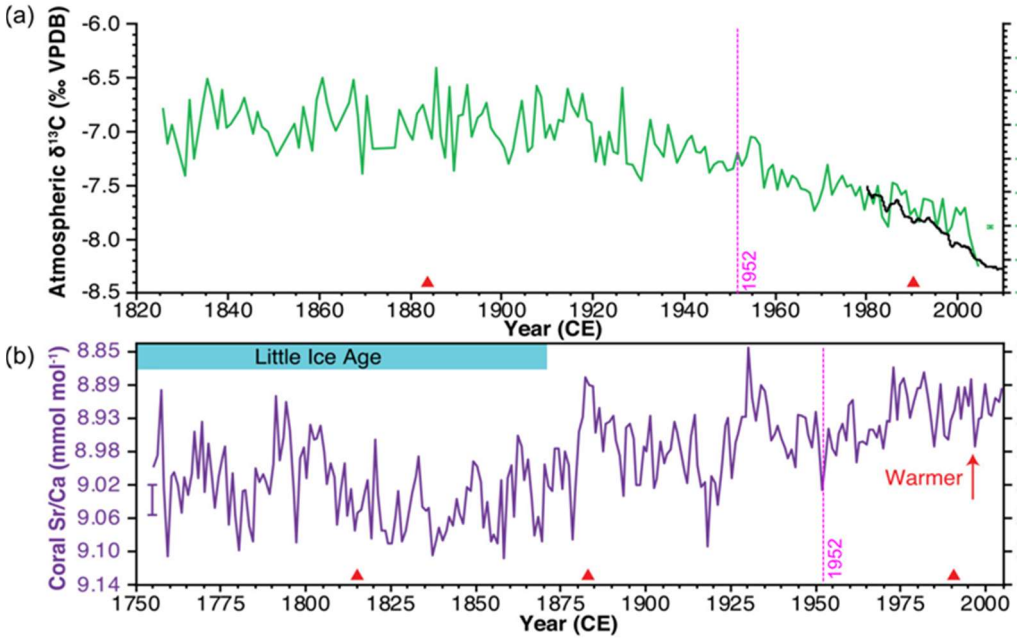

Figure WFG2. Annual average coral environmental markers from entire core 05WFGB3 (a) Monthly coral $\delta^{13}C$ values averaged in the interval from 1932–2005 CE and annual maximum and minimum $\delta^{13}C$ values were averaged in the interval from 1826–1932 CE. Atmospheric $\delta^{13}C$ is from Mauna Loa, Hawaii is shown with the quasi-regular seasonal cycle removed (Keeling et al., 2001). (b) Monthly coral Sr/Ca variations annually-averaged in the interval from 1755–2005 CE, converted to SST using the coral Sr/Ca-SST equation for this coral (Weerabaddana et al., 2021) and are scaled to the same temperature range and plotted so that warmer values are up. Error bars (1σ) are analytical precision determined for monthly samples. From DeLong et al. (2023, fig. 5).

REFERENCES USED IN THE APPENDICES (* key references)

*Borsato, A., Fairchild, I.J., Frisia, S., Wynn, P.M., Fohlmeister, J., 2023. The Ernesto Cave, northern Italy, as a candidate auxiliary reference section for the definition of the Anthropocene series. *The Anthropocene Review* **10**(1): 269–287. https://doi.org/10.1177/20530196221144094

Bouchet, V.M.P., Pavard, J.-C., Holzmann, M. *et al*., 2023. The invasive Asian benthic foraminifera *Trochammina hadai* Uchio, 1962: identification of a new local in Normandy (France) and a discussion on its putative introduction pathways. *Aquatic Invasions* **18**(1): 23-38. https://doi.org/10.3391/ai.2023.18.1.103512

Calvo, E., Marshall, J.F., Pelejero, C. *et al*., 2007. Interdecadal climate variability in the Coral Sea since 1708 A.D. *Palaeogeography Palaeoclimatology Palaeoecology* **248:** 190–201. https://doi.org/10.1016/j.palaeo.2006.12.003

Dalmeri, G., 1985. La Grotta d'Ernesto: un insediamento preistorico di grande interesse per la conoscenza del Paleolitico finale nell'area trentino-veneta (Colle dei Meneghini-Val d'Antenne, Trentino sud-orientale). *Natura Alpina, Museo Tridentino di Scienze Naturali* **36**(2–3): 31–40.

*DeLong, K.L., Palmer, K., Wagner, A.J., Weerabaddana, M.M., Slowey, N., Herrmann, A.D., Duprey, N., Martínez-García, A., Jung, J., Hajdas, I., Rose, N.L., Roberts, S.L., Roberts, L.R., Cundy, A.B., Gaca, P., Milton, J.A., Yang, H., Turner, S.D., Huang, C.-Y., Shen, C.-C., Zinke, J., 2023. The Flower Garden Banks *Siderastrea siderea* coral as a candidate Global boundary Stratotype Section and Point for the Anthropocene series. *The Anthropocene Review* **10**(1): 225–250. https://doi.org/10.1177/20530196221147616

Eichler, P.B. McGann, M., Rodrigues, A.R. *et al*., 2016. The occurrence of the invasive foraminifera *Trochammina hadai* Uchio in Flamengo Inlet, Ubatuba, São Paulo State, Brazil. *Micropaleontology* **64**(5/6): 391-402. https://www.jstor.org/stable/26759098

Emanuelsson, B.D., Thomas, E.R., Tetzner, D.R. *et al*., 2022. Ice core chronologies from the Antarctic Peninsula: The Palmer, Jurassic, and Rendezvous age-scales. *Geosciences* **12**(2): 87.

Fohlmeister, J., Kromer, B., Mangini, A., 2011. The influence of soil organic matter age spectrum on the reconstruction of atmospheric ^{14}C levels via stalagmites. *Radiocarbon* **53**(1): 99–115. https://doi.org/10.1017/S003382220003438X

Foxgrover, A.C., Higgins, S.A., Ingraca, M.K. *et al.,* 2004. Deposition, erosion and bathymetric change in South San Francisco Bay: 1858‑1983. *Open-File Report 2004-1192*. Available at: https://pubs.usgs.gov/of/2004/1192/of2004-1192.pdf (accessed 15 September 2021).

Frisia, S., Borsato, A., Preto, N. *et al*., 2003. Late Holocene annual growth in three alpine stalagmites records the influence of solar activity and the North Atlantic Oscillation on winter climate. *Earth and Planetary Science Letters* **216**(3): 411–424. https://doi.org/10.1016/S0012-821X(03)00515-6

Frisia, S., Borsato, A., Fairchild, I.J., Susini, J., 2005. Variations in atmospheric sulphate recorded in stalagmites by synchrotron micro-XRF and XANES analyses. *Earth and Planetary Science Letters* **235**: 729–740. https://doi.org/10.1016/j.epsl.2005.03.026

Fuller, C.C., van Geen, A., Baskaran, M., Anima, R., 1999. Sediment chronology in San Francisco Bay, California, defined by ^{210}Pb, ^{234}Th, ^{137}Cs and $^{239,240}Pu$. *Marine Chemistry* **64**(1–2): 7–27. https://doi.org/10.1016/S0304-4203(98)00081-4

Head, M.J., Gibbard, P.L., 2015. Formal subdivision of the Quaternary System/Period: Past, present, and future. *Quaternary International* **383**: 4–35. https://doi.org/10.1016/j.quaint.2015.06.039

*Himson, S., Williams, M., Zalasiewicz, J., Waters, C., McGann, M., England, R., Boom, A., Holmes, R., Sampson, S., Pye, C., Berrio, J.C., Tyrrell, G., Wilkinson, I.P., Rose, N., Cundy, A., 2023. The San Francisco Estuary, USA as a reference section for the Anthropocene series. *The Anthropocene Review* **10**(1): 87–115. https://doi.org/10.1177/20530196221147607

Hua, Q., Turnbull, J.C., Santos, G.M. *et al*., 2021. Atmospheric Radiocarbon for the Period 1950–2019. *Radiocarbon* **64**: 723-745. https://doi.org/10.1017/rdc.2021.95

*Kaiser, J., Abel, S., Arz, H.W. Cundy, A.B., Dellwig, O., Gaca, P., Gerdts, G., Hajdas, I., Labrenz, M., Milton, J.A., Moros, M., Primpke, S., Roberts, S.L., Rose, N.L., Turner, S.D., Voss, M., Ivar do Sul., J.A., 2023. The East Gotland Basin (Baltic

Sea) as a candidate Global boundary Stratotype Section and Point for the Anthropocene series. *The Anthropocene Review* **10**(1): 25–48. https://doi.org/10.1177/20530196221132709

Keeling, C.D., Piper, S.C., Bacastow, R.B. *et al*., 2001. Exchanges of atmospheric CO_2 and $^{13}CO_2$ with the terrestrial biosphere and oceans from 1978 to 2000. I. Global aspects, SIO Reference Series, No. 01-06, Scripps Institution of Oceanography, San Diego.

Mosser, M., 2019. KG Wieden, 4. Bezirk. *Fundberichte aus Österreich* **58**: 454–455.

Mosser, M., Litschauer, C., 2021. Bericht über die archäologische Grabung Wien 4, Karlsplatz vor Nr. 8 (Wien Museum neu 2019–2021). *Unpublished report of the Museen der Stadt Wien - Stadtarchäologie*.

Pelejero, C., Calvo, E., McCulloch, M.T. *et al*., 2005. Preindustrial to modern interdecadal variability in coral reef pH. *Science* **309**: 2204–2207. https://doi.org/10.1126/science.1113692

Peterson, L.C., Haug, G.H., 2006. Variability in the mean latitude of the Atlantic Intertropical Convergence Zone as recorded by riverine input of sediments to the Cariaco Basin (Venezuela). *Palaeogeography, Palaeoclimatology, Palaeoecology* **234**(1): 97–113. https://doi.org/10.1016/j.palaeo.2005.10.021

Redondo, S. 2022. *Signals of an Insidious Pollutant: Temporal, Spatial, and Biotic Interplay of Anthropogenic Mercury in a Terrestrial Ecosystem.* PhD thesis, Stanford University.

Remane, J., Bassett, M.G., Cowie, J.W. *et al*., 1996. Revised guidelines for the establishment of global chronostratigraphic standards by the International Commission on Stratigraphy (ICS). *Episodes* **19**: 77–81.

Scholz, D., Frisia, S., Borsato, A. *et al*., 2012. Holocene climate variability in north-eastern Italy: potential influence of the NAO and solar activity recorded by speleothem data. *Climate of the Past* **8**: 1367–1383. https://doi.org/10.5194/cp-8-1367-2012

Sobik, M., Błaś, M., Migała, M. *et al*., 2014. Klimat. In: Knapik R and Raj A (eds) *Przyroda Karkonoskiego Parku Narodowego* [Karkonoski Park Narodowy]. Jelenia Gora, Bielsko-Biała: DIMOGRAF, pp.147‑186.

*Stegner, M.A., Hadly, E.A., Barnosky, A.D., La Selle, S., Sherrod, B., Anderson, R.S., Redondo, S.A., Viteri, M.C., Weaver, K.L., Cundy, A.B., Gaca, P., Rose, N.L., Yang, H., Roberts, S.L., Hajdas, I., Black, B.A., Spanbauer, T.L., 2023. The Searsville Lake Site (California, USA) as a candidate Global boundary Stratotype Section and Point for the Anthropocene series. *The Anthropocene Review* **10**(1): 116–145. https://doi.org/10.1177/20530196221144098

Thomas, E.R., Vladimirova, D.O., Tetzner, D.R. *et al*., 2023a. The Palmer ice core as a candidate Global boundary Stratotype Section and Point for the Anthropocene series. *The Anthropocene Review* **10**(1): 251–268. https://doi.org/10.1177/20530196231155191

*Thomas, E.R., Vladimirova, D.O., Tetzner, D.R., Emanuelsson, D.B., Humby, J., Turner, S.D., Rose, N.L., Roberts, S.L., Gaca, P., Cundy, A.B., 2023a. The Palmer ice core as a candidate Global boundary Stratotype Section and Point for the

Anthropocene series. *The Anthropocene Review* **10**(1): 251–268. https://doi.org/10.1177/20530196231155191

Tremblin, C.M., Holzmann, M., Parker, J.H. *et al*., 2022. Invasive Japanese foraminifera in a south-west Australian estuary. *Marine and Freshwater Research* **73**: 328–342. https://doi.org/10.1071/MF21254

UNSCEAR (United Nations Scientific Committee on the Effects of Atomic Radiation) 2000. *Sources and Effects of Ionizing Radiation*, 2000 Report, Volume 1. New York: United Nations. https://www.unscear.org/unscear/en/publications/2000_1.html

*Wagreich, M., Meszar, M., Lappé, K., Wolf, J., Mosser, M., Hornek, K., Koukal, V., Litschauer, C., Piperakis, N., Hain, K., 2023. The urban sediments of Karlsplatz, Vienna (Austria) as a reference section for the Anthropocene series. *The Anthropocene Review* **10**(1): 316–329. https://doi.org/10.1177/20530196221136427

*Waters, C.N., Turner, S.D., Zalasiewicz, J., Head, M.J. (Eds.), 2023. Candidate sites and other reference sections for the Global boundary Stratotype Section and Point of the Anthropocene series. *The Anthropocene Review* **10**(1): 3–24. https://doi.org/10.1177/20530196221136422

Weerabaddana, M.M., DeLong, K.L., Wagner, A.J. *et al*., 2021. Insights from barium variability in a *Siderastrea siderea* coral in the northwestern Gulf of Mexico. *Marine Pollution Bulletin* **173**: 112930. https://doi.org/10.1016/j.marpolbul.2021.112930

Wu, F., Zheng, J., Liao, H. *et al*., 2011. Anomalous plutonium isotopic ratios in sediments of Lake Qinghai from the Qinghai-Tibetan Plateau, China. *Environmental Science and Technology* **45**: 9188–9194. https://doi.org/10.1021/es202315c

Wynn, P.M., Fairchild, I.J., Frisia, C. *et al*., 2010. High-resolution sulphur isotope analysis of speleothem carbonate by secondary ionization mass spectrometry. *Chemical Geology* **271**(3–4): 101–107. https://doi.org/10.1016/j.chemgeo.2010.01.001

Zalasiewicz, J., Waters, C.N., Summerhayes, C.P. *et al*. 2017a. The Working Group on the Anthropocene: Summary of evidence and interim recommendations. *Anthropocene* **19**: 55–60. https://doi.org/10.1016/j.ancene.2017.09.001

*Zinke, J., Cantin, N.E., DeLong, K.L., Palmer, K., Boom, A., Hajdas, I., Duprey, N., Martínez-García, A., Rose, N.L., Roberts, S.L., Yang, H., Roberts, L.R., Cundy, A.B., Gaca, P., Milton, J.A., Frank, G., Cox, A., Sampson, S., Tyrrell, G., Agg, M., Turner, S.D., 2023. North Flinders Reef (Coral Sea, Australia) *Porites* sp. corals as a candidate Global boundary Stratotype Section and Point for the Anthropocene series. *The Anthropocene Review* **10**(1): 201–224. https://doi.org/10.1177/20530196221142963